SPECTRAL DISTORTIONS & ENHANCEMENTS IN COHERENT ANTI-STOKES RAMAN SCATTERING HYPERSPECTROSCOPY

Aaron M. Barlow

A thesis submitted to the
Faculty of Graduate and Postdoctoral Studies
in partial fulfillment of the requirements for a
Doctor of Philosophy in Physics

Department of Physics
Faculty of Science
University of Ottawa

Abstract

Coherent anti-Stokes Raman scattering microscopy is a versatile technique for label-free imaging and spectroscopy of systems of biophysical interest. Due to the coherent nature of the generated signals, CARS images and spectra can often be difficult to interpret. In this thesis, we document how distortions and enhancements can be produced in CARS hyperspectroscopy as a result of the instrument, geometrical optical effects, or unique molecular states, and discuss how these effects may be suppressed or exploited in various CARS applications.

Microscopie "coherent anti-Stokes Raman scattering" est une technique polyvalent pour l'imagerie et la spectroscopie des systèmes d'intérêt biophysique. En raison de la nature cohérente des signaux générés, les images et les spectre de CARS peuvent souvent être difficiles à l'interpréter. Dans cette thèse, nous montrons comment les distorsions et les améliorations peuvent être produites dans CARS hyper-spectroscopie comme un résultat de l'instrument, des effets d'optique géométrique, ou états moléculaires uniques, et nous discutons comment ces effets peuvent être supprimés ou exploités dans diverses applications de CARS.

Contents

Acknowledgements **vii**

List of Acronyms **ix**

1 Introduction **1**

2 Background **7**
2.1 CARS Theory 7
2.2 Raman Retrieval 13

3 CARS Microscope Implementation **18**
3.1 Overview of CARS Microscopy Implementations 18
3.2 Chirp-Matched CARS Microscope Design 21
3.3 Translation Stage Calibration 24
Direct Peak Interpolation 24
Calibration by Sum-Frequency Generation 25
Calibration by Four-Wave Mixing 27
3.4 Stokes Generation 27
3.5 Chirp Matching 30

4 Spatial-Spectral Coupling in CARS Microscopy **34**
4.1 Introduction 34
4.2 Theory 35
4.3 Method and Materials 37
Experimental Design 37
Numerical Simulations 40
4.4 Results 41
4.5 Discussion 44
4.6 Conclusions 47

5 The Remarkable Algae *Haematococcus Pluvialis* **50**
5.1 Introduction 50
5.2 Method and Materials 54
Introduction 54
Preparation of the Algae 54
Preparation of AstaREAL 55
Collection of Spontaneous Raman 58
Preparation of Astaxanthin Radicals 59
5.3 CARS Microscopy of *Haematococcus pluvialis* 59
5.4 Discussion 64

6 Four-Wave Mixing Microscopy of *Haematococcus Pluvialis* 78
6.1 Introduction of Four-Wave Mixing Microscopy 78
6.2 Theory of Four-Wave Mixing 79
6.3 Method and Materials 82
Introduction 82
Video Collection 83
Wavelength Dependence 84
6.4 FWM Microscopy of *Haematococcus pluvialis* 84
6.5 Discussion 89

7 The Effective Conjugation Coordinate Model in CARS Microscopy 96
7.1 Introduction 96
7.2 Calculating Raman Spectra from the ECCM 99
7.3 Calculating γ from the ECCM 102
7.4 Discussion 105
7.5 Conclusion 110

8 Time-Correlated Single Photon Counting CARS Microscopy 111
8.1 Introduction 111
8.2 Theory of TCSPC 115
Fluorescence Lifetime 115
Forster Resonance Energy Transfer 117
8.3 Method and Materials 119
Multi-modal TCSPC Setup 119
Detector Control 121
Calibration of the PML-16-C 122
Measuring the Instrument Response Function 123
Sample Preparation 124
8.4 Applications of TCSPC 125
Fluorescence Lifetime Imaging 125
Time-Gated FWM with TCSPC 126
8.5 Discussion 128

9 Conclusion 139

Appendices 145

A Microscope Alignment 145

B Configuring the TCSPC Module 149

List of Publications 152

List of Figures

2.1 The energy level diagram of CARS 9
2.2 Nitrobenzene: CARS, Raman, Retrieved 17
3.1 Frequency-Time Graph of Chirp-Matched CARS 19
3.2 Chirp-Matched CARS Microscope Design 22
3.3 Calibration of the Delay Stage Using SFG from KDP 26
3.4 Calibration of the Delay Stage Using FWM from Astaxanthin . . 28
3.5 Variations in Stokes Power with Time 29
3.6 Effects of Chirp on Spectral Resolution 33
4.1 Spontaneous Raman spectrum of nitrobenzene 38
4.2 CARS image of nitrobenzene droplets in gel 39
4.3 Experimentally measured CARS spectra of nitrobenzene droplets at three focal positions 42
4.4 Numerically generated CARS spectra of nitrobenzene droplets at three focal positions 43
4.5 Induced phase shifts in CARS signal resulting from linear index mismatch and Gouy phase 45
4.6 Generated CARS and retrieved Raman spectra including the effects of Gouy phase and linear index mismatch 47
4.7 Positions of the shifted Raman peaks at various spectral linewidths 48
5.1 Life Cycle of *Haematococcus pluvialis* 51
5.2 Absorption Spectrum of *Haematococcus pluvialis* 56
5.3 High-power CARS Images of *Haematococcus pluvialis* 70
5.4 CARS Images of Algal Cysts 71
5.5 3-Dimensional CARS + TPEF Reconstruction of Algal Cyst . . 72
5.6 CARS Spectrum of *Haematococcus pluvialis* 73
5.7 Concentration Plot for AstaREAL 73
5.8 Quantitative Concentration Map of *Haematococcus pluvialis* . . . 74
5.9 CARS Spectrum of AstaReal Dilutions Compared to Diamond . 74
5.10 Energy level diagram of astaxanthin 75
5.11 Pump wavelength dependence of astaxanthin compared to diamond 76
5.12 Spectroscopy of AstaReal and its radical 77
6.1 Motion of a spinning algae monitored by FWM microscopy in a 256x256 field 86
6.2 Motion of a travelling algae monitored by FWM microscopy . . . 87
6.3 FWM Microscopy of a single algal cyst 92
6.4 Life cycle of *haematococcus pluvialis* by FWM and TPEF 93
6.5 FWM intensity dependence on pump wavelength 94
6.6 FWM and CARS intensity in the fingerprint 95
7.1 The spontaneous Raman spectrum of Astaxanthin 101
7.2 Chain length dependencies of linear polyenes 109
8.1 Example of Fluorescence Lifetime Histograms 116
8.2 Schematic of the FRET Process 118
8.3 Block Diagram of TCSPC 120

8.4 Instrument response functions of the R3809-U50 and PML-16-C detectors. 132
8.5 FLIM of fluorescein and Nile red 133
8.6 Fluorescent spectrum of fluorescein with lifetime 133
8.7 16-channel wavelength imaging of FCN and NLR interface 134
8.8 16-channel FLIM of fluorescein and Nile red 135
8.9 Simultaneous FWM and FLIM measurement with the PML-16-C detector 136
8.10 Simultaneous FWM and FLIM measurement with the R3809-U50 detector 137
8.11 Background rejection of the detectors 138
A.1 Alignment of the Laser System 146
A.2 Alignment of the Microscope Condensor 147
B.1 Example of SPCM Interface 150

List of Tables

8.1 Calibration of PML-16-C 16 Channel Detector 123
A1 System parameters for C-H and fingerprint CARS implementations. 149

Acknowledgements

I would first like to thank my beloved wife Kate, for her endless love, support, and patience throughout this entire process. I would also like to thank my parents, Jim and Lorraine, and my brother Jim, for their faith and support of me. Thanks to my supervisor, Dr. Albert Stolow, for providing me with the opportunity to do research in a world-class facility and with a fantastic research group. I also thank the members of the CARS group, Marco Andreana, Andrew Ridsdale, Rune Lausten, and Doug Moffatt, for their invaluable assistance and advice. I would like to thank Dr. Aaron Slepkov from Trent University for his mentorship and extensive collaboration. I thank my co-supervisor, Jim Harden. I would also like to acknowledge funding provided by the NSERC CREATE Program in Quantitative Biomedicine.

This thesis is based, in part, on the following four papers:

- A. M. Barlow, A. D. Slepkov, A. Ridsdale, P. J. McGinn, and A. Stolow, "Label-free hyperspectral nonlinear optical microscopy of the biofuel microalgae Haematococcus Pluvialis," *Biomedical Optics Express,* vol 5., pp 3391-3402, Sept. 2014

- A. D. Slepkov, A. M. Barlow, A. Ridsdale, P. J. McGinn, and A. Stolow, "In vivo hyperspectral CARS and FWM microscopy of carotenoid accumulation in H. Pluvialis," *Proc. SPIE 8937, Multimodal Biomedical Imaging IX,* 893707, Feb. 2014

- A. M. Barlow, K. Popov, M. Andreana, D. J. Moffatt, A. Ridsdale, A. D. Slepkov, J. L. Harden, L. Ramunno, and A. Stolow, "Spatial-spectral coupling in coherent anti-Stokes Raman scattering microscopy," *Optics Express,* vol. 21, pp 15298-15307, Jun. 2013

- A. M. Barlow, K. Popov, M. Andreana, D. J. Moffatt, A. Ridsdale, A.

D. Slepkov, L. Ramunno, and A. Stolow, "Spatial-spectral coupling in hyperspectral CARS microscopy image formation," *Proc. SPIE 8589, Three-Dimensional and Multidimensional Microscopy: Image Acquisition and Processing XX,* 85890T, Feb. 2013

The last two papers cover the topic of spatial spectral coupling, which is covered in Chapter 4 in this thesis. In this work, I was responsible for performing the CARS measurements (Chapter 4.3) that were designed in collaboration among myself, Marco Andreana, Andrew Ridsdale, Aaron Slepkov, Jim Harden and Albert Stolow. The FDTD calculations were performed by Konstantin Popov and Lora Ramunno (Chapter 4.3), whereas I performed the 1D models in Chapter 4.5. Doug Moffatt provided the code for Raman retrieval.

The remaining papers cover the topic of the microalgae *haematococcus pluvialis* described in Chapters 5 and 6. The topic of the enhancement in Chapter 7 is introduced briefly in these papers, but was not resolved at the time of publication. These papers represent an extensive collaboration primarily between myself and Aaron Slepkov, and the majority of the experiments and subsequent analysis we undertook jointly. The photobleaching experiments (eg. Figure 5.3) were performed by Andrew Ridsdale. The algae were cultivated by Patrick McGinn. Andrew Ridsdale and Albert Stolow also contributed to the interpretation of the data.

List of Acronyms

ADC Analog-to-digital converter

AXN* The radical of astaxanthin

CARS Coherent anti-Stokes Raman scattering

CFD Constant fraction discriminator

ECCM Effective Conjugation Coordinate Model

FCN Fluorescein

FLIM Fluorescence lifetime imaging

FRET Förster resonance energy transfer

FWM Four-wave mixing

IRF Instrument response function

KDP Potassium dihydrogen phosphate

NA Numerical aperture

NBZ Nitrobenzene

NIR Near-infrared

NLO Nonlinear optics

NLR Nile Red

NRB Nonresonant background

OPO Optical parametric oscillator

OSA Optical spectrum analyzer

PCF Photonic crystal fibre

PMT Photomultiplier tube

PSD Power-spectral density

SFG Sum-frequency generation

SHG Second harmonic generation

SPCM Single-Photon Counting Module (software)

SRS Stimulated Raman scattering

TAC Time-to-amplitude converter

TCSPC Time-correlated single photon counting

TPEF Two-photon excited fluorescence

ZDW Zero-dispersion wavelength

1 Introduction

The optical microscope is perhaps the most powerful tool in the biologist's toolkit. Since 17th century pioneer Antonie van Leeuwenhoek first observed micro-organisms in his home-built optical microscopes, researchers have been intensely interested in the microscopic origins of disease, in cellular structure and function, and in plant and animal physiology. Light microscopes are an ubiquitous part of any biology lab, and the backbone of innumerable studies and discoveries in the field. While more sophisticated methods such as transmission electron microscopy, scanning-tunneling microscopy, and atomic force microscopy have improved the resolution of microscopes to well below the diffraction limit, these methods are often unsuitable for the study of living systems due to such things as difficult sample preparation requirements, the need for vacuum chambers, or the necessity for interferometric stability [1, 2, 3]. Consequently, optical microscopy remains the dominant tool of biological research. Unfortunately, nature is not colour-coded for our convenience; standard optical microscopes may not provide the necessary contrast to be able to identify particular features of interest within a biological specimen. To circumvent this problem, researchers have developed a number of ingenious microscopy techniques in order to meet their needs. One approach taken by microscopists has been to develop microscopy techniques based on nonlinear optics (NLO). NLO exploits the intense, collimated, and coherent nature of lasers in order to access a regime of higher-order effects that are otherwise so weak that they are impossible to observe using everyday light. Nonlinear optical microscopy offers a unique synthesis of novel physics spanning the classical and quantum regimes, applied to challenging problems of biophysical interest.

The genesis of NLO came shortly after the invention of the laser in 1960, when Franken et al.[4] discovered that 694 nm light focused through a quartz

crystal generated coherent light at 347 nm propagating in the direction of the laser, the strength of which depended on the intensity of the focused laser light. This process was called second harmonic generation (SHG) because the new radiation was engendered at twice the frequency (or half the wavelength) of the driving field. A flurry of new nonlinear effects were quickly discovered: third harmonic generation (1962) [5], sum frequency generation (SFG) (1962) [6], difference frequency generation (1965) [7], degenerate four-wave mixing (1966)[8], and coherent anti-Stokes Raman scattering (CARS) (1965)[9]. The common theme of these various effects is a higher-order dependence of the induced polarization $\vec{P}$ on the driving electric field(s) $\vec{E}$, mediated by the nonlinear polarizability tensors $\chi^{(2)}$, $\chi^{(3)}$, etc. Hence these phenomena may be described by a perturbation series expansion in χ as shown in Equation 1.1.

$$\vec{P} = \epsilon_0(\chi^{(1)}\vec{E} + \chi^{(2)}\vec{E}\cdot\vec{E} + \chi^{(3)}\vec{E}\cdot\vec{E}\cdot\vec{E} + \ldots) \tag{1.1}$$

The terms in $\chi^{(2)}$ are second-order effects, depending on the intensity ($|\vec{E}|^2$) of the electric field E ; the terms in $\chi^{(3)}$ are third-order effects, depending on the intensity to the three-halves, and so on. Note that many nonlinear optical effects such as sum-frequency generation and CARS involve the interactions of multiple fields at different frequencies. The magnitudes of the polarizabilities are very small ($\chi^{(2)}$ $\sim 10^{-12}$ m/V; $\chi^{(3)}$ $\sim 10^{-24}$ m^2/V^2)[10], so these terms only contribute appreciably at high intensities. Modern laser systems use ultra short ($\sim$100 fs), intense ($>10^7$ W/cm^2) laser pulses to generate these effects.

CARS is a four-wave mixing (FWM) process that involves the interaction of four photons mediated through a Raman resonance. It can thus be considered to be a nonlinear analogue to spontaneous Raman scattering. The Raman effect, first observed in 1928 [11], is a scattering process that allows small quanta of energy to be exchanged between a photon and an atom or molecule during a

scattering event that is coupled to a molecular vibration. The energy transferred is given by $\hbar\Omega$, where Ω is the frequency of the vibrational energy level that the photon is coupled to. When spontaneous Raman scattering from the ground state occurs, it is red-shifted (Stokes shifted) relative to the incident field. In CARS, the vibrational energy level is excited by two lasers whose difference frequency is equal to Ω. A further excitation by the higher frequency laser results in a blue-shifted (anti-Stokes) response. Because CARS is based on stimulated emission rather than spontaneous emission, its signal intensities in the forward direction are many orders of magnitude greater than Raman, and thus more efficient generation of images or spectra [12].

CARS has been used extensively for gas-phase spectroscopy [13, 14, 15, 16, 17], and, more recently, has become a subject of interest for microscopy applications. CARS was first successfully applied to microscopy in 1982 [18], but the technical challenges of using noisy, visible light lasers available at the time rendered this more a novelty than a subject of intensive research. It was not until 1999, when Zumbusch et al. [19] used a novel confocal microscope design with synchronized, short-pulse infrared lasers to generate CARS, that the field of CARS microscopy became an area of active research. CARS provides several key advantages that make it ideally suited for the study of biological systems. First, CARS is a parametric process; no energy is deposited into the system as a result of the CARS interaction, and therefore, the CARS process itself will not produce excess heat or photodamage to sensitive systems. Second, because the CARS process depends on a resonant interaction with a vibrational energy level, it can provide chemical specificity via the generated spectrum without the need for fluorescent dyes or stains–label-free imaging. Finally, since CARS is a third-order optical process, its intensity will scale with the product of the intensities of the three interacting laser fields. As a result of this cubic dependence

on intensity, in a confocal microscope design, CARS will only be appreciably generated at the microscope focus, allowing for three-dimensional sectioning of samples, with high penetration depth due to the use of near-infrared lasers. Theoretical treatments of CARS microscopy under tightly focused conditions has been an important aspect of understanding CARS images and were developed concurrently to early microscope designs [20, 21]. The original Zumbusch design of the CARS microscope was restricted by the laser bandwidths to a frequency range near 2850 cm^{-1}, corresponding to the dominant Raman resonance of condensed lipids[1]. Due to the significant strength the lipid resonance and the relative ease of developing a system capable of studying this region, the bulk of CARS applications are dedicated to the study of lipids [22, 23, 24]. While representing a minority in the literature at this time, CARS systems with larger tuning ranges were able to access other Raman-active regions of the vibrational spectrum. These include water [25], as well as the fingerprint region [26, 27]. The fingerprint region, the spectral region extending from 800 cm^{-1} to 1800 cm^{-1}, contains vibrational resonances for many molecular vibrations N-H, O-H, C-H, C-H_2, and CH_3, which are present in innumerable molecules of biological significance including proteins, amino acids, carotenoids cellulose, and carbonate.

A significant downside to CARS microscopy is the presence of an ubiquitious nonresonant background (NRB) that is generated concurrently and coherently to CARS by non-vibrationally resonant four-wave mixing from the solvent. Because the NRB field is of the same frequency and coherent to the resonant CARS process, it interferes, producing both distortions in the spectrum [12], as well as imaging artefacts [28]. This interference from the NRB can significantly compli-

[1]Following spectroscopic convention, frequencies in this thesis will be quoted in wavenumbers with units of cm^{-1}, rather than in Hz. Wavenumber can be converted to frequency by $\omega = ck$ where k is the wavenumber, ω is the frequency, and c is the speed of light. For similar reasons, intensities will be quoted in W/cm^2

cate quantitative applications of CARS. The interference between the NRB and the CARS response results in a shift in the position of a spectral peak, as well as a change in its intensity; in spectrally congested regions, such as the fingerprint, there is a considerable risk of misidentifying a spectral feature. The intensity changes manifest as an unusual dependence on the concentration of resonant oscillators. If the CARS response is large, then there is a quadratic dependence on the number of resonators; however, if the NRB is large, then there is only a linear dependence on the number of oscillators [12]. As a result, measuring the concentration of sample using CARS is a non-trivial endeavour. NRB suppression can be achieved through a variety of methods, including interferometric CARS [29], polarization CARS [30], and frequency-modulation CARS [31]. However, these methods tend to suffer other drawbacks such as low signals or difficult implementations. As an alternative, some groups have attempted to separate the resonant CARS spectrum from the NRB using post-processing retrieval algorithms [32, 33].

The major theme of this thesis is how the interplay between the sample, the instruments, and the coherently generated CARS and NRB signals affect our visualization and interpretation of CARS images and spectra. This interplay manifests itself primarily through distortions in the CARS spectrum. These distortions may take the form of a very desirable enhancement, which can boost the signal intensity by several orders of magnitude, allowing for very precise, dynamic measurements that fully exploit all of the advantages of CARS. On the other hand, these distortions may also manifest as undesirable spectral shifts, image artefacts, or poor spectral resolution. We will characterize several of these effects in detail, highlighting their subtle origins, how they can be detected, suppressed or exploited, as appropriate, for a given experimental system.

This thesis is organized in the following manner. In Chapter 2, we review

the theory of CARS signal generation and its interaction with NRB, following the analysis of [34]. In Chapter 3, we discuss the design and development of CARS microscopes, with a particular emphasis on a "chirp-matched" CARS implementation, and address several subtle issues related to how the chirp affects the spectral resolution and the instrument calibration. In Chapter 4, we describe an intrinsic coupling between imaging artefacts and spectral distortions in a sample, and show how understanding the relative phases of the signal and the NRB, as they propagate is of critical importance to a correct interpretation of CARS spectra. In Chapter 5, we begin our discussion of spectral enhancement. In particular, we will demonstrate a tremendous CARS signal contrast enhancement in the compound astaxanthin found in the microalgae *haematococcus pluvialis*, and show how such an enhancement may be exploited for quantitative experiments. In Chapter 6, we extend our discussion of signal enhancement in astaxanthin to the NRB, and show that the FWM produced by the NRB can itself be used as a mechanism for quantitative analysis. In Chapter 7, we provide a theoretical treatment for the enhancement mechanism and discuss its implications. In Chapter 8, we discuss the application of time-correlated single photon counting to CARS microscopy, and show how this technique can be used both for signal enhancement and greater versatility for imaging. Finally, in Chapter 9 we summarize our key results.

2 Background

2.1 CARS Theory

As a nonlinear optical process, CARS may be described both classically in terms of the propagation of electric fields through a medium, or quantum mechanically in terms of the photons interacting with the dipole moment operators of the electronic energy levels. In this Chapter, we outline the classical treatment of CARS following the analysis in [35], and qualitatively comment on the quantum mechanical implications as appropriate. The propagation of electromagnetic radiation in a medium is governed by Maxwell's equations. These equations describe the relationship between electric field $\vec{E}$ and the magnetic field $\vec{H}$ in the presence of a charge distribution ρ and current source $\vec{J}$. These may be written in the form of Equation 2.1a:

$$\nabla \times \vec{E} = -\frac{\partial}{\partial t}\vec{B} \tag{2.1a}$$

$$\nabla \times \vec{H} = \vec{J} + \frac{\partial}{\partial t}\vec{D} \tag{2.1b}$$

$$\nabla \cdot \vec{B} = 0 \tag{2.1c}$$

$$\nabla \cdot \vec{D} = \rho \tag{2.1d}$$

where D is the displacement field and B is the magnetic induction. These fields are given by, respectively:

$$\vec{D} = \epsilon_0 \vec{E} + \vec{P} \tag{2.2a}$$

$$\vec{B} = \mu_0 \vec{H} + \mu_0 \vec{M} \tag{2.2b}$$

In the case of nonlinear optics, it is typical to take the magnetization density $\vec{M} = 0$, and the polarization $\vec{P} = \vec{P}^{(1)} + \vec{P}^{(\mathrm{nl})}$, where $\vec{P}^{(1)}$ describes the polarization resulting from linear interactions between the fields and the medium–that is, classical linear optics–and $\vec{P}^{(\mathrm{nl})}$ is the polarization due to any higher order–i.e. nonlinear–interactions. Combining Equations 2.1a and 2.2 in the absence of free charges ($\rho = 0$), currents ($\vec{J} = 0$) and setting $B = \mu_0 H$, we arrive at the standard wave equation for a nonlinear medium:

$$\nabla^2 \vec{E} - \frac{1}{c^2}\frac{\partial^2}{\partial t^2}\vec{E} = \frac{1}{\epsilon_0 c^2}\frac{\partial^2}{\partial t^2}\left(\vec{P}^{(1)} + \vec{P}^{(\mathrm{nl})}\right) \tag{2.3}$$

For the case of CARS, we are interested in two incoming coherent, monochromatic beams, which are generally referred to as the 'pump' and 'Stokes', representing the high and low frequency fields, respectively. We adopt a plane wave approximation for these fields, so that the pump and Stokes fields are given by Equations 2.4(a) and (b), while the outgoing anti-Stokes field is given by Equation 2.4 (c),

$$\vec{E}_p = \frac{1}{2}\big(E_p(z)e^{i(k_p z - \omega_p t)} + \text{c.c.}\big)\hat{x} \tag{2.4a}$$

$$\vec{E}_S = \frac{1}{2}\big(E_S(z)e^{i(k_S z - \omega_S t)} + \text{c.c.}\big)\hat{x} \tag{2.4b}$$

$$\vec{E}_{aS} = \frac{1}{2}\big(E_{aS}(z)e^{i(k_{aS} z - \omega_{aS} t)} + \text{c.c.}\big)\hat{x} \tag{2.4c}$$

where E_p and E_S are the field amplitudes, k_p, k_S, k_{aS}, ω_p, ω_S, and ω_{aS} are the wavevectors and frequencies of pump, Stokes, and anti-Stokes fields respectively, and c.c. indicates the complex conjugate of the preceding term. For the CARS process, the nonlinear polarization is [10]

$$\vec{P}^{(\mathrm{nl})} = \vec{P}^{(3)} = \epsilon_0 \chi^{(3)}(\vec{E}_p \cdot \vec{E}_S^*)\vec{E}_p \tag{2.5}$$

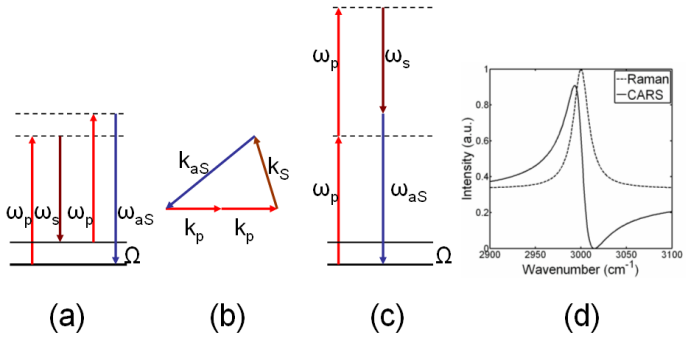

Figure 2.1: (a) The energy level diagram of CARS. This process uses the difference frequency of a pump (ω_p) and Stokes (ω_S) photons resonant on a Raman vibronic resonance Ω, followed by a second pump photon in order to generate an blueshifted anti-Stokes photon. (b) Phase matching condition for CARS, with wavevectors k representing those of the pump, Stokes, and anti-Stokes. (c) The nonresonant background produce anti-Stokes photons at an identical frequency, but shifted in phase of the CARS process. This process is detected concurrently with CARS, producing distortions. (d) Example of a resonant Raman vibronic shape (dashed line) at 3000 cm^{-1} with a spectral width of 10 cm^{-1} overlaid with the CARS spectrum (solid line) produced by this spectral line coupled to a nonresonant background where the resonant response is four times as strong as the nonresonant.

where the * operator represents complex conjugation. Substituting Equations 2.4(a) and (b) into Equation 2.5 yields a key result:

$$\vec{P}^{(3)} = \frac{1}{8}\epsilon_0 \chi^{(3)} E_p(z) E_S(z)^* E_p(z) e^{i[k_{aS}z - \omega_{aS}t]}\hat{x} + \text{c.c.} \tag{2.6}$$

where $k_{aS} = 2k_p - k_S$ and $\omega_{aS} = 2\omega_p - \omega_S$. Equation 2.6 relates the frequencies of the driving fields directly to the nonlinear polarization that, in turn, produces the forward-propagating plane wave $\vec{E}_{aS}$. The energy level diagram of the CARS process is shown in Fig. 2.1(a). From a quantum mechanical point of view, the pump excites the molecule into a virtual state, followed by immediate stimulated emission into the resonant Raman energy level at frequency $\Omega = \omega_p - \omega_S$ via a Stokes photon. Further excitation from the pump allows for a

second transition into a virtual state, producing an outgoing anti-Stokes photon with frequency ω_{aS}. Note that the anti-Stokes frequency is blueshifted relative to both pump and Stokes; this is extremely useful for analysis of CARS signals as the anti-Stokes can be filtered from excess pump and Stokes; moreover, since measurement is sensitive to the difference $2\omega_p - \omega_S$, the pump and Stokes frequencies can be judiciously chosen to avoid unwanted photodamage or linear absorption within the sample. The strength of the field is thus proportional to the square of the pump, and linearly proportional to the Stokes; it is also very sensitive to the nonlinear response $\chi^{(3)}$.

We can determine the amplitude of $\vec{E}_{aS}$ by direct substitution of Equations 2.4(c) and 2.6 into the nonlinear wave equation, Equation 2.3, neglecting the linear term $\vec{P^{(1)}}$. This yields

$$\nabla^2 \vec{E}_{aS} - \frac{1}{c^2}\frac{\partial^2}{\partial t^2}\vec{E}_{aS} = \frac{i\omega_{aS}^2}{8c^2}\chi^{(3)}E_p(z)E_S(z)^*E_p(z)e^{i[k_{aS}z-\omega_{aS}t]} \tag{2.7}$$

The left-hand side of this equation can be simplified using the slowly varying envelope approximation, which assumes that the envelope of the travelling wave varies slowly in time and space compared to the wavelength of a single optical cycle. Under such circumstances, Equation 2.7 may be reduced to a first order differential equation of the form

$$\frac{\partial E_{aS}(z)}{\partial(z)} = \frac{i\omega_{aS}}{8c}\chi^{(3)}E_p(z)E_S(z)^*E_p(z)e^{i\Delta kz} \tag{2.8}$$

where $\Delta k = 2k_p - k_S - k_{aS}$. In general, the solution to this Equation depends on the changes in amplitudes of the field strengths E_p, E_s. In practice, these fields may be treated as nearly constant, since little energy is transferred from the incident fields to the generated field [34]. Taking these values as constant,

then, allows direct integration of the anti-Stokes field E_{aS} over an interaction length L.

$$E_{aS}(L) = \frac{i\omega_{aS}L}{8c}\chi^{(3)}E_p^2E_S^*\mathrm{sinc}\big(\frac{\Delta kL}{2}\big)e^{i\Delta kL/2} \tag{2.9}$$

It is evident from Equation 2.9 that the anti-Stokes signal drops precipitiously unless $\Delta kL \approx 0$. This is the phase matching condition for CARS, shown schematically in Figure 2.1b, and simply reflects conservation of linear momentum. This condition can be satisfied using a non-collinear BoxCAR geometry and carefully matching the angles of the incident beams [18, 36]; however, it is often more practical to use a collinear geometry with a high NA (numerical aperture) lens to focus tightly into a volume significantly smaller than the coherence length $\frac{\pi}{\Delta k}$ [19]. This guarantees that CARS microscopes will always be phase matched.

We have suggested so far that $\chi^{(3)}$ describes the resonant CARS process. However, the entire analysis described above holds equally well for the competing nonresonant process illustrated in Figure 2.1(c). From a quantum mechanical perspective, this process behaves identically to CARS, producing an anti-Stokes photon at the same energy, except that the time-ordering of the second and third photons are reversed, and the process is not mediated by the Raman resonance. Thus, the nonlinear polarization is generated by two contributions: $\chi^{(3)} = \chi_R^{(3)} + \chi_{NR}^{(3)}$, where $\chi_R^{(3)}(\omega)$ and $\chi_{NR}^{(3)}$ are the contributions due to the resonant and nonresonant components, respectively, and the resonant component depends on the excitation frequency ω.. While one might expect the resonant contribution to be significantly enhanced, in practice it is possible for the nonresonant contribution to in fact be of comparable strength to the resonant term if the density of resonant oscillators is low. Moreover, there may be significant enhancements in the nonresonant contribution if it couples to an

electronic resonance. This situation is discussed in detail in Chapter 6.

The intensity of the CARS field at the detector in a collinear microscope with $\Delta kL \approx 0$ is proportional to the square of the electric field $E_{aS}(L)$, given by

$$I_{CARS}(\omega) \propto |\chi^{(3)}_{NR} + \chi^{(3)}_{R}(\omega)|^2 I_p^2 I_S L^2 \tag{2.10}$$

Equation 2.10 provides several key insights into the nature of CARS experiments. As noted previously, the intensity of the signal is proportional to the square of the pump and linear with the Stokes. The resonant signal intensity also scales quadratically with $\chi^{(3)}_R$, which in turn, is proportional to the concentration of oscillators. Due to the interference between CARS and the NRB, however, the combined signal may not follow this quadratic dependence. In the regime where $\chi^{(3)}_{NR} >> \chi^{(3)}_R$, the resonant signal will be approximately linear with concentration. Because of this transition region, it can be difficult to accurately measure concentrations from CARS microscope measurements except in the regions where the signal is very strong or very weak. Reducing the concentration to a linear dependence can be achieved using various methods, including the Kramers-Kronig retrieval discussed in Chapter 2.2.

In the simplest case, we can treat a Raman resonance as a Lorentzian of the form of Equation 2.11

$$\chi^{(3)}_R(\omega) = \chi^{(3)}_{R0} \frac{1}{\Omega_R - (\omega_p - \omega_S) - i\Gamma} \tag{2.11}$$

In this equation, $\chi^{(3)}_{R0}$ is the Raman amplitude, and Γ is half of the spectral linewidth. As the frequency of the incoming beams approaches the resonant frequency, the denominator becomes large, but complex; the nonresonant contribution, on the other hand, is purely real. The imaginary part of $\chi^{(3)}_R$ intro-

duces a phase shift between the resonant and nonresonant fields, which interfere due to the cross-term in Eq. 2.10, even in the case of a constant, but non-zero, NRB, which is generally always real. Fig. 2.1(d) shows a resonant Raman spectral line (dashed) of the form of Eq. 2.11 with a width 10 cm^{-1} centred at 3000 cm^{-1}, overlaid with the generated CARS spectrum of the form of Eq. 2.10 (solid line) of the same peak with a constant nonresonant background, and a resonant-to-nonresonant intensity ratio of 4:1. As can be seen from the Fig. 2.1(d), the CARS spectrum adopts a dispersive lineshape with a peak that is redshifted relative to the Raman line and a corresponding reduced intensity. For spectroscopy of isolated lines or contrast imaging, the raw CARS spectrum is often sufficient; however, for congested regions or very accurate measurements of Raman lineshapes, it is often necessary to use one of several deconvolution algorithms devised to separate the Raman spectrum from the nonresonant background, as discussed in the following section.

2.2 Raman Retrieval

In Chapter 2.1, it was shown that the response at a far-field detector is the coherent sum of the vibrationally resonant CARS signal $\chi_R^{(3)}$ and the NRB $\chi_{NR}^{(3)}$. Expanding Equation 2.10 reveals that the resonant response and the NRB contributions to the signal are in fact coupled at the detector:

$$I_{CARS}(\omega) \propto |\chi^{(3)}(\omega)|^2 = |\chi_{NRB}^{(3)}|^2 + |\chi_R^{(3)}(\omega)|^2 + 2\chi_{NRB}^{(3)}\Re[\chi_R^{(3)}] \qquad (2.12)$$

The coupling term between the resonant response and the NRB accounts for most of the undesirable properties of CARS. First, it results in significant distortions to the CARS spectrum, yielding the dispersive lineshape shown previously in Figure 2.1(d). The lineshape and position of the spectral peak are shifted

relative to the spontaneous Raman spectrum, greatly increasing the difficulty in interpreting spectral features compared to the wealth of previously established Raman spectra found in the literature. Because CARS and the NRB are coherently generated, linear deconvolution techniques cannot be used to separate the desired response from the undesirable NRB, nor are any simple background subtractions possible [37, 38]. Finally, the signal intensity does not vary linearly with the number of oscillators, but rather varies from linear to quadratic depending on the relative strengths of $\chi_R^{(3)}$ and $\chi_{NRB}^{(3)}$.

For an isolated Raman resonance, $\chi_R^{(3)}$ may be treated as a Lorentzian function of the form of Equation 2.11. By contrast, the intensity of spontaneous Raman scattering is given by: [39]

$$I_{Ram} \propto \frac{\Gamma}{(\Omega_R - \omega)^2 + \Gamma^2} \tag{2.13}$$

Comparing Equations 2.11 and 2.13 reveals that the imaginary part of $\chi^{(3)}$ is directly proportional to the spontaneous Raman intensity, i.e. $\Im\left[\chi^{(3)}\right] \propto I_{Ram}$, where $\Im$ represents the imaginary part. The imaginary part of the CARS response contains all of the relevant information required to extract the spontaneous Raman spectrum. It is useful to write $\chi^{(3)}$, then, in terms of a spectral phase $\varphi(\omega)$ that accounts for the relative contributions of the signal in the real and imaginary planes by Equation 2.14 [33].

$$\chi^{(3)}(\omega) = \left|\chi^{(3)}(\omega)\right| \exp(i\varphi(\omega)) \tag{2.14}$$

For reasons that will be made clear shortly, it is convenient at this point to divide Equation 2.14 by the nonresonant background, $\chi_{NRB}^{(3)}$, which we assume to be positive and real-valued for all ω. We then take the logarithm of both

sides of the equation to get

$$\ln\left(\frac{\chi^{(3)}(\omega)}{\chi^{(3)}_{NRB}(\omega)}\right) = \ln\left(\frac{\left|\chi^{(3)}(\omega)\right|}{\chi^{(3)}_{NRB}(\omega)}\right) + i\varphi(\omega) \tag{2.15}$$

The real and imaginary parts of Equation 2.15 can be related to each other through use of the Hilbert transform, $\mathscr{H}$, which is defined as follows:

$$\mathscr{H}(f(\omega)) \equiv \frac{1}{\pi}\mathscr{P}\int_{-\infty}^{\infty}\frac{f(\omega')}{\omega-\omega'}\mathrm{d}\omega' \tag{2.16}$$

Here $\mathscr{P}$ is the Cauchy principal value of the integral, which, in turn, is defined as

$$\mathscr{P}\int_{-\infty}^{\infty} f(x)\mathrm{d}x \equiv \lim_{\rho\to\infty}\int_{-\rho}^{\rho} f(x)\mathrm{d}x \tag{2.17}$$

Note that the limit in Equation 2.17 may be finite even for functions that are, in principle, not integrable over this domain. For example $\int_{-\infty}^{\infty} x\mathrm{d}x$ is undefined, but $\mathscr{P}\int_{-\infty}^{\infty} x\mathrm{d}x = 0$. The Hilbert transform has the effect of inducing a 90^o rotation of a real function into the complex plane, and a corresponding rotation of an imaginary function back into the real plane. This type of relationship brings to mind the Kramers-Kronig relations for the linear optical susceptibility $\chi(\omega) = \chi_1(\omega) + \chi_2(\omega)$, which can be related directly by the Hilbert transform:

$$\chi_1(\omega) = \mathscr{H}(\chi_2(\omega)) \tag{2.18a}$$

$$\chi_2(\omega) = -\mathscr{H}(\chi_1(\omega)) \tag{2.18b}$$

In an analogous manner, the real and imaginary parts of Equation 2.15 are likewise the Hilbert transformations of each other and can be related in an identical manner to Equation 2.18. The spectral phase can therefore be written

expressly in terms of $\chi^{(3)}$ in the following manner:

$$\varphi = -\frac{1}{\pi}\mathscr{P}\int_{-\infty}^{\infty}\frac{\ln\left(\frac{\left|\chi^{(3)}\right|}{\chi^{(3)}_{NRB}}\right)}{\omega-\omega'}\mathrm{d}\omega' \tag{2.19}$$

We note that as $\omega \to \infty$, $\frac{|\chi^{(3)}|}{\chi^{(3)}_{NRB}} \to 1$, so the integral in Equation 2.19 is convergent, which would not necessarily be the case for $\chi^{(3)}$ alone. Moreover, we note that Equation 2.19 is written expressly in terms of observables, namely $|\chi^{(3)}|$, which is related to the intensity of the generated response via Equation 2.12, and $\chi^{(3)}_{NRB}$, which in many samples we can extract by measuring the NRB response due to the solvent, or by focusing the microscope objective into the glass cover slide. We note that the results generated from the approach outlined above [40] are quite similar the time-domain Kramers-Kronig relations used in the literature [33]; however, the use of Hilbert transforms as opposed to Fourier transforms and the explicit introduction of $\chi^{(3)}_{NRB}$ makes the derivation much more straightforward.

In Figure 2.2, we provide an illustration of this process. Highlighted in black is a raw CARS spectrum of neat nitrobenzene in the fingerprint region from 800 cm^{-1} to 1850 cm^{-1}. This is overlaid with the spontaneous Raman spectrum (blue) as measured directly through a Raman spectrometer. It can be clearly seen that both the peak positions, their shapes, and their relative heights are considerably distorted in the CARS spectrum compared to Raman. Overlaid upon these in red is the retrieved Raman spectrum of nitrobenzene using the algorithm described above. As can be seen, the positions, relative heights and shapes of the retrieved spectrum are much more accurate than that of the raw CARS. It should be noted that the spectral resolutions between the Raman and the CARS are quite different (~ 3 cm^{-1} vs. ~ 30 cm^{-1}, respectively), so there is necessarily some broadening of the CARS spectrum due to the relatively poor

resolution in this case. Otherwise, however, the agreement is very good.

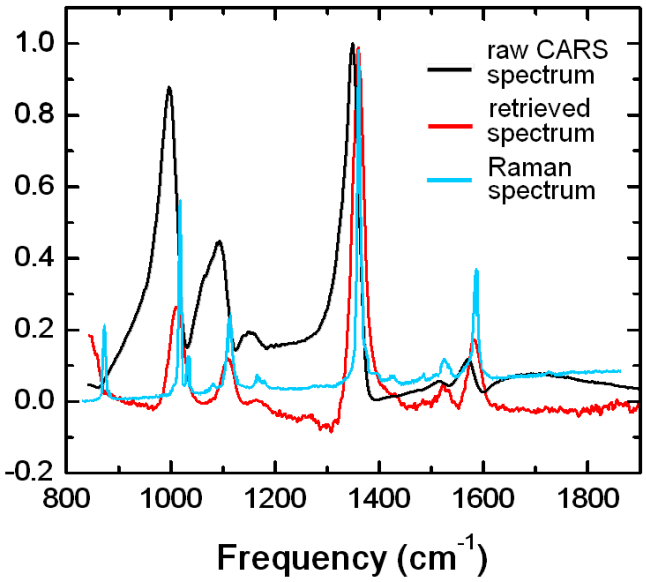

Figure 2.2: The collected spectra of nitrobenzene using CARS (black), CARS after a retrieval via the Hilbert transform (red), in comparison to the spontaneous Raman spectrum of nitrobenzene (blue). The intensities of the three spectra have been scaled to match that of the 1346 cm^{-1} peak.

Unfortunately, perfect agreement between the retrieved Raman and spontaneous Raman spectra may not always be possible in practice. For objects whose size is significantly smaller than the focal volume of the microscope objective, additional spectral distortions may be introduced due to such things as spatial interference, refractive index mismatch, and the Gouy phase shift. This latter problem will be discussed in more detail in Chapter 4.

3 CARS Microscope Implementation

3.1 Overview of CARS Microscopy Implementations

Much of the recent interest in CARS can be attributed to the microscope developed by Zumbusch et al [19]. Their CARS microscope presented several important innovations that have become the cornerstones of modern CARS microscopes. First, the system made use of a tightly-focused, high NA lens to restrict the interaction volume to only a small focus. The tight focusing conditions greatly relaxed the phase matching conditions discussed in Chapter 2, allowing for three-dimensional sectioning of the sample. Moreover, this design made use of femtosecond NIR pulses, which, unlike the visible light pulses used in previous work [18], are generally below any electronic resonances within the sample and thus avoid potential problems of resonance enhancement of the NRB. This original system made use of synchronized femtosecond pulses trains from an optical parametric oscillator (OPO) system to generate the pump and Stokes colours. This design limited the scanning range to a relatively narrow frequency range (2600-3300 cm^{-1}), and the OPA needed to be manually tuned to change frequencies, limiting scans to only a small number of data points.

It was noted early in the literature that the transform limited femtosecond pulses used in this original design significantly reduced the contrast of the microscope system [41]. While femtosecond pulses have higher peak intensity, the interaction bandwidth of two transform-limited femtosecond pulses is significantly larger than the spectral width of a typical Raman line and only the components of the pulses within that bandwidth may contribute to CARS, whereas all of the components contribute to the NRB. Consequently, much of the fs bandwidth is wasted in the sense that it only enhances the NRB, not the resonant vibrational transition. It should be noted, however, that this argument applies only to transform-limited pulses, and not necessarily to other (e.g.

chirped) pulse shapes. A natural improvement, then, was thought to be to move to frequency-locked picosecond pulses. Picosecond pulses have a much narrower interaction bandwidth and, consequently, the energy may be more concentrated into the Raman linewidth of interest, thus increasing the signal-to-noise and the spectral resolution simultaneously. Moreover, the lower peak powers and longer pulse widths of picosecond pulses generally reduce photodamage and improve sample viability [42]. An implementation making use of two tunable picosecond lasers, or picosecond laser pumping a tunable OPO have become the standard designs in many labs worldwide [35, 24].

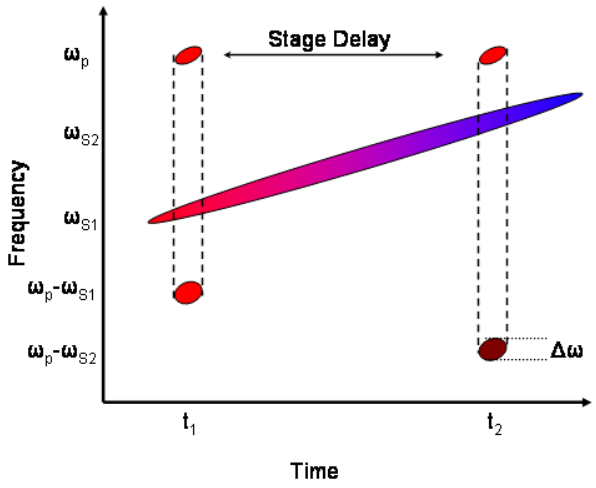

Figure 3.1: A chirped pump pulse ω_p interacts with a chirped Stokes pulse. At t_1, the pump interacts with the Stokes at the instantaneous frequency ω_{S1}. By changing the delay to t_2, the pump instead interacts at frequency ω_{S2}. Thus changing the delay allows for spectral scanning. The resolution in this case is $\Delta\omega$.

While it was argued that CARS generally benefited from picosecond pulses, it is notable that many other nonlinear optical processes generated concurrently to CARS, such as SHG and two-photon excited fluorescence (TPEF), benefit from shorter pulses [10], and thus for a system designed to interrogate one or

more of these additional modalities (a multimodal system) femtosecond pulses would in fact be preferable. It was proposed that the spectral resolution of CARS using fs pulses could be vastly improved using so-called "spectral focusing" [43]. Spectral focusing involves introducing a linear chirp into each of the pump and Stokes arms using, for example, blocks of highly dispersive glass. By introducing linear dispersion into the system, the blue components of the pulses are delayed with respect to the red, stretching them in time as shown in Figure 3.1. As a result of this introduced chirp, only the instantaneous bandwidth of the time-overlapped pulses will interact. The reduced interaction bandwidth greatly improves the spectral resolution and the signal-to-noise, effectively grafting the advantages of the ps system into a fs implementation. By judiciously choosing the lengths of glass in the two arms to match the chirp parameters of the pump and Stokes, it is possible to have comparable spectral resolution to ps systems while maintaining the high peak powers of fs systems for SHG and TPEF. Using two blocks of SF_{57} glass of appropriate lengths in the pump and Stokes arms, the spectral resolution in a chirped 100 fs system could be improved to 8 cm^{-1} [44]. In addition, the larger bandwidth of the pulses allowed for a broad spectral range to be probed, which could be easily, and, more importantly, rapidly, tuned simply by changing the relative delay between the pump and Stokes arms using a mechanical delay stage.

Even using a 100 fs system, the tuning range for a CARS system is limited by the bandwidths of the two pulses, in the above case limited to about 1000 cm^{-1}. While it has been recently demonstrated that with a pulse width as narrow as 5 fs, it is possible to span nearly the entire Raman vibrational region from $\sim$1200 cm^{-1} to $\sim$3800 cm^{-1} [45], the significant increase in peak intensity and difficulty in generating such short pulses make this option somewhat unpalatable for many biological applications. An alternative approach is to generate

the broad Stokes pulse through use of a photonic crystal fibre (PCF). A PCF such as the FemtoWhite CARS (NKT Photonics) used in our system produces an extremely broad NIR pulse spanning from 950-1250 nm, effectively equivalent to that of an $\sim$ 12 fs pulse. The added bandwidth supplied by the fibre allows for a much broader tuning range, at the expense of Stokes power per unit bandwidth compared to OPO or synchronized source based systems [46]. Using this implementation, it was demonstrated that a tuning range of 1600 cm^{-1} with a spectral resolution, optimized for CARS in lipids, of 60 cm^{-1} could be achieved with simultaneous generation of TPEF and SHG in a rabbit aeorta. Unfortunately, rather than a transform limited pulse, the PCF produces an extremely non-uniform distribution in the Stokes power-spectral-density (PSD). While this can significantly complicate the analysis of generated spectra from these systems, it may also be advantageously used to stretch the spectral range of the system in order to access Raman lines that are at the edge of the tuning range of the pump laser [47]. The Stokes spectrum is discussed in more detail in Chapter 3.4.

3.2 Chirp-Matched CARS Microscope Design

The CARS microscope design in our lab makes use of a simplified version of the femtosecond "chirp-match" design described in Ref [47]. The system is driven by a single Mira900 (Coherent) oscillator pumped [48] by a Verdi-12 (Coherent) 532 nm source laser [49]. The standard operating power of the Verdi laser is 8.5W, leading to a typical output power of 0.97 W from the Mira900 with a 14-15 nm bandwidth at 800 nm. The power tends to decrease as a function of wavelength, yielding an output power of only 0.55 W at 915 nm for the same spectral bandwidth. The laser is mode-locked, producing 60 fs pulses at a repetition rate of 80 MHz. The laser light is directed into a beamsplitting cube

to produce beams corresponding to the pump and Stokes, respectively. The relative powers of these two arms may be adjusted via a polarizer in front of the beamsplitter.

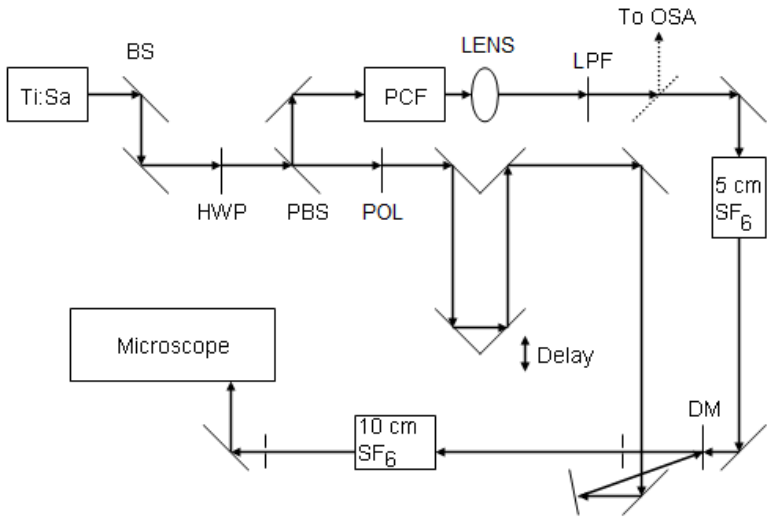

Figure 3.2: Multi-modal CARS microscopy setup. A Ti:Sa laser produces a pulse train that is split into two arms using a polarizing beam splitter (PBS), whose relative intensities are controlled by a half-wave plate (HWP). The pump portion can be attenuated by a stage-controlled polarizer and then is directed into an electronically controlled motorized delay stage. The Stokes light is coupled into a photonic crystal fibre, producing a supercontinuum. This light is collimated by a lens and filtered by a long-pass filter (LPF). The light can be routed into an optical spectrum analyzer (OSA), or passed through a block of SF_6 glass. The beams are recombined on a dichroic mirror (DM), passed through a larger block of SF_6 glass before being routed into the microscope.

The Stokes light is coupled into a FemtoWhite CARS (NKT Photonics) [50] photonic crystal fibre to produce a broad supercontinuum. Careful alignment of the fibre is necessary to ensure proper coupling. Typical coupling efficiencies using this system are between 35-41%. The <950nm light from the Stokes supercontinuum is filtered using a set of long-pass filters and the transmitted light is directed onto a dichroic mirror. Simultaneously, the pump light is passed

through a computer controlled polarizer that allows for precise calibration of the power at the microscope, then directed through a variable delay stage. The pump light is filtered by a long pass filter (<800 nm for C-H and <830 nm for fingerprint) and recombined with the Stokes light on the dichroic mirror. A 5 cm block of high-dispersion SF_6 glass is added to the Stokes arm and a 10 cm block of SF_6 added to the combined beam arm in order to introduce linear chirps, such that the CARS response will have a $\sim$30 cm^{-1} spectral resolution using an 815 nm pump. The matched chirp rates of the pump and Stokes allows for both efficient signal generation and optimization of the spectral resolution [44]. Moreover, by translating the delay stage between pump and Stokes, we change the instantaneous interaction bandwidth between the pulses, and thus have rapid and facile spectral scanning capability. The light is directed into a modified FV300 Fluoview microscope (Olympus) [51] to allow for descanned detection of the forward-generated CARS, SHG, or SFG signals into fibre-coupled off-board photomultiplier tubes (PMT), while fluorescence is collected concurrently in the backward direction using a separate PMT (Hamamatsu) [52]. At the input to the microscope, a 830-25 notch filter is added for fingerprint detection; in the forward direction, a 730 short pass or 809-81 bandpass filter is used for, respectively, C-H and fingerprint implementations to filter out unwanted pump signals. The microscope design is summarized in Figure 3.2. See Appendix A for details on the alignment procedure.

Images are collected using a commercial FluoView software (Olympus) [51] that is augmented by several home-built LabView programs to synchronize the scanning galvos with the translation stage. The typical pixel dwell time for the system is 2 μs, resulting in an image generation rate for a standard 256$\times$256 pixel image of about 0.5s per frame.

3.3 Translation Stage Calibration

Due to the chirp introduced into the pump and Stokes arms, changing the relative timing between the pulses will change the instantaneous frequency difference between them. This timing is controlled by a motorized delay stage, so it is necessary to create a calibration between the stage position and the corresponding frequency difference. Since the chirp is approximately linear (except at the edges of the Stokes bandwidth), this should be fairly straightforward. Unfortunately, the difference frequency is difficult to measure directly, and, as will be discussed in the following sections, using other measurements as proxies for the difference frequency requires some care, as the underlying nonlinearities of these processes may produce erroneous calibrations. These issues are subtle, and we believe that they have been largely overlooked in the literature.

Direct Peak Interpolation

The simplest calibration method is to simply choose a sample with two (or preferably more) strong Raman peaks in the spectral window of interest. Then, by scanning the spectrum, one can attain a calibration simply by assigning those peaks to their corresponding values in the literature, and interpolate between them. While this is by far the simplest method to calibrate the spectrum, it is also relatively inaccurate. Due to the spectral distortions described in Chapter 2.1 (and those in Chapter 4), the peak positions in the CARS spectrum will be redshifted relative to their true positions in the Raman spectrum by up to their spectral linewidth, typically a few tens of wavenumbers, which can lead to corresponding calibration errors of similar magnitude, depending on the shifts and the number of peaks used. In order to generate an accurate calibration using this method, either the Raman spectrum must be retrieved using the Hilbert transform methods of Chapter 2.2, or the signal intensities must be sufficiently

large that the nonresonant background is negligible compared to the resonant CARS response. In the former case, the quality of the calibration will depend entirely on the reliability of the retrieval algorithm. The latter case requires a specific sample to be found that meets this condition. In the fingerprint, one option would be astaxanthin, which, as discussed in Chapter 5, has an anomalously large CARS response and minimal nonresonant background.

Calibration by Sum-Frequency Generation

The microscope system can be calibrated using the forwarded-generated SFG from powdered (ie. monocrystalline) KDP (Monopotassium dihydrogen phosphate), a well-known nonlinear optical material. SFG is produced by the interaction of the pump and Stokes, generated at a frequency given by $\omega_{SFG} = \omega_{pump} + \omega_{Stokes}$. For an 800 nm pump and 1050 nm Stokes, the expected SFG frequency is 454 nm. The SFG peak can be measured directly by coupling a spectrometer to the fibre output. As with CARS, since the interaction regime depends only on the instantaneous bandwidth, by tuning the relative delay between the pump and Stokes, we can move the SFG peak, and therefore calibrate the stage. This process applies across the entire Stokes bandwidth.

Figure 3.3(a) shows a typical SFG calibration using this method. Curiously, there appears to be "wobble" in the calibration curve that greatly increases the standard error. That is, the calibration is not strictly linear, but rather there is some sinusoidal variation in the the instantaneous bandwidth that can be observed. This effect is reproduceable and systematic. This may be a result of the focussing optics: SFG manifests at several orders in the diffracting plane over a relatively broad range of angles in our collinear geometry [10, 53]; if the condensor optics are unable to collect the SFG signal entirely, this may result in systematic errors in the ability to accurately use SFG calibration. There are other concerns in SFG calibration as well. In Figure 3.3(b), we show the SFG

spectrum of KDP taken at three different stage delays using a 900 nm pump and the broadband Stokes supercontinuum. In this region, we see that the SFG response is highly non-uniform, in some case containing multiple peaks, and hence the full-width at half-maximum of the SFG spectrum is unclear and it is difficult to accurately assign the position of the peak. It is likely that this is due to the non-uniform nature of the Stokes light (see Chapter 3.4) from the supercontinuum manifesting itself in the cross-correlation of pump and Stokes. Moreover, the close proximity of the SFG signals at 470-495 nm to the SHG from the pump (450 nm) and Stokes ($\sim$ 525 nm) severely limit the effective interaction bandwidth in this case. This greatly reduces the reliability of SFG calibrations, which are, on the whole, not recommended.

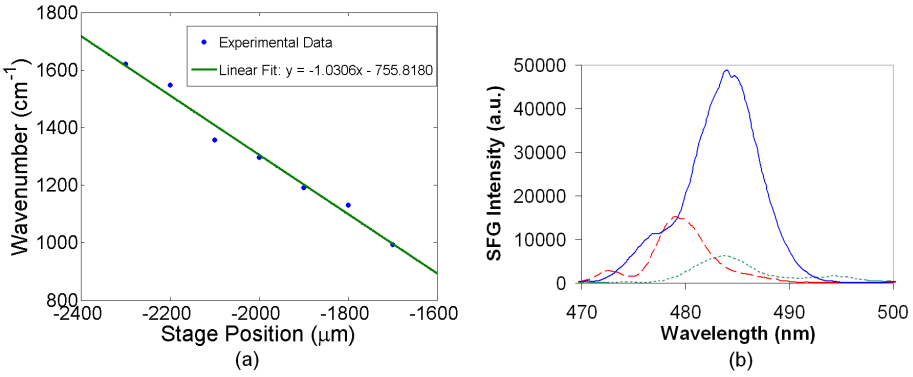

Figure 3.3: (a) Calibration of the translation stage using SFG at 900 nm. In this case, the slope of the calibration was found to be -1.0306 μm/ cm^{-1}, which can be taken as a proxy for the negative of the rate of chirp. In this case, two of the data points are notably above the linear fit and one decidedly below it, forming the characteristic "wobble" in SFG calibrations. (b) SFG Spectra of KDP at three difference stage positions. Note the significant shoulder on the blue side of both the solid and dashed curves, making the full-width at half maximum remarkably more difficult to identify.

Calibration by Four-Wave Mixing

The ideal calibration method involves the use of four-wave mixing within a non-resonant sample. Four-wave mixing can be produced either by a sample with sufficient enhancement of this process, such as astaxanthin as discussed in Chapter 6, or simply by applying a very large ($>$ 200 mW) pump power onto a vibrationally nonresonant sample such as a glass slide, and measuring the spectrum of the NRB. With the spectrometer connected to the condensor, it should be possible to observe a FWM response from glass, lens immersion oil, or other NRB samples. Depending on the pump power, Stokes intensity variations, detector sensitivity, and $\chi^{(3)}_{NRB}$ of the sample, it is possible that only a fraction of the stage delay may be measured as the FWM in most samples is very weak. Nonetheless, by measuring the anti-Stokes wavelength of the FWM light and the pump wavelength, the frequency difference between pump and Stokes can be calculated for a given stage delay. An example of this is shown in Figure 3.4(a) for a 815 nm pump. The corresponding anti-Stokes spectra at various delays are shown in Figure 3.4(b). The anti-Stokes calibration has a much lower error (less than 1% error in the slope for 10 data points) than the SFG calibration ($>$ 5% error in the slope for 10 data points), and the anti-Stokes spectra are much more uniform and less sensitive to the variations in the Stokes spectrum. Generally, then, direct measurement of the anti-Stokes spectrum using a spectrometer as a function of stage position provides the best calibration method with a minimum of difficulty.

3.4 Stokes Generation

The Stokes light for our system is produced via a FemtoWhite CARS photonic crystal fibre. This fibre is characterized by two zero-dispersion wavelengths (ZDW) at 775 nm and 945 nm. Upon pumping with laser light between these

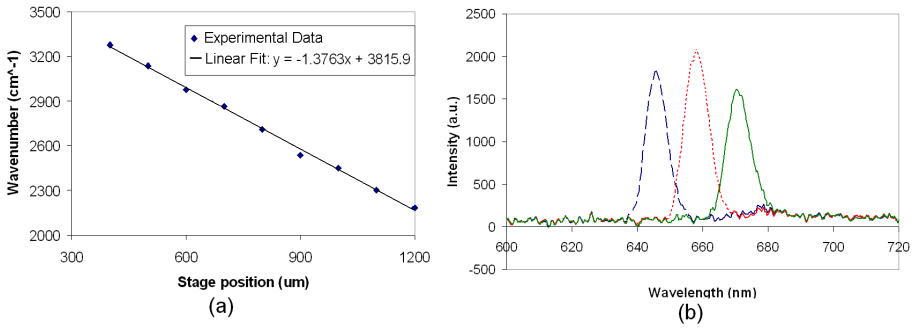

Figure 3.4: (a) Calibration of the translation stage using FWM of astaxanthin using an 815 nm pump. The slope of the calibration is found to be -1.3763 μm/ cm^{-1}, which may be taken as a proxy for the chirp rate at this pump wavelength. (b) FWM Spectra of astaxanthin three different stage positions.

wavelengths, self-phase modulation and FWM within the fibre produce a very broad supercontinuum spectra in the < 775 nm and > 945 nm regions, both of which are typically 300-400 nm wide [54]. Unlike fibres with one ZDW where supercontinuum generation may only occur when the pump wavelength is below the ZDW [55], this fibre may be pumped anywhere between the two ZDW with varying chirps and the output power and bandwidth of the fibre will not change significantly [54]. The fibre efficiently converts energy into the NIR region from 1000-1350 nm, although rapid variations of more than a factor of ten or more in intensity at any given frequency can result in a highly nonlinear spectrum [47, 56]. Thus it is necessary to monitor the Stokes spectrum resulting from the fibre using an optical spectral analyzer (OSA). Figure 3.5 shows several traces of the Stokes spectrum at a fixed pump wavelength and power taken at three hour intervals. Note that there can be substantial day-to-day differences in the Stokes spectrum due to drift in the laser pointing, vibrations, or noise in the system. The spectrum can also be altered considerably by changing the input power or polarization, which can be used to optimize the signal intensity in a particular spectral region. Notably, as the Stokes input power decreases, the

peak of the power-spectral density (PSD) of the PCF shifts closer to the ZDW. In our current configuration where there is considerable difficulty in tuning the pump laser beyond 925 nm, and our detector sensitivities fall off precipitiously above 850 nm for the anti-Stokes. Therefore, in order to maximize the signal intensity in the lowest energy regions of the fingerprint (< 1000 cm^{-1}), we can decrease the input power to the PCF from our typical usage of 150-200mW to 30-40 mW, in order to selectively enhance the shorter wavelength NIR components in the Stokes spectrum [47].

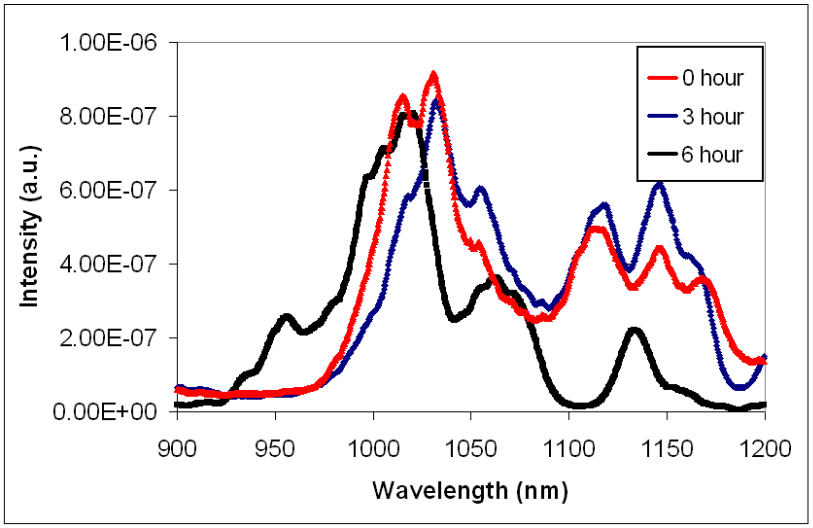

Figure 3.5: Recorded Stokes spectra taken at regular intervals using the optical spectrum analyser. No changes to the laser system were otherwise made during this period; the observed variations are purely a result of instabilities in the fibre coupling.

Because the CARS intensity of any given component of the CARS spectrum depends linearly on the PSD of the Stokes, the overall CARS spectrum will not faithfully reproduce the intensities of the underlying Raman components. Rather, the CARS intensities (as well as four-wave mixing, SFG and non-degenerate two-photon fluorescence) will be proportional to the variations

in the intensity of the Stokes beam. In order to reproduce accurately the peak intensities of the CARS spectrum, it is therefore necessary to collect a Stokes spectrum using an optical spectrum analyser (OSA) following each scan, and divide the CARS peaks by their relative intensities in the Stokes spectrum. The variations in the Stokes spectrum can, in principle, change the intensity of a given CARS peak by a factor of 10 or more, so comparing the intensities of peaks without taking this effect into account could lead to very erroneous conclusions.

3.5 Chirp Matching

The electric field due to a transform-limited Gaussian pulse of centre frequency ω_j and with pulse width Δ_j is given by Equation 3.1, where j may represent the pump (p) or Stokes (S) as appropriate

$$E_j \propto \exp\Big(\frac{-t^2\pi^2\Delta_j^2}{(2\ln 2)^2}\Big)\exp(i\omega_j t) \tag{3.1}$$

When this pulse passes through a dispersive medium of length z, there is a frequency-dependent delay of the radiation due to dispersion. The frequency of the light is given by $\omega(t) = \omega_j + 2\beta t$ for chirp β. For dispersive materials whose lengths z are long compared to $\frac{\tau_0^2}{|k''|}$, where τ_0 is the pulse FWHM and k'' is the group-velocity dispersion of the material, the chirp can be determined by $\beta^{-1} \approx 2z|k''|$ [44]. The GVD, in turn, can be calculated from the Sellmeier equations using known coefficients found in the literature [57]. The resulting chirped pump pulse now takes the form

$$E_j \propto \exp\Big(\frac{-t^2\pi^2\Delta_j^2}{(2\ln 2)^2 + a_j^2}\Big)\exp\Big(i\omega_j t + i\big(\frac{-t^2\pi^2\Delta_j^2 a_j}{(2\ln 2)^2 + a_j^2}\big)\Big) \tag{3.2}$$

where a_j is the dimensionless chirp parameter of the pulse, given by $a = \Delta^2\beta^{-1}$.

We consider the interaction of the fields in the CARS process, $E_p^2 E_S^*$ using chirped pulses. In this case, the field is given by

$$E_p^2 E_S^* \propto \exp\Big[\frac{-t^2\pi^2}{(2\ln 2)^2}\Big(\frac{2\Delta_p^2}{(2\ln 2)^2 + a_p^2} + \frac{\Delta_S^2}{(2\ln 2)^2 + a_S^2}\Big)\Big] \times \exp\Big[i(2\omega_p - \omega_S)t + it^2\pi^2\Big(\frac{2\Delta_p^2 a_p}{(2\ln 2)^2 + a_p^2} - \frac{\Delta_S^2 a_S}{(2\ln 2)^2 + a_S^2}\Big)\Big] \quad (3.3)$$

We note several general features of interest in Equation 3.3. The phase term depends both on the anti-Stokes frequency, $2\omega_p - \omega_S$ and a quadratic phase term depending both on the widths of the pulses, and the chirp parameters a_p and a_S. The envelope is Gaussian, with an effective width given by the term in parenthesis. The added chirp effectively lengthens the pulse duration, i.e. it improves the spectral resolution–compared to the unchirped case where $a_p = a_S = 0$. The effective spectral resolution of the anti-Stokes can therefore be calculated as

$$\Delta^2_{\text{effective}} = \Big(\frac{2\Delta_p^2}{1 + \big(\frac{a}{2\ln 2}\big)^2} + \frac{\Delta_S^2}{1 + \big(\frac{b}{2\ln 2}\big)^2}\Big) \quad (3.4)$$

Previous analysis of this problem only considered the interaction of a single pump field with the Stokes and neglected the effect of the second pump field [44, 46]. Under this simplification, it is clear that the optimal spectral resolution is achieved when $a = b$; however, the more complete Equation 3.3 reveals that this approximation will result in the Stokes being under-chirped relative to the pump. Rather, the chirp that maximizes the spectral resolution is given by

$$a = \sqrt{(2\ln 2)^2 + 2b^2} \quad (3.5)$$

Figure 3.6(a) shows that for a fixed introduced chirp $C = a + b$, the optimal

spectral resolution is slightly greater than the traditional chirp-matched case. Assuming that the pump and Stokes pulses are 100 cm^{-1} each with a total chirp $a + b = 10$, we see that the optimal spectral resolution of 41 cm^{-1} in this case occurs when the Stokes is overchirped by 2.6 relative to the pump. Overall, the trend suggests that it is generally favourable to be slightly over-chirped in the Stokes ($b > a$) rather than under-chirped ($b < a$), as the spectral resolution increases more rapidly for under-chirped pulses than for over-chirped ones. Experimentally, as shown in Figure 3.6(b), we see that the spectral resolution as a function of chirp has an asymmetric pattern. The best spectral resolution experimentally was found at the $a = b$ condition, but we note that a significant increase in Stokes chirp from the traditional chirp match condition to a mismatch of 2×10^4 fs^2 of added dispersion in the Stokes does not result in an appreciable change in the spectral resolution. This suggests that, at the very least, this region is very flat, and the shape of the curve may indicate that there is a minima somewhere between these two points. Unfortunately, the glass we have available to us does not allow us to interrogate this region. The model does not capture the experimental data particularly well except for a very rough qualitative agreement of the general trend. This is likely due to the fact that the simple analysis above assumes that both the pump and Stokes pulses are Gaussian in shape, when, as discussed above, the Stokes has a highly non-uniform character that is difficult to model analytically.

This analysis thus provides a simple method to determine the required length of glass to achieve a particular spectral resolution for given pump and Stokes wavelengths. For a given desired spectral resolution, the required chirps, and hence, the lengths of glass of a given material necessary to achieve those chirps, can be calculated using Equations 3.4 and 3.5. Generally, a better spectral resolution will require a larger chirp, and thus, more glass. This does introduce

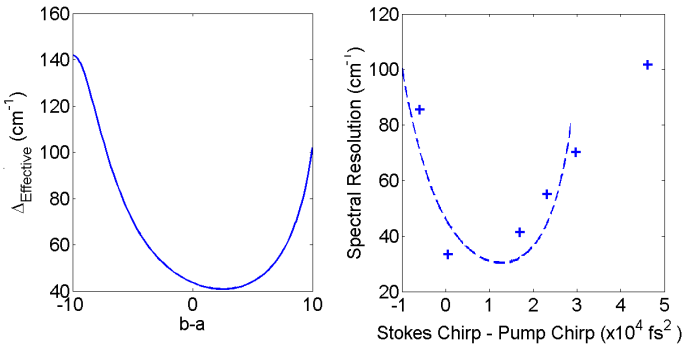

Figure 3.6: (a) Effective spectral resolution of chirp on pump/Stokes pulses measuring 100 cm^{-1} each, where the total chirp is fixed at a+b = 10, and the difference is allowed to vary. This is equivalent to having a fixed amount of glass, and moving it between the pump and Stokes arms. (b) Experimentally measured data of the spectral resolution measured as a function of the Stokes - pump chirp rates for our microscope system. The dashed line shows the fit of (a)

some practical limitations as significantly longer pieces of glass will result in a loss of transmission through the sample, though spectral resolutions of 8 cm^{-1} have been measured with better than 70% transmission [44], which is sufficient for most practical purposes. Thus, in principle, it is not necessary to match the chirps as adding additional glass into either arm will tend to improve the spectral resolution through Equation 3.4, in practice it is far more efficient to achieve superiour spectral resolutions if the chirps are matched or nearly matched.

4 Spatial-Spectral Coupling in CARS Microscopy

4.1 Introduction

One of the key advantages to CARS microscopy is the ability to visualize microscopic objects in three-dimensional space, while simultaneously performing spectroscopic measurements on specific regions of interest within a sample. This technique, called hyperspectral CARS, allows for detailed spectroscopic information to be extracted from specific regions within a sample, which can provide significant insight into local dynamics or chemistry within the specimen [47, 58, 59, 60]. This is due to the fact that Raman peaks have long since been recognized to experience small shifts in amplitude and frequency due the effects of temperature [61], salinity [62], functionalization and isomerization [63]. These changes, when localized within specific regions in an inhomogenous sample, allow visualization and analysis of local dynamics and chemistry.

Unfortunately, because CARS is a coherent process, the generated signals within the focal volume, their propagation to, and interference at the detector may not necessarily reflect the true nature of the sample. For example, shadows have been observed in CARS microscopy images that have been associated with interference effects [37, 38], linear refractive index mismatch [64], and the Gouy phase shift [28]. Moreover, as described in Chapter 2.1, CARS spectra are also distorted due to the presence of the nonresonant background, and require a post-processing retrieval to decouple the resonant Raman response from the background. Previous work has not, however, considered the possibility that these effects are coupled: That spatial distortions in the image may be linked to a corresponding distortion in the spectrum. In this Chapter, such spatial-spectral couplings are investigated in detail using a combination of theory and experiment. We will demonstrate conclusively that within the Rayleigh length of the laser, there is an intrinsic coupling between the position of an object

within the laser focus, and distortions to its CARS spectrum. Furthermore, the observed spectral distortions persist even after retrieval through common methods (e.g. Kramers-Kronig).

4.2 Theory

We begin by deriving a relation to relate phase shifts, particularly the Gouy phase, to the CARS intensity I_{CARS}. Consider an object of diameter D that has a Raman resonance at frequency Ω with suspectibility $\chi_R^{(3)}$ embedded in a nonresonant medium with susceptibility $\chi_{NR}^{(3)}$ and with the linear refractive index mismatch between the media given by Δn. Suppose that this object is positioned along the optical axis of a confocal microscope, a distance z from the focal plane of an incoming Gaussian beam. The electric field at position z of the Gaussian beam is then given by Equation 4.1[65]

$$E_{r=0}(z,t) \propto e^{[ikz - i\phi(k,z)]} e^{i\omega t} \tag{4.1}$$

where k is the wavenumber of the incoming wave and is thus $k = k_p$ for the pump and $k = k_S$ for the Stokes. $\phi(k,z)$ is the Gouy phase shift of the Gaussian beam at position z relative to the beam waist w_0, given by

$$\phi(k,z) = -\arctan\left(z\frac{2}{kw_0^2}\right) \tag{4.2}$$

where the parameter $z_0 = kw_0^2/2$, is the Rayleigh length of the Gaussian beam. The generated anti-Stokes photon is then given by the product of pump squared and Stokes fields as seen in Equation 2.5, which may be written in terms of the Gaussian beams as

$$P_R(z,t) \propto e^{[i(k_{aS})z - i(2\phi(z)_p - \phi(k,z)_S)]} e^{i\omega_{aS}t} \tag{4.3}$$

k_{aS} is the wavevector of the anti-Stokes and is related to the phase matching conditions for the CARS process; the term $2\phi(z)_p - \phi(k,z)_S$ describes the overall Gouy phase shift resulting from the propagation of the Gaussian beam. By comparison, the dominant nonresonant background contribution is generated at the highest intensity plane corresponding to $z = 0$, and therefore behaves as if it originated from this plane [28].

$$P_{NR}(t) \propto e^{i(\omega_{aS})t} \tag{4.4}$$

Equations 4.3 and 4.4 can be expressed more explicitly to $\chi_R^{(3)}$ and $\chi_{NRB}^{(3)}$ through Equation 2.6, including the additional phase terms:

$$P_R(z,t) = \chi_R^{(3)}(\omega) E_{0R} e^{i(\omega_{aS}t + \phi_0 - \delta\phi_G + \delta\phi_L)} \tag{4.5a}$$

$$P_{NR}(t) = \chi_{NR}^{(3)} E_{0NR} e^{i(\omega_{aS}t + \phi_0)} \tag{4.5b}$$

$$\delta\phi_G = 2\phi(z)_p - \phi(k,z)_S \tag{4.5c}$$

$$\delta\phi_L = Dk_{aS}\Delta n \tag{4.5d}$$

where E_{0R} is the electric field strength of the resonant component, E_{0NR} is the electric field strength of the nonresonant component, $\delta\phi_G$ is the phase shift due to the Gouy phase. $\delta\phi_L$ is the phase shift due to the linear refractive index mismatch between the resonant sample and the nonresonant solvent, neglecting dispersion, ϕ_0 is an arbitrary phase. As noted in Chapter 2, the CARS process is created by the interference between the resonant and nonresonant components, described by Equation 2.12. This may be rewritten more explicitly as shown in Equation 4.6

$$I_{CARS}(\omega) \propto |E_{CARS}(\omega)|^2 \propto |\chi_R^{(3)}|^2 + |\chi_{NR}^{(3)}|^2 + 2(\chi_{NR}^{(3)})\Re(\chi_R^{(3)}(\omega)e^{\delta\phi_L - i\delta\phi_G}) \tag{4.6}$$

If the Gouy phase or the refractive index mismatch terms are not taken into account, the cross-term depends only on the shape of the resonant peak. This assumption underlies such retrieval methods as the Kramers-Kronig algorithm discussed in Chapter 2.2 and the Maximum Entropy Method [33, 32]. However, in proper accounting for these terms, it is apparent that there is an additional phase shift that is applied to the resonant component that causes an added rotation it the complex plane. The implications of this phenomenon will be responsible for intrinsic distortions in both CARS images and their spectra.

4.3 Method and Materials

Experimental Design

In order to demonstrate the relationship between spectral distortions and spatial distortions, experiments were run on a model system of nitrobenzene (NBZ) droplets in agarose gel. The Raman spectrum of NBZ was taken using a Renishaw InVia Raman spectrometer, and is shown in Figure 4.1. In order to illustrate the effects of the interference between the resonant signal and nonresonant background, the resonance near 1585 cm^{-1}, identified as the C=C stretch mode [66], was selected for study. This resonance also has the advantage of relative isolation in the fingerprint region, minimizing any potential overlap effects between neighbouring resonances (the weaker resonance at 1520 cm^{-1} is below the current detection limit of the system). NBZ is a relatively volatile liquid at room temperature, so it was necessary to trap it in aragose gel in order to create droplets smaller than the Rayleigh range of the microscope. This was done by

combining the NBZ with a mixture of 1% agarose in water in a 1:25 ratio at 80^{o}C while stirring vigorously. As the agarose cooled, it formed a gel containing a distribution of immobilized NBZ droplets of sizes ranging from $\sim$1 μm to $\sim$20 μm as observed through the transmitted light of our microscope. Conveniently, the agarose does not have any resonances in this region, and therefore contributed only to the nonresonant background response.

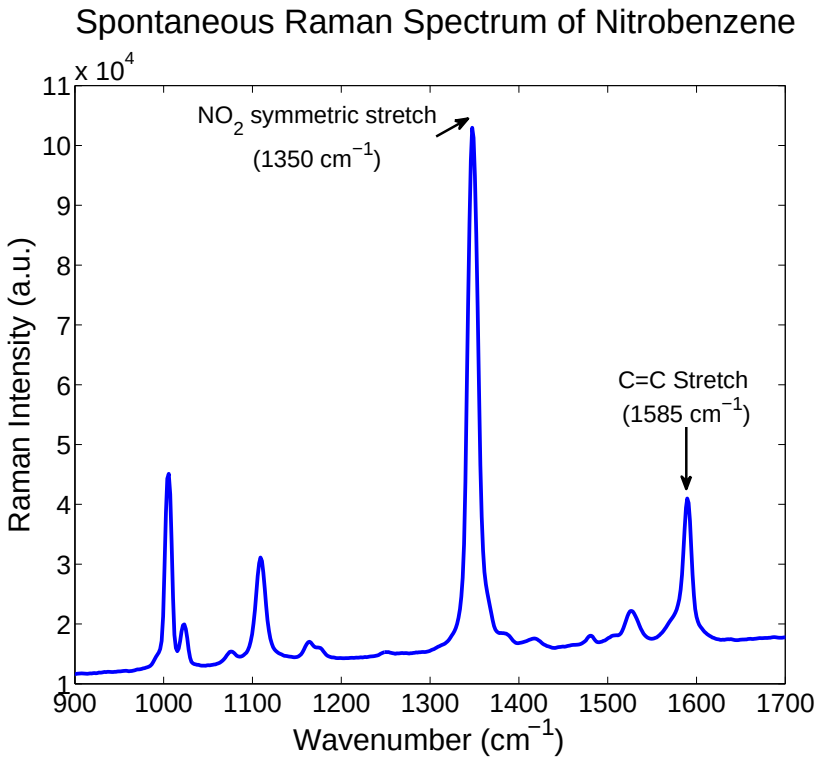

Figure 4.1: Spontaneous Raman spectrum of nitrobenzene in the fingerprint region. The strong NO_2 symmetric stretch peak at 1350 cm^{-1} and the weak C=C stretch at 1585 cm^{-1} of interest to this study are highlighted.

The laser system was operated using the fingerprint setup, described in Chapter 3.2, tuned to 900 nm. The output power from the laser was $\sim$500

mW with a bandwidth of ∼15 nm. Powers of 150 mW and 20 mW were measured for the pump and Stokes, respectively, at the microscope entrance. A typical CARS image of the droplets in gel is shown in Figure 4.2, in this case using the strong peak at 1350 cm^{-1} for contrast. At the weak NBZ peak of interest, the resonant to nonresonant ratio is ∼2:1.

The field in Figure 4.2 was selected for observation, and a focal plane at $z = 0$ μm identified for the highlighted droplet using the transmitted light. Spectral scans of this field were taken in the fingerprint region from 1235 cm^{-1} to 1785 cm^{-1}, divided among 340 frames, for an effective resolution of ∼1.6 μm per frame and an overall chirped resolution of ∼30 cm^{-1}. The field was scanned from the $z = -2.5$ μm to $z = 2.5$ μm in 0.5 μm intervals. Each of the resulting spectra were smoothed using a rolling five-point average, and the Raman spectra retrieved using the Kramers-Kronig algorithm described in 2.2.

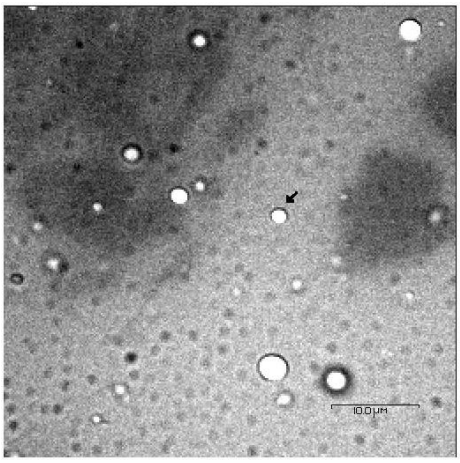

Figure 4.2: CARS image of nitrobenzene at best focus for the highlighted droplet at the 1350 cm^{-1} resonance. Note the presence of the shadows (black) of out of focus objects projected into the image plane.

Numerical Simulations

In order to verify the experimental results, numerical simulations of the system were performed using a finite-difference time-domain (FDTD) method, following the protocols established in the literature [28, 67, 68]. In brief, the simulation domain consists of a tightly focused (NA = 1) Gaussian pump beam with wavelength 900 nm and a Stokes beam of frequency ω incident on a Raman resonant scatterer of diameter 1 μm at frequency 1600 cm^{-1} and linewidth $\Gamma = 10$ cm^{-1}. The simulation domain used the constitutive relations described in Equations 4.7a to describe the resonant and nonresonant components of the signal, where $*$ represents the convolution integral.

$$\vec{D} = \left[1 + 4\pi\left(\chi^{(1)}\vec{r} + \chi^{(3)}\vec{r}E^2\right)\right]\vec{E} + 4\pi\vec{P}_R \tag{4.7a}$$

$$\vec{H} = \vec{B} \tag{4.7b}$$

$$\vec{P}_R(\vec{r},t) = \frac{1}{4\pi}\vec{E}\cdot\left(\chi_R(\vec{r},t)E^2(t)\right) \tag{4.7c}$$

$$\chi_R(\vec{r},t) = \chi_R^{(3)}(\vec{r}) * \mathscr{F}^{-1}\Big(\frac{\omega_R^2}{\omega_R^2 - \omega^2 + 2i\omega\Gamma_R}\Big) \tag{4.7d}$$

Maxwell's equations were solved using a standard Maxwell solver [69]. The anti-Stokes beam was generated at the Raman scatterer and numerically propagated into the far field and absorbed at the simulation boundary, explicitly taking into account the propagation effects of the Gouy phase shift. Outside the simulation domain, the fields were analytically propagated to a detector and the intensity was measured. In one case, the refractive index was chosen to be uniformly $n = 1.33$ for the entire simulation domain, exclusively isolating the effects of the Gouy phase. In another simulation, an index mismatch between NBZ and the agarose gel ($\Delta n = 0.214$) was explicitly included.

4.4 Results

The experimentally measured CARS spectra of the droplet highlighted in Figure 4.2, at three different focal positions, are shown in Figure 4.3(a). The best focus position is defined to be $z = 0$ μm, shown in green circles in the graph. The spectra at $z = \pm 1$ μm are shown in blue squares and red crosses, respectively. All three spectra display the typical dispersive line shape characteristic of CARS spectra as described in Chapter 2.1. The spectra at $z = \pm 1$ μm have some significant differences compared to the spectrum at $z = 0$ μm, most notably in terms of the amplitudes of the strength of the peak and dip in the spectrum. Moreover, there is some asymmetry between the two spectra as well; the $z = -1$ μm spectrum has notably lower amplitude, especially at the dip in the spectrum near 1620 cm^{-1}. It should be noted that, because both of these signals are symmetric within the Rayleigh range of the microscope, one would naively expect them to have equal magnitudes: this is not the case. These differences are exacerbated significantly upon retrieval, as shown in Figure 4.3(b): There is a significant and persistent shift in the position of the spectral peak as the droplet is scanned from $z = -1\mu$m to $z = +1$ μm. In particular, while the $z = 0$ μm spectrum is found to have an identical peak position to that of spontaneous Raman (albeit broaded due to the lower spectral resolution of our system), the spectral position of the peak shifts by $\sim$10 cm^{-1} upon scanning from $z = -1$ to $z = +1$. This is a clear demonstration of spatial-spectral coupling: Both the CARS spectra and the retrieved Raman spectra are intrinsically coupled to the spatial position of the droplet (and the surrounding NRB) within the laser focus.

The corresponding CARS spectra from the numerical simulations are shown in Figure 4.4(a), revealing qualitative agreement with those of Figure 4.3(a). In particular, the spectra at $z = \pm 1$ μm (dashed, dotted) are distorted both in

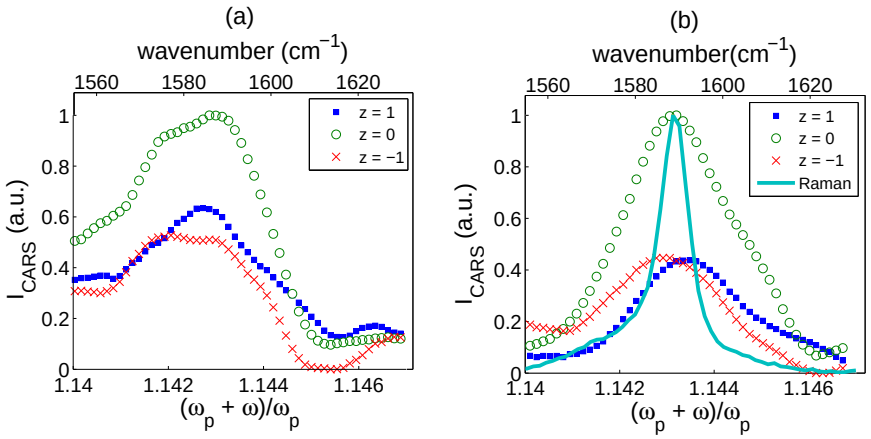

Figure 4.3: (a) Experimentally measured raw CARS spectra of the highlighted NB droplet of Figure 4.2, located at the $z = 0$ μm (circles) and at displaced foci ($z = -1$, crosses, and $z = +1$ μm, squares). (b) The retrieved Raman spectra of the same droplet, overlaid with the spontaneous Raman spectrum of NBZ (solid line). There is a spectral shift of 10 cm^{-1} due to the intrinsic spatial-spectral coupling.

amplitude and in form relative to that at the best focus $z = 0$ μm position (solid line), and are different from each other despite their symmetric displacement about the best focus, and, therefore, identical laser intensities. The spectrum at $z = 1$ μm in the simulations does have a considerably higher amplitude than the experiments; this is likely due to some imprecision in being able to determine the exact position of the best focus in the experimental measurements, or due to refractive index mismatch. These spectra are then retrieved using the standard Kramers-Kronig algorithm (which is insensitive to phase shifts due to the Gouy phase or refractive index mismatch) and as shown in Figure 4.4(b). These display an identical 10 cm^{-1} spectral shift as seen in the experimental measurements.

In this model system, it is possible to retrieve the correct Raman spectra using a simulated annealing least squares method [70] by assuming an isolated Lorentzian profile given by Equation 2.11. In this simple model, additional

phase shifts $\delta\phi$ were treated as a free parameter and, by including this within the solution space, the correct spectra could be recovered as shown in Figure 4.4(c). We note, however, that this method requires foreknowledge of the shape of the Raman spectrum, and thus cannot be applied more generally. Finally, in Figure 4.4(d), the effect of the difference in refractive index between nitrobenzene ($n = 1.554$) and agarose ($n = 1.33$) was explored and it was found that the mismatch introduced a further spectral shift beyond the effect attributed to the Gouy phase shift.

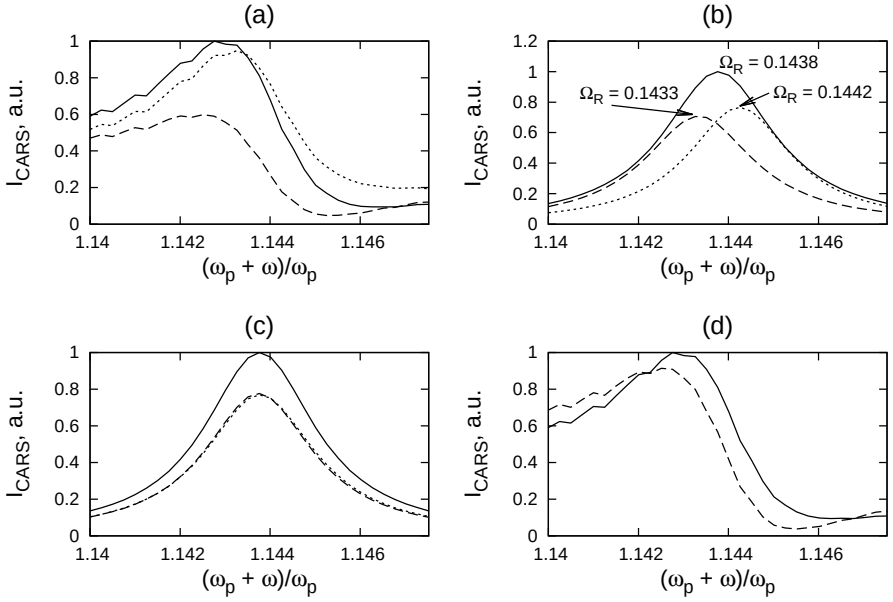

Figure 4.4: (a) Numerically generated CARS spectra of nitrobenzene droplets, located at the $z = 0$ μm position and displaced along z, centered at $\Omega_R = 1600$ cm^{-1}. (b) The Raman spectra of NB droplets retrieved using the Kramers-Kronig algorithm that does not consider the Gouy phase. The shift in Ω_R is 10 cm^{-1} ($9 \times 10^{-4} \omega_P$). (c) The retrieved Raman spectra of the same data, but now including the effects of the Gouy phase. (d) The CARS spectra of nitrobenzene accounting for the refractive index mismatch between nitrobenzene and the agarose medium. In panels (a)-(c), the solid line is $z = 0$ μm, $z = -1\,\mu$m is the dashed line, and $z = +1\,\mu$m, dotted line); in panel (d), the dashed line represents the index-mismatched CARS spectrum at $z = 0$ μm.

4.5 Discussion

The experimental measurements illustrate the intrinsic coupling between distortions in the image and corresponding distortions in the spectra. In Figure 4.2, the image is cratered with numerous shadows representing the distortions of out-of-focus droplets; indeed, only a few droplets are within the focal plane at any given time. As the focus shifts in z, different droplets will move into the focus and others will produce shadows. Because the nonresonant background is predominantly generated at the best focus, while the resonant signal is generated at the object, there will be a phase difference between the two signals, particularly due to the Gouy phase [28]. Depending on the relative position of the object within the focal volume, this will produce either constructive or destructive interference, resulting in signal enhancement away from the best focus, or shadows, respectively. The phase shift at a given z can be calculated directly from Equations 4.5(c) and (d). For the microscope system, the Rayleigh lengths for pump and Stokes are on the order of 1.4 μm and 1.6 μm, respectively, assuming identical spot sizes. The linear refractive index mismatch between nitrobenzene and agarose is 0.214, and the size of the droplet is taken to be 1 μm. Figure 4.5 illustrates the total phase shift relative to z. It is evident that the dominant effect is the Gouy phase (blue sold line); the introduction of the refractive index mismatch retains essentially the same functional form, and simply results in a shift toward more negative phase. Within the Rayleigh range of the pump and Stokes, the phase shifts from $\sim -\pi/4$ to $\sim \pi/4$.

The CARS spectra in Figures 4.3(a) and 4.4(a) demonstrate that this phase difference manifests itself as distortions in the spectral regime: Both the intensity and shape of the spectra are significantly distorted relative to the best focus. Retrieval of these distortions using standard methods, as shown in Figures 4.3(b) and 4.4(b), fails to retrieve the correct spectra. Both the experiments

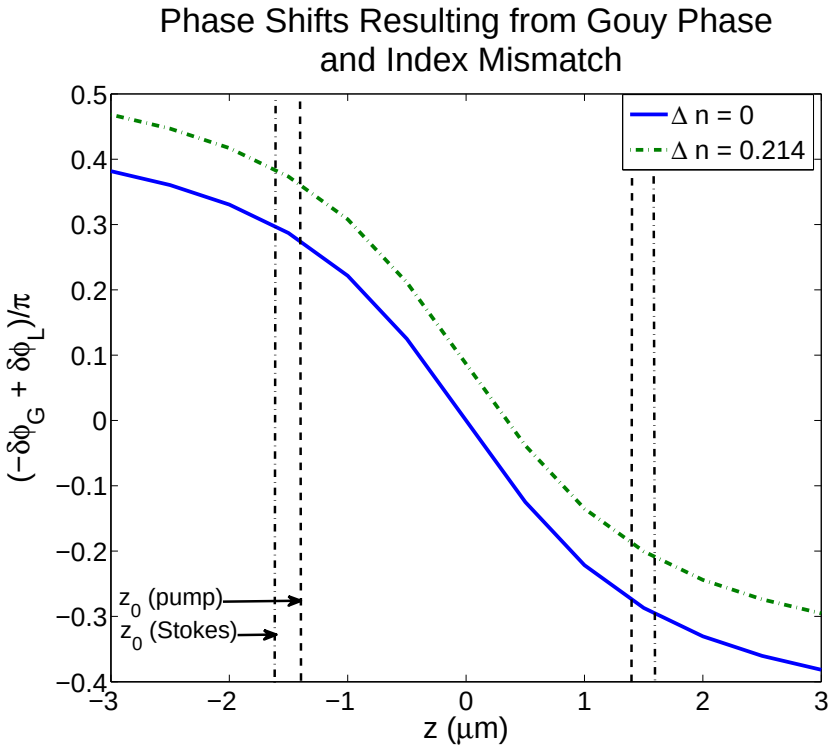

Figure 4.5: Estimated phase shifts in the CARS microscope system due to Gouy phase alone (green solid line) and Gouy phase with linear refractive index mismatch of $\Delta n = 0.214$ (blue dotted line).

and simulations display a 10 cm^{-1} shift in the spectrum as the NBZ droplet is moved through the focus. By design, this shift cannot be associated with any internal chemical or thermodynamic effects within the sample; the NBZ droplet is a pure, homogenous compound. As discussed in Chapter 4.1, shifts of similar magnitudes are often associated with physiological changes in biological systems, both in CARS microscopy and in Raman microscopy. The evidence presented above suggests that, in the case of CARS, such associations may be unwarranted if proper care is not taken to account for the spectral shifts due to

propagation effects such as the Gouy phase.

A simple, analytic model can be used to provide additional insight. A model CARS spectrum can be created by substituting Equation 2.11 into Equation 4.6 combined with the phases derived from Figure 4.5, including the refractive index mismatch. The resulting CARS spectra are shown in Figure 4.6(a). There is a family of spectra of completely different forms, all of which correspond to the same identical object under observation. It is clear that there is significant difficulty in extracting any useful information about this object from the CARS spectrum alone. Upon retrieval, the effect persists, as seen in Figure 4.6(b): The distortions overall are suppressed and many of the spectra look very similar to a true Raman profile; however, the distortions in the CARS spectra are instead mapped to spectral shifts in the retrieved Raman profile.

The Raman peak positions vary smoothly with z as shown in Figure 4.7. The overall spectral shift from $z = -3$ μm to $z = 3$ μm is of the order the spectral linewidth, as can be seen in Figure 4.7(a), and the effect of the refractive index mismatch is to tend to shift the peak position toward lower wavenumbers, as shown in Figure 4.7(b). It can be concluded, therefore, that shifts in the peak that are greater than the spectral linewidth can be safely associated with real spectral features; peak shifts that are within the spectral linewidth may be subject to spatial-spectral coupling that creates uncertainty in the peak position.

The observed coupling is due to the position of a small object within the Rayleigh range of the laser focus. For objects of size $D \gg z_0$, that is, objects much larger than the Rayleigh range, the spectral shifts will not be observed at all due to spatial averaging across the whole of the Rayleigh range, although coupling will still be observed near the interfaces between resonant and non-resonant media [71]. Moreover, as the coupling term between the resonant and nonresonant background terms is linear in $\chi_R^{(3)}$, if $\chi_R^{(3)} \gg \chi_{NR}^{(3)}$, the quadratic

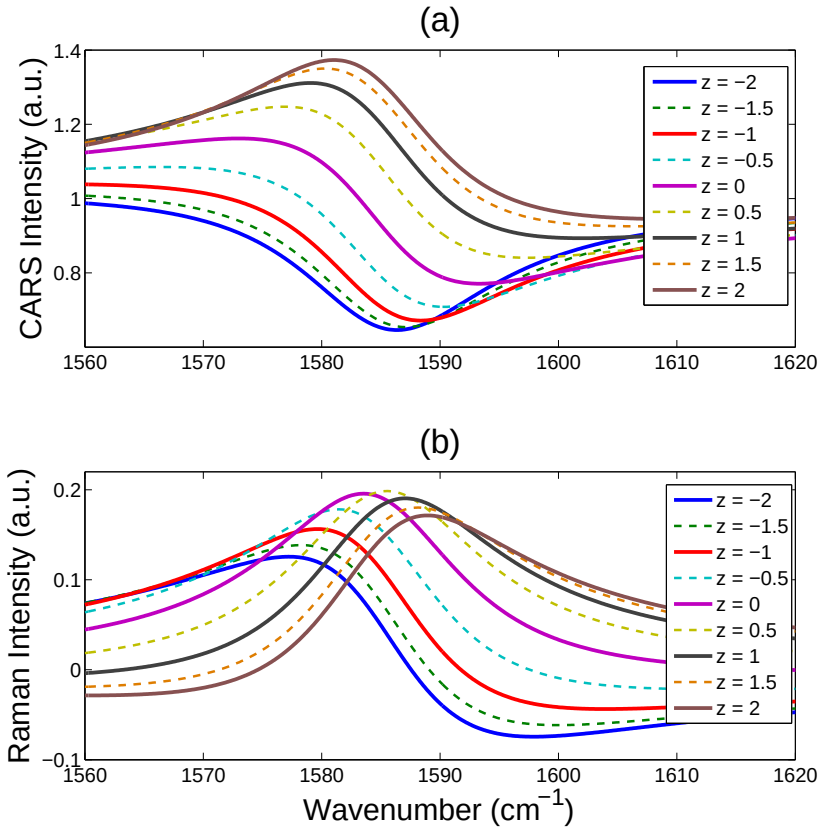

Figure 4.6: (a) Generated CARS spectra the effects of Gouy phase and linear index mismatch at various positions z. (b) Raman-retrieved spectra of (a)

term in Equation 4.6 will dominate, and the CARS spectrum will converge to the Raman spectrum independent of the coupling term.

4.6 Conclusions

It is clear from the discussion above that knowledge of spatial-spectral coupling is required to interpret CARS images and spectra. The interference between the resonant response and the nonresonant background manifests itself as shadows in images and distortions in spectra, particularly of weakly-resonant,

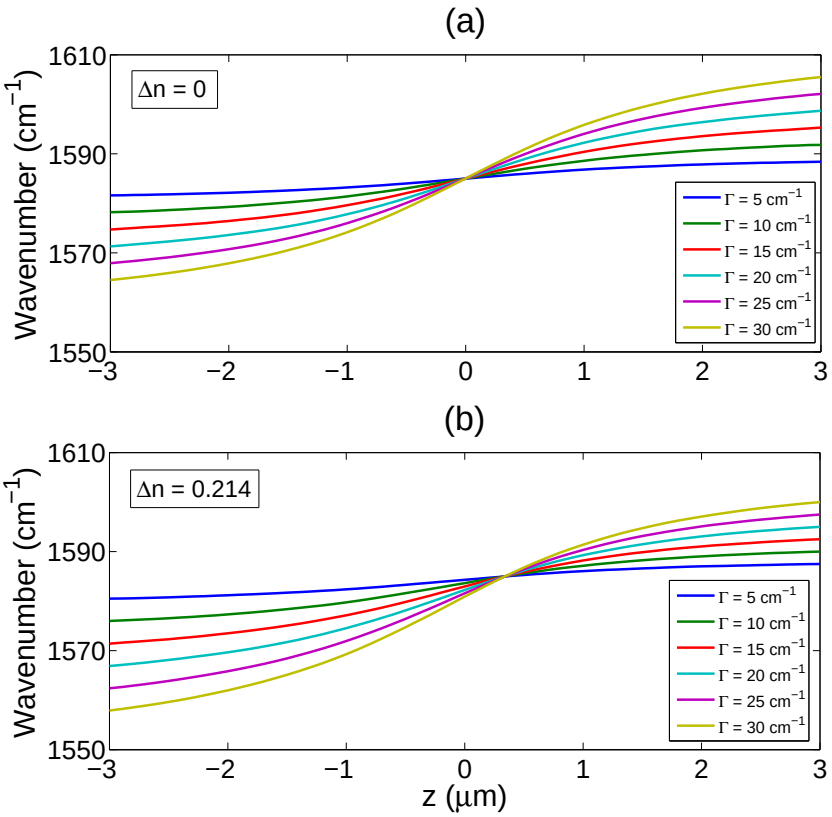

Figure 4.7: The shift in the Raman peak with z at various spectral linewidths (a) neglecting refractive index mismatch and (b) accounting for refractive index mismatch. The total possible shift is equal to the spectral linewidth.

sub-Rayleigh length objects. The resulting spectral distortions persist into the retrieved Raman spectrum using standard methods, yielding spectral shifts of order the spectral linewidth. Therefore, great care must be taken in assigning physical significance to observed spectral shifts of this nature in physiological systems, as the shifts may be due to propagation effects.

If a model can be devised which can take the shifts into account, such as the one shown in Figure 4.4(c), it may be possible that the correct spectral positions can be retrieved. Regrettably, the model shown in Figure 4.4(c) is

not a general one; it requires specific knowledge of the system, such as the correct spectral linewidth, that the peak is isolated, etc. in order to retrieve the undistorted spectra. A more general solution is a challenging problem that warrants further study. In particular, the refractive index term δ_L may be very difficult to measure accurately in complex heterogenous systems, which may render this problem intractable.

5 The Remarkable Algae *Haematococcus Pluvialis*

5.1 Introduction

In the preceding Chapters, we discussed how the CARS spectrum can be shaped by the interplay between the sample, the instrument, and the medium, and how this interplay can lead to distortions in the CARS spectrum. In the following Chapters, we turn our attention to how certain kinds of molecular systems can be advantageously exploited by CARS to produce significant signal enhancements, resulting in dramatically improved contrast and sensitivity. In particular, we focus our attention on the ketocarotenoid compound astaxanthin, which is produced by the microalgae *haematococcus pluvialis*.

Haematococcus pluvialis are a species of unicellular freshwater microalgae found ubiquitously in freshwater ponds and rainwater pools worldwide. The family name *Haematococcaceae* derives from the blood-red pigmentation in species of this group, which can often be observed on the surface of small pools or bare rocks near the algae habitats [72]. This pigmentation arises due to high concentrations of the carotenoid compound astaxanthin, which is synthesized naturally by these algae [73]. *Haematococcus pluvialis* have attracted considerable interest from researchers in recent years, as carotenoids have emerged as high-value compounds with applications in cosmetics, nutriceuticals, and food additives, with a worldwide market for astaxanthin exceeding a hundred million dollars [74, 75, 76, 77]. While scientific-grade astaxanthin is typically made synthetically, *haematococcus pluvialis* represents the primary source of industrial astaxanthin production due to the high yields of the algae that can approach 3% of dry weight [78, 79]. Moreover, during the astaxanthin production phase, internal lipid concentrations rise from 16% to over 30%, allowing for sequestra-

tion of significant amounts of carbon and establishing its potential as a biofuel [80].

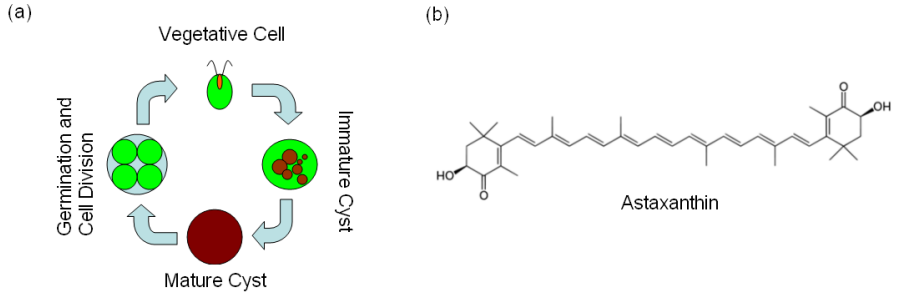

Figure 5.1: (a) The life cycle of *haematococcus pluvialis*. The algae start in a flagellated, vegetative phase (top). Under adverse conditions, they begin encystment (right), until they reach full maturation (bottom). This part of the cycle can persist nearly indefinitely, but eventually, the cell will germinate and undergo cell division (left), ultimately recovering the vegetative cells. (b) The chemical structure of astaxanthin, bioproduced during the encystment phase.

The algal life-cycle consists of four distinct phases, as shown in Figure 5.1(a) [73, 81]. In the vegetative phase, *haematococcus pluvialis* is a small, flagellated algae whose dominant pigmentation arises from chlorophyll. Algae in this phase are essentially devoid of astaxanthin and are consequently green in colour. Upon exposure to unfavourable conditions such as nitrogen deprivation [73], salt stress [82], or intense illumination [83], the flagellated algae enters an encystment phase. During this phase, the algae begins astaxanthin production within lipid droplets at its centre, at the expense of the exterior chlorophyll [84]. This process causes the algae to swell considerably, such that the fully encysted algae can reach several times their original size, with its constituents fully dominated by astaxanthin, giving the cells their characteristic red hue. The encysted algae can persist for extended periods of time with minimal nutrients or light exposure. When conditions improve, the carotenoids are decomposed back into chlorophyll, and the algae undergo cell division. Commercially, it is clear that

the encystment phases are of primary interest, and the process of understanding and optimizing carotenogenesis is a topic of active study [79, 85].

Astaxanthin is classified in the xanthophyll family of carotenoid compounds. Xanthophylls are characterized by a chain of polyconjugated carbon-carbon bonds functionalized with a hydroxyl or ketone group. The molecular structure of astaxanthin is shown in Figure 5.1(b). Carotenoids serve several important functions in cellular biology [86, 87]. First, carotenoids typically have a strong visible-light absorption band. Light harvested from this band can be efficiently passed to chlorophyll, effectively extending the photosynthetic absorption of the plant. Second, these compounds serve as a protective mechanism in plant physiology. In the absence of carotenoids, under absorption of light, chlorophyll may enter into a relatively long-lived triplet state that, in turn, reacts with molecular oxygen to produce singlet oxygen, an oxidizing agent that is toxic to the plant. In the presence of carotenoids, this triplet state of chlorophyll is greatly suppressed, preventing this hostile reaction. In addition, the carotenoids react readily with singlet oxygen and other harmful radicals, protecting the vulnerable cellular components [88]. Xanthophylls, including astaxanthin, play an additional role in protecting the cell by forming a protective shell within lipid drops surrounding the cell nucleus. Thus, these "secondary carotenoids" are not only employed to protect the chlorophyll, but also to provide a protective shade around the nuclear components, absorbing excess light and protecting the genetic material from radicals produced via photobleaching of chlorophyll [89].

Raman microscopy has proved to be a natural choice for study of carotenoids *in vivo*, including astaxanthin in *haematococcus pluvialis* [84, 90, 91, 92]. The polyconjugated structure of these compounds is known to produce an unusually large Raman cross section and distinctive Raman spectrum consisting only of a few well-defined peaks (in the fingerprint region) [93]. However, while

carotenoids are only weakly fluorescent, greatly increasing the signal-to-noise in Raman studies *in vitro* [94], plant cells also contain compounds such as chlorophyll that fluoresce strongly when exposed to visible light, making resonance Raman microscopy considerably more challenging. While Raman spectroscopy of carotenoids has been a subject of extensive study, carotenoids have received comparatively little interest in the CARS literature [95, 96, 97, 98], perhaps due to the relative difficulty in implementing a fingerprint CARS scheme, or the general reputation of CARS as being primarily suited to lipids.

Nonetheless, CARS microspectroscopy provides several key advantages over spontaneous Raman for the study of astaxanthin in *haematococcus pluvialis*. The confocal excitation scheme employed by our CARS microscope generally prevents light significantly outside the focal volume from entering the detector; because astaxanthin is lipid-associated and the dominant fluorophore is chlorophyll: they are spatially separated in the algae, so that only the weak fluorescent response from the carotenoid will be observed within the focal volume. This, in turn, is easily filtered by a long-pass filter, since the fluorescent spectrum peaks at $\sim$ 680 nm and the anti-Stokes in the fingerprint region is produced at 800 nm. Not only do we avoid any fluorescent contamination in the Raman spectrum, but we can also simultaneously image the chlorophyll using its strong TPEF response. Thus we can directly separate the two primary constituents of *haematococcus pluvialis* by associating fluorescence with chlorophyll, and CARS with astaxanthin. As we will show, the measured CARS response of the carotenoids in the fingerprint region appears nearly devoid of any nonresonant background contamination and is significantly stronger than those of common calibration standards such as diamond, nitrobenzene, or pure oils. This allows for direct quantitative measurements of carotenoids *in vivo*, free of any confounding effects due to the nonresonant background, such as those

discussed in Chapter 2.1 or the spatial-spectral coupling effects in Chapter 4. In this Chapter, we discuss several significant experiments demonstrating the effectiveness of CARS for *in vivo* carotenoid research.

5.2 Method and Materials

Introduction

Our studies of *haematococcus pluvialis* in CARS operated using the standard fingerprint microscope scheme, detailed in Chapter 3.2. Here, we briefly outline a series of variations and techniques related to the studies of carotenoids that were further undertaken.

Preparation of the Algae

Cultures of *haematococcus pluvialis* algae were provided by the National Research Council of Canada, Algal Carbon Conversion Flagship Program. Two main cultures were used in the experiments. The first culture was was grown in Bold's basal media with excess nitrate supplementation at 22^oC under 150μmol photons m^{-2} s^{-1} photosynthetically active radiation and agitated on a shaking table at 175 rpm. The highly nitrogenated environment encourages algal growth and generally does not lead to encystment [73]. This culture appeared visually to be green, and both motile algae and palmelloid algae undergoing cell division could be observed. A few algae did appear to have traces of red-brown colouring indicating astaxanthin. This culture was kept in a well lit area open to the air, and was shaken every few days.

In addition to the process above, the second culture was further irradiated at 800 μmol photons $m^{-2}s^{-1}$ photosynthetically active radiation for a few days and the nutrient supply was allowed to deplete. In this nutrient-poor environment under high light conditions, the algae developed significant quantities of astax-

anthin. The cultures were observed to be red-brown by eye, and no motile algae were observed at any point in this culture. The majority of the cells appeared to be in various stages of encystment. Encysted cells could be maintained under low light conditions for a period exceeding two years, with minimal observable degradation in the cellular contents as observed by through transmitted light or the corresponding CARS and TPEF signals.

For microscopy experiments, the algae in water were placed on a microscope slide or well slide. No other preparation for the cells was necessary; in the former case, additional water was added periodically to prevent the cells from drying.

Preparation of AstaREAL

A sample of 10 g AstaREAL-10L (a commercially available extract of esterified astaxanthin from *haematococcus pluvialis*, nominally 10% astaxanthin by weight) was acquired from AstaReal (a company of Fuji Chemical Industry Group, Japan). This was used as a reference sample as it contains concentrated esterified astaxanthin in the same form and similar environment to that in live *haematococcus pluvialis* cells. This compound resembled an opaque, viscous tar, containing large sections of lower density material interspersed with microscopic droplets of very high concentration astaxanthin. This compound dissolved readily in both canola oil and acetone at ambient conditions with shaking. This produced an orange-red liquid with no observable droplets or astaxanthin deposits. Due to the volatility of acetone, it was more convenient to create samples of diluted AstaREAL using canola oil, and this dilution was used for all experiments involving AstaREAL unless otherwise noted. A concentration series of 8 samples of AstaREAL in canola were made, with each sample having 2/3 the concentration of the previous member of the series (approx. half of the CARS intensity). These were labelled C_0 through C_7. A second dilution series at lower concentrations C'_1 through C'_7 at 1/2 dilutions was also created.

The concentrations of AstaREAL in solution were measured by collecting the UV-Vis spectrum using a CARY5000 spectrometer. This was done at a 50:1 dilution relative to the initial C series using a sample of pure canola as a reference and divided by the source spectrum. It was also instructive to collect the UV-Vis spectrum through the microscope directly. To do this, the light from an intense incandescent lamp was directed into the microscope using an external mirror, and absorption spectrum of an AstaREAL dilution on a microscope slide was collected through the condensor into an Ocean Optics spectrometer, using pure canola oil as a reference.

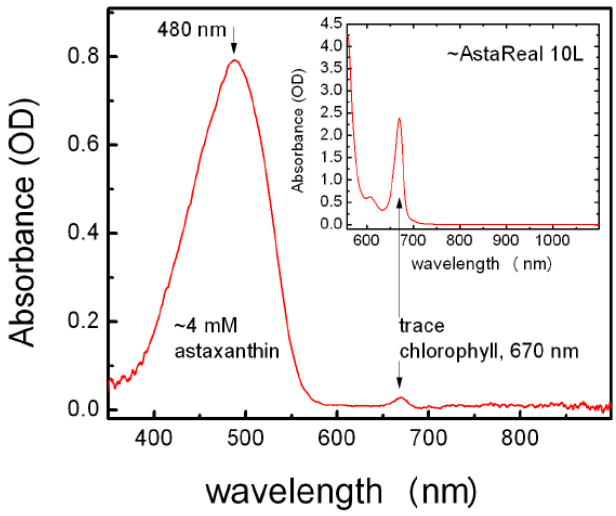

Figure 5.2: UV-Vis absorption spectrum of AstaREAL-10L collected through using the CARY5000 spectrometer The main peak corresponds to the absorption of astaxanthin, and the smaller peak (see inset) corresponds to a trace amount of chlorophyll.

The absorption spectrum of C_5 collected through the CARY5000 spectrometer is shown in Figure 5.2. The spectrum consists of a very large peak centred at 480 nm, with a smaller peak at 670 nm. The former peak is the primary absorption of astaxanthin, as identified in the literature [99]; the latter peak is

identified to be trace contamination of chlorophyll in the AstaREAL-10L. This is to be expected as the AstaREAL product is made directly from ground *haematococcus pluvialis*. Due to the fact that AstaReal-10L is not a pure compound, it was necessary to estimate the concentration of astaxanthin in the solutions. The concentration was then estimated according to the following formula:

$$C = \frac{OD}{d\alpha} \tag{5.1}$$

where OD is the measured optical density, d is the thickness of the well slide, and α is the absorption coefficient of astaxanthin in canola. The thickness of the well slide was 300 μm. The absorption coefficient of astaxanthin in canola was not found in the literature, but it was found for several similar solvents to be in the range of 100000-130000 $cm^{-1}M^{-1}$ [100]. A value of 115000 $cm^{-1}M^{-1}$ was adopted. The calculated concentrations were as large as 45 mM for C_0 and 2 mM for C_7, with estimated errors of order 20%, with the primary source of error being due to the absorption coefficient of canoloa. In the second series, the concentrations ranged from 7 mM to 0.08 mM with the same relative error.

In the fingerprint region, the 1334 cm^{-1} peak of diamond was used as an intensity calibration to astaxanthin. Because the CARS signal from astaxanthin is so much larger than diamond, the PMT and laser intensity were chosen so that the astaxanthin signal nearly saturated in order to maximize the dynamic range. The diamond sample was sufficiently large that diamond could completely fill the microscope focus. The polarization of the light into the microscope was adjusted to maximize the signal intensity in order to ensure a consistent orientation of the diamond was used. The Stokes spectrum from the fibre was also measured after every few scans to ensure that the variations described in Chapter 3.4 were properly accounted for. Under these conditions, a direct comparison between the signal intensites of CARS in AstaREAL or *haematococcus pluvialis* could

be ascertained, even if small changes to the fundamental laser wavelength were introduced.

Collection of Spontaneous Raman

The spontaneous Raman spectrum of several AstaREAL samples and *haematococcus pluvialis* algae were collected using a Renishaw InVia Raman microscope made available by the Nanocomposites group at the National Research Council of Canada. The Raman system has three available lasers at 514 nm, 633nm, and 785 nm with total powers of 3.8 mW, 5.1 mW, and 81.3 mW, respectively. For the 514 nm laser, a 1800/mm grating was used, while for the longer wavelengths, the 1200/mm grating was employed. Samples were measured in well slides using a 5× objective lens. Measurements were typically done at 10s exposure times using 0.05%–1% of the available laser power depending on wavelength and concentration in order to minimize photobleaching and fluorescence, and maximize the Raman intensity. Only dilute ($<$ 10mM) samples could be used for this purpose as at higher concentrations the samples are nearly opaque to the system. The spontaneous Raman spectrum could be collected in the region from 600 cm^{-1} to 3000 cm^{-1} in a few minutes' time.

Direct comparison of the absolute intensities of Raman lines is challenging, as one must take into account the collection geometry and detector sensitivity as a function of frequency, refractive index changes, and absorption and reabsorption cross-sections of the solute [101]. To a very crude approximation, the relative strength of two Raman lines R scales as

$$R \propto \left(\frac{I_1}{I_2}\right)\left(\frac{\lambda_2}{\lambda_1}\right)^4\left(\frac{P_1}{P_2}\right)\left(\frac{\zeta(\lambda_1)}{\zeta(\lambda_2)}\right) \tag{5.2}$$

where I_1 and I_2 are the measured intensities of the Raman lines, λ_1 and λ_2 are the excitation laser wavelengths and P_1 and P_2 are the excitation laser

powers, respectively. The function $\zeta(\lambda)$ represents the detector sensitivity at the wavelength of interest.

Preparation of Astaxanthin Radicals

Radicals of astaxanthin were produced for direct comparison to neutral astaxanthin in the microscope. Astaxanthin radicals form readily in the presence of $FeCl_3$ [102]. For this experiment, acetone was used as a solvent as $FeCl_3$ precipitates in canola oil. A stock solution of AstaREAL in acetone was produced. A 1 mg of powdered $FeCl_3$ was added to a portion of this solution to produce radicals, which were compared with a reference of equal concentration made from the stock.

5.3 CARS Microscopy of *Haematococcus pluvialis*

Preliminary measurements of the cyst-dominated *haematococcus pluvialis* were taken using the fingerprint setup operating at 918 nm pump at our standard operating powers of 100 mW pump and 17 mW Stokes. A wide-field image of *haematococcus pluvialis* at these powers is shown in Figure 5.3(a). The system allows for clear differentiation between the astaxanthin generated by the CARS signal (red) and the TPEF generated by chlorophyll (green). The accompanying spectrum in Figure 5.3(b) shows clear peaks at 1000 cm^{-1}, 1148 cm^{-1}, 1268 cm^{-1}, and 1520 cm^{-1}, consistent with values of 1007 cm^{-1}, 1152 cm^{-1}, 1275 cm^{-1}, and 1520 cm^{-1} as found in the literature [92]. In particular, we associate the 1000 cm^{-1} peak with C-CH_3 stretching, the 1148 cm^{-1} peak with C-C stretch, and the 1520 cm^{-1} peak with C=C vibrations characteristic of carotenoids [103]. At these powers, however, an appreciable photobleaching effect was measured, both in the CARS and the fluorescent responses. This is shown in Figure 5.3(c), where we see that there is a substantial difference in

the CARS spectrum simply as a result of the direction travel of the translation stage–that is, over the course of a scan, the photobleaching of the CARS response is sufficiently large at this power to distort the relative heights of the peaks. The signal intensity was found to decrease at an extremely rapid rate, likely too rapid for our pixel dwell time to be able to appreciably measure, as shown in Figure 5.3(d), then decay at a relatively linear rate at longer times. It was further observed that the brown-red colour of the astaxanthin was significantly diminished in the transmitted light image as shown in the before-and-after images in the transmitted light in Figures 5.3(e) and (f), respectively.

When the power was reduced to <20 mW pump and <20 mW Stokes, no photobleaching was observed over the timescales of our measurements, except at high magnifications ($> 5\times$), where even lower (<10 mW) pump powers were required to minimize photobleaching. Surprisingly, the substantial decrease in pump power did not require a corresponding increase in PMT voltage. This is consistent with previous observations in Raman microscopy of β-carotene, where a strong saturation effect depending on laser power was observed [104]. In Figure 5.4, we show a series of images of *haematococcus pluvialis* cysts using CARS (red) and TPEF (green). The high-resolution (512×512 pixel with 0.5 μm transverse resolution at $5\times$ zoom) images enable us to see the distribution of astaxanthin within the cell for various cellular morphologies. It can be seen that the TPEF and CARS signals are strongly anti-correlated, representing distinct spatial regions within the cell. The CARS signal, which maps the astaxanthin content, is confined to small, well defined regions–presumably lipid drops–near the interior of the cell. These are surrounded by chloroplasts which are simultaneously visualized by TPEF. This spatial localization is consistent with the model that the astaxanthin forms a protective layer around the nucleus [105]. A few cells exhibited significant reduction of chlorophyll signals,

and, for these, the entire cell was dominated by large astaxanthin deposits, consistent with the hypothesis that astaxanthin biosynthesis ultimately comes at the expense of chlorophyll[85]. Several of the cells contain large, circular, transparent voids within them. These voids do not have any CARS or fluorescent signals, and are transparant under visible light imaging. In Figure 5.5, we show a three-dimensional reconstruction of a cell made from images taken in 1-μm z-steps, showing the spatial distribution of cellular contents throughout the whole volume. Again, a near-complete segregation of the chlorophyll and AXN is observed, with a dense deposit of AXN dominating the interior of the cell, enclosed by a thin exterior layer of chlorophyll.

In Figure 5.6 we see the spectrum of an astaxanthin droplet of an astaxanthin droplet of a particular algal cell taken at 915 nm pump and 15 mW power (red). Overlaid with this is the spontaneous Raman spectrum of the calibrated AstaREAL standard, normalized to the peak intensity of the 1520 cm^{-1} peak (grey). The spontaneous Raman spectrum was collected from the Raman microscope, and then convolved with a 30 cm^{-1} Gaussian to simulate the spectral resolution of our system (black). As can be observed from the figure, there is good agreement of the positions of the peaks, and relatively good agreement about the intensities of the major peaks in the 30 cm^{-1} resolution Raman spectrum. The differences between the spectra are likely due to variations in the Stokes power. Notably, the peak positions of the Raman and CARS spectra agree without the need for any of the retrieval algorithms discussed in Chapter 2.2–the spectrum is essentially pure CARS, with no measurable contamination from the nonresonant background.

We perform a concentration series measurement using the C_0-C_7 series, as shown in Figure 5.7(a). In this series, we see that the concentration of astaxanthin follows a strict quadratic relation down to the lowest measured concentra-

tion of 2 mM. By comparison, the concentration of DMSO relative to d-DMSO shows that, at 3M, we see the transition to the linear concentration regime. The two curves intersect at 0.2M DMSO to 0.002M astaxanthin, indicating that astaxanthin has a 10^4 times larger response per molecule compared to DMSO. This does not, however, take into account the fact that measurements of low concentrations of DMSO require 100 mW of pump power to be observed, compared to $\sim$ 10 mW for astaxanthin. Thus, the astaxanthin signal is in fact six orders of magnitude greater in intensity than that of DMSO. In Figure 5.7(b), we extend this series down to 100 μM. In this region, we do see the emergence of the NRB into the CARS spectrum, as the concentration dependence linearizes around 1 mM. The dominant NRB contribution in this case is due to FWM from the canola oil solvent.

Using this concentration calibration, we are able to transform the CARS image of the algal cell in Figure 5.8(a) into an *in vivo* absolute concentration map, as shown in Figure 5.8. We observed intracellular AXN concentrations up to 120$\pm$10 mM, and noted that AXN content is minimal in the regions of the chloroplast. From our AstaREAL dilutions, we estimate that AXN concentrations saturate in lipid droplets at 180$\pm$20 mM, suggesting that the most abundant cellular regions are nearly saturated. We suggest that this saturation is due to the fact that pure, undiluted AstaREAL contains dense deposits of astaxanthin that appear to have this range as their upper bound for concentration.

There are several significant sources of error in this measurement which must be considered. First, we are limited by the focal volume of the microscope; hence, any droplets that are smaller than the focal volume will under-represent their concentration. Second, we are limited by the dynamic range of the instrument: The noise floor of the detector makes simultaneous collection of signals

from high and low concentration objects difficult. The detector A/D card has 12 bits (4096 units) of detection range, so if at 100 mM the detector were fully saturated, then a signal at 10 mM would be only 40 units high, essentially within the detector noise. Thus, droplets of very low concentration cannot be observed without nearby high concentration droplets saturating the detector.

The observed CARS signal intensity at low powers and lack of nonresonant background contamination suggests that the response due to astaxanthin is considerably greater than CARS signals from conventional sources, including lipids. To quantify this hypothesis, a series of experiments were undertaken comparing AstaREAL to a diamond standard. Diamond is known for its very large Raman cross section at 1334 cm^{-1} [106], conveniently located in the fingerprint region between the two major peaks of astaxanthin. Diamond, being a bulk solid, allows for easy reproduction of measurements. In Figures 5.9, we show the CARS spectrum of diamond overlaid with that of AstaREAL at various concentrations. In each spectrum, the intensity of the diamond has been corrected to account for the variation in the Stokes intensity discussed in Chapter 3.4. We see that the relative intensity of AstaREAL to diamond is about 3:1 at 45 mM concentration on the 1520 cm^{-1} peak and the signals from diamond exceed astaxanthin below 20 mM. It must be noted that the AstaREAL dilutions do not represent the highest concentrations observed either *in vivo* or in the AstaREAL compound itself; in more concentrated specimens, astaxanthin signals can exceed 400 times the intensity of bulk diamond. As noted previously, the intensity of dilute astaxanthin exceeds that of DMSO by several orders of magnitude.

5.4 Discussion

CARS offers several distinct advantages for the *in vivo* analysis of H. pluvialis. Much like spontaneous Raman, CARS is able to chemically identify astaxanthin within living cells. However, whereas fluorescence is typically an undesirable background in Raman microscopy, here we use TPEF as an additional contrast mechanism, allowing simultaneous determination of both chlorophyll and astaxanthin distributions. The large CARS signals allow for high resolution spectrally-resolved images to be generated, in only a few minutes, on live cells in aqueous solution with minimal sample preparation. Raman microscopy, on the other hand, can be performed on live cells with excellent spectral contrast, but its low signals and long integration times lead to poorer image quality, and it cannot typically be used for real-time monitoring of cells.

The substantial signals afforded by CARS allow us to observe the alga in various morphologies, and we can identify the relative maturation of the cysts by the available astaxanthin concentration. As can be seen in Figure 5.4, there are several stages of production in the encystment process. Cells with low astaxanthin density tend to have only tiny droplets scattered throughout the exterior of the cell. Production of astaxanthin requires the movement of β-carotene from the chloroplast to the lipid droplets [79], so it is reasonable to expect that the cells in the early stages of production would primarily have droplets near the edges of the cell. More mature cysts with higher astaxanthin concentrations have large drops increasingly localized in the interior of the cell, and the chlorophyll content is generally diminished due to photobleaching. Although our measurement is not directly sensitive to the nuclear material, we can likely infer the position of the nucleus in several cells due to the mapping of the astaxanthin. For example, the cell in the bottom left of Figure 5.4 shows a clear void in the middle of the cell with the astaxanthin surrounding it, suggestive of the

nucleus. This may not be visible in all of the cells, since the presented images are only at a single slice of the algal volume, which may not include the nucleus, but would be more apparent in a three-dimensional reconstruction such as in Figure 5.5.

Astaxanthin displays a fingerprint CARS spectrum that is characteristic of carotenoids, with two large peaks at 1150 cm^{-1} and 1520 cm^{-1}, and several smaller peaks, notably at 1000 cm^{-1} and 1268 cm^{-1}. As discussed above, the CARS spectrum does not experience any notable spectral distortions due to the NRB for concentrations above 1 μM, as indicated by the linearization of the concentration series in Figure 5.7(b). In the direct comparison between the CARS spectrum and the spontaneous Raman in Figure 5.6 we affirm this fact, showing that the positions of the resonances match extremely well with the spontaneous Raman. The fact that the signal is so strong and essentially background-free means that we can construct a concentration map of a cell, as shown in Figure 5.8. This provides a sophisticated analytical tool to quantitatively trace the production of carotenoids *in vivo*. Due to the presence of the nonresonant background in CARS and the inevitable transition from quadratic to linear response, quantitative CARS measurements have been fraught with difficulty and generally avoided in the literature [107], and those groups that have attempted quantitative measurements have required complex post-processing in order to address these problems [108, 109]. By comparison, we present an *in vivo* concentration map that requires no post-processing beyond fitting the measured concentration intensities to a calibration curve. We do note, however, that some care needs to be taken to use low enough powers to avoid the photobleaching of astaxanthin, as, at the power levels appropriate for analysis of lipids, there is rapid and substantial photobleaching in the CARS spectrum, and significant potential for complete cellular rupturing at higher magnifications.

Fortunately, the CARS signal from astaxanthin is extremely large. We estimate that astaxanthin produces a per molecule CARS signal that is $\sim 10^6$ times that of DMSO, as shown in Figure 5.7(a), and is comparable to bulk diamond at 30 mM astaxanthin. The CARS signal in carotenoids exceeds that of pure lipids by several orders of magnitude which, in itself, is quite remarkable considering CARS' reputation as a tool primarily for monitoring lipids.

The most natural origin for such large signals would be due to the presence of electronic resonance enhancement resulting from the interaction of the pump or probe photons coinciding with an electronically excited state in the molecules. The intensity of CARS process can be described by third order perturbation theory [12] in terms of the triple product

$$I_{CARS} \propto \left| N \sum_{k,m,l,n} \frac{\mu_{km}\mu_{nl}\mu_{ln}\mu_{nk}}{(\omega_{mk} - \omega_p - i\gamma_{mk})(\omega_{lk} - \omega_p + \omega_s - i\gamma_{lk})(\omega_{nk} - \omega_{as} - i\gamma_{nk})} \right|^2 \tag{5.3}$$

where N is the number of molecules, μ_{xy} is the transition dipole moment between states x and y, ω_{xy} is the energy difference between x and y, γ_{xy} is the linewidth associated with the transition between x and y, summed over all vibronic states of the molecule. In typical CARS experiments, $\omega_p - \omega_s = \omega_{lk} = \Omega$, for some Raman transition of frequency Ω, and the frequency denominator of the form $\omega_{lk} - \omega_p + \omega_s - i\gamma_{lk}$ would be the dominant contribution of the sum; however, further enhancement can be achieved if either of the conditions $\omega_p = \omega_{mk}$ or $\omega_{as} = \omega_{nk}$ are met. Typical enhancements resulting from resonant CARS can be of the order of 10^2 over non-electronically-resonant CARS [110].

Exploiting such enhancement underlies the principle of resonance Raman spectroscopy and has been studied extensively in gas-phase CARS spectroscopy experiments [110, 111, 112]. Enhancements of this nature are typically rarer in CARS microscopy, since absorption of relatively low-energy NIR photons partic-

ipating in CARS is somewhat uncommon and, indeed, there is only one example of this in the CARS microscopy literature, which used a specialized laser dye and did not succeed to produce any images [113]. According to the literature, it is noted that astaxanthin has a strong one-photon allowed transition at 488 nm, and a two-photon allowed but one photon-forbidden transition at 751 nm ($S_0 \rightarrow S_1$) [99], neither of which can obviously participate in a CARS process with a 915 nm pump, as summarized in Figure 5.10. Since astaxanthin is a large, flexible molecule in solution, it is possible that the strict parity selection rules for the two-photon transition are partially relaxed, potentially allowing some enhancement due to the $S_0 \rightarrow S_1$ transition. Were this the case, however, we should see an absorption band in the UV-Vis absorption spectrum corresponding to this transition. However, as seen in Figure 5.2, the band peaks at the expected position of 480 nm, ruling out the possibility of absorption shifts due to aggregation [114], and no peak at 751 nm is observed, suggesting that there can only be minimal contribution from the S_1 state in this instance.

In Figure 5.11, we show the dependence of the CARS response on wavelength in the regime from 890-925 nm. These measurements are calibrated relative to that of diamond. As can be seen, the response varies minimally with wavelength; there is no more than a factor of two increase in intensity over this regime. This may indicate that there is some resonance below 930 nm that is enhancing the CARS process, but this seems unlikely given the absorption spectrum. We assert, therefore, that electronic resonance enhancement, at least through the conventional means described by Equation 5.3, cannot adequately explain the observed spectra of astaxanthin in *haematococcus pluvialis*.

As noted, astaxanthin plays a key role in dissipating excess energy from absorbed light within the cell. The mechanism for energy dissipation is typically via the production of astaxanthin radicals [115, 116]. We therefore must consider

the possibility that an appreciable quantity of the astaxanthin under study could be the radical form of astaxanthin, AXN*, and that there may be some enhancement mechanism via the energy levels of the radicals. In particular, it is notable that the astaxanthin radical appears to have an energy level at 890 nm, which more closely aligns with our CARS scheme [117].

We created two solutions containing astaxanthin and AXN* at equal concentrations in acetone. In Figure 5.12(a), we show the spectra of astaxanthin and its radical. As can be seen from the figure, there is a dramatic *decrease* in the signal intensity in the AXN* as compared to pure astaxanthin. The signal intensity is approximately a factor of 25 lower in the radical solution than in the pure astaxanthin solution. Moreover, we observe a surprising 29 cm^{-1} spectral shift of the 1520 cm^{-1} peak to 1549 cm^{-1}. In Figure 5.12(b), we see that in the radicalized solution, there is a near-complete suppression of the 480 nm absorption peak (and, likewise, a colour-change in the sample from red-brown to green, presumably from the chlorophyll contaminant). Nonetheless, we are still able to observe an astaxanthin spectrum in the radical solution. This yields a critical observation: The *enhancement* is somehow associated with the 480 nm electronic resonance, but this does not lead to a complete destruction of the carotenoid entirely, as the spectral shape is essentially unchanged. This is consistent with our observations of bleaching: At high powers, rapid photobleaching of the astaxanthin was observed, but the bleaching appeared to saturate at some nonzero (and still appreciable) signal intensity. This was commensurate with a disappearance of the red colouring of the algae.

We summarize the key observations as follows: 1) Astaxanthin produces a CARS response that is several orders of magnitude greater than expected when compared to lipids and other calibration standards on a per molecule basis; 2) The large signals provide a significant advantage for the study of carotenoids in

an essentially background-free manner, allowing for quantitative concentration measurements down to 100 μM; 3) The energy of the participating photons are well below the energy lowest electronic resonance; 4) The response is nearly wavelength independent, at least over the limited excitation regimes probed here; 5) The response is nonetheless *associated* with the resonance, such that the enhancement can be destroyed due to either photobleaching or the chemical change from astaxanthin to AXN*; 6) The CARS response appears to be completely uncontaminated by the NRB. This final point requires some further elaboration. As noted in Chapters 2 and 4, when the CARS response is very large compared to the NRB, spectral reshaping is generally minimized. Given that we are describing one of the largest CARS signals ever encountered, it should be unsurprising that we do not experience any NRB. However, as hinted at in the Chapter 5.3, there is, in fact, a rather large NRB present in the spectrum of astaxanthin. As we will see in Chapter 6, not only does astaxanthin produce a tremendously large native CARS response in the fingerprint, but also a tremendously large non-vibrationally resonant FWM response. While smaller than the CARS response, the NRB is by no means dwarfed by the CARS signal as one might expect in this scenario.

Based on this evidence, we conclude that the signal enhancement in astaxanthin cannot be due to an electronic resonance enhancement in the conventional understanding from Equation 5.3. In Chapter 6, we will outline crucial evidence resulting from nonresonant four-wave mixing in astaxanthin, which will enable us to create a model that is able to encapsulate these dischordant measurements, discussed in Chapter 7.

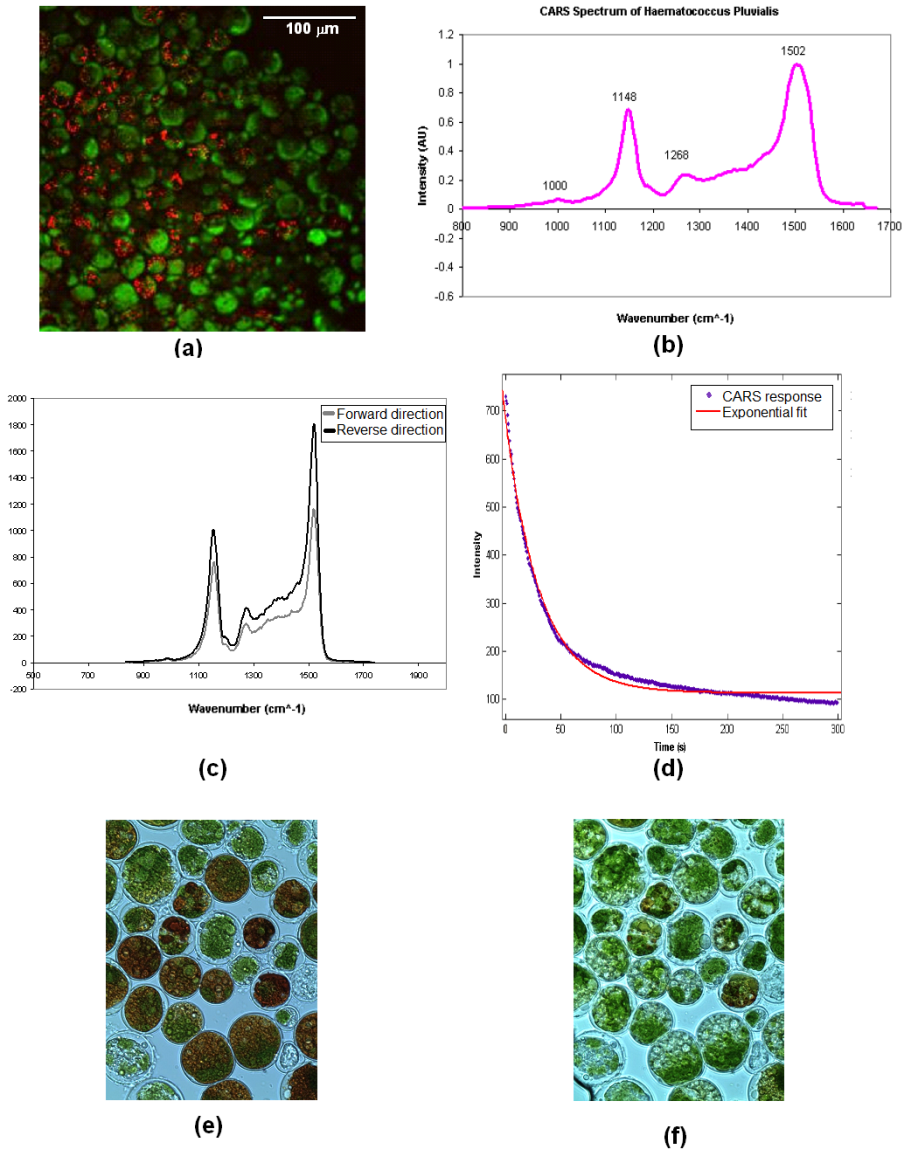

Figure 5.3: (a) Wide-field image of *haematococcus pluvialis* algal cysts at 1520 cm^{-1} CARS peak (red) with TPEF (green). (b) Typical CARS spectrum of isolate *haematococcus pluvialis* cyst at high power. Notable peaks at 1000 cm^{-1}, 1148 cm^{-1}, 1268 cm^{-1} and 1520 cm^{-1}. (c) Photobleaching response of CARS signal at 100 mW pump (blue), fitted with an exponential curve (red). (d) CARS spectrum photobleaching over the course of stage travel. (e) Transmitted light of *haematococcus pluvialis* cells before exposure. (f) Transmitted light image of *haematococcus pluvialis* cells after 3 min exposure at 100 mW.

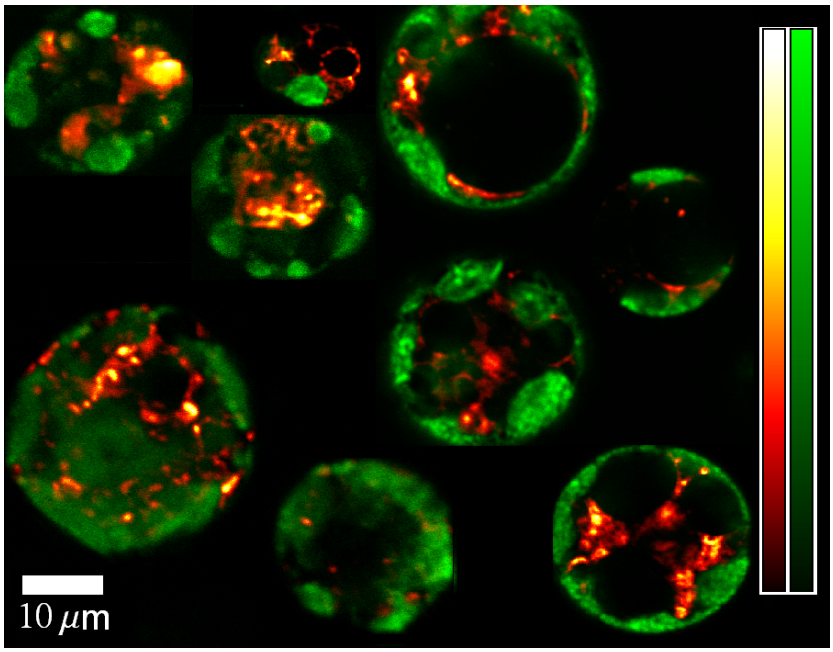

Figure 5.4: Composite image of various *haematococcus pluvialis* cysts using forward-collected CARS from astaxanthin at 1520 cm-1 (red) and epi-collected TPEF from chlorophyll (green). The cells show several distinctive morphologies, ranging from minimal astaxanthin content within a chlorophyll-dominated cell, to those with several astaxanthin-containing droplets, to cells where astaxanthin almost completely dominates the interior of the cell. Several cells also appear to have large transparent voids within them.

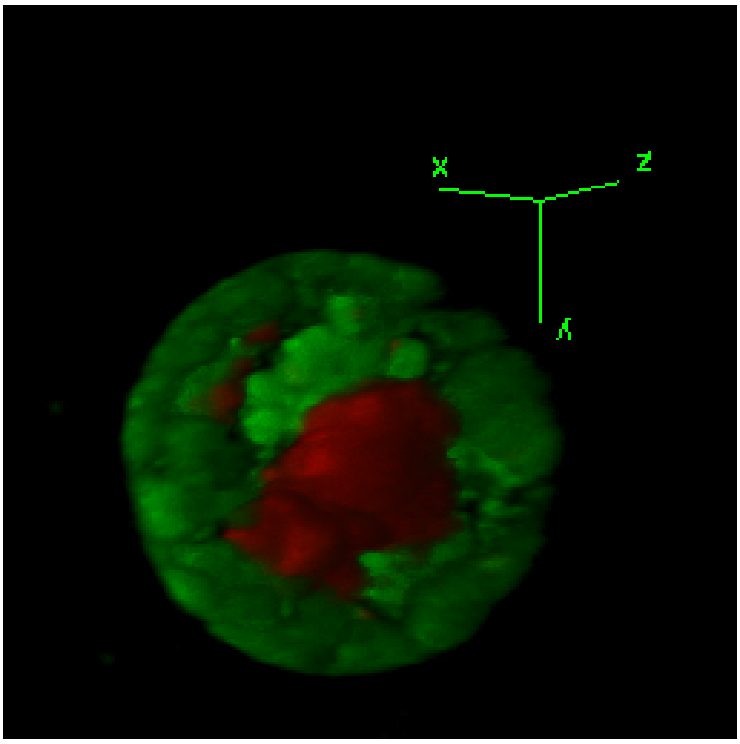

Figure 5.5: Three-dimensional reconstruction of an algal cyst using CARS at 1520 cm^{-1} (red) and TPEF (green), generated by 1 μm slices.

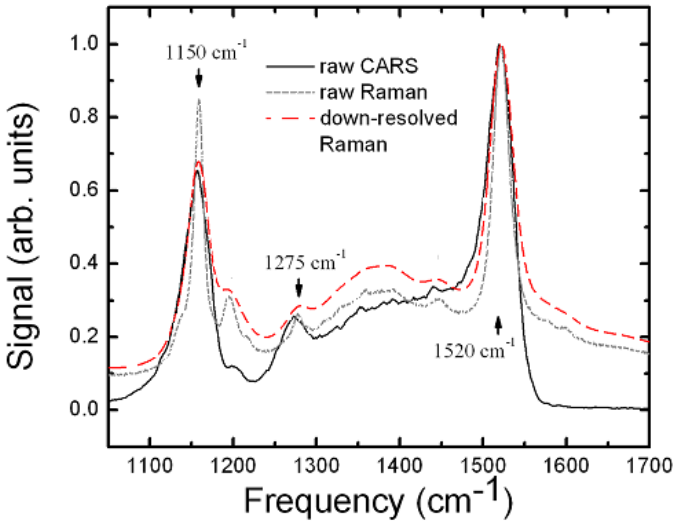

Figure 5.6: Black: Raw CARS spectrum extracted astaxanthin in *haematococcus pluvialis*. Grey: Spontaneous Raman spectrum of AstaREAL standard collected with a Raman spectrometer. Red: The same Raman spectrum after being broadened to the CARS spectral resolution of 30 cm^{-1}.

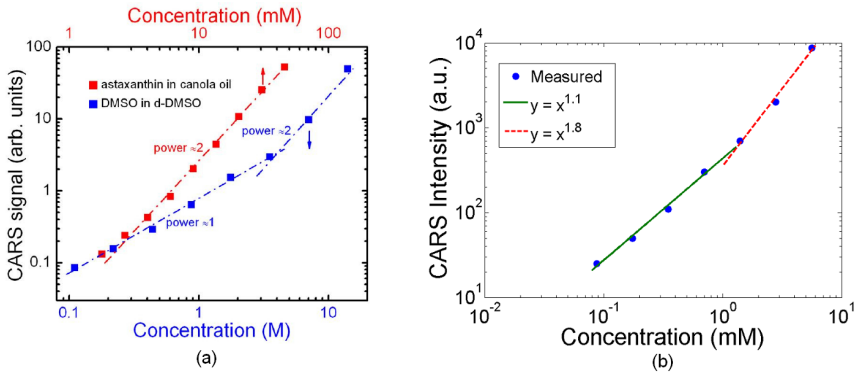

Figure 5.7: (a) Plot of AstaREAL concentration and d-DMSO mixed in DMSO mixture. At high concentrations, both are quadratic, but below $\sim$ 5 M, the DMSO concentration dependence linearizes. By comparison, astaxanthin maintains its quadratic (eg. high signal) character down to the lowest measured concentration of 1.8 mM. (b) Using the C' series, the concentration dependence is extended into the sub-millimolar regime. At higher concentrations, the dependence is nearly quadratic ($x^{1.8}$ power), whereas at low concentrations it is nearly linear ($x^{1.1}$)

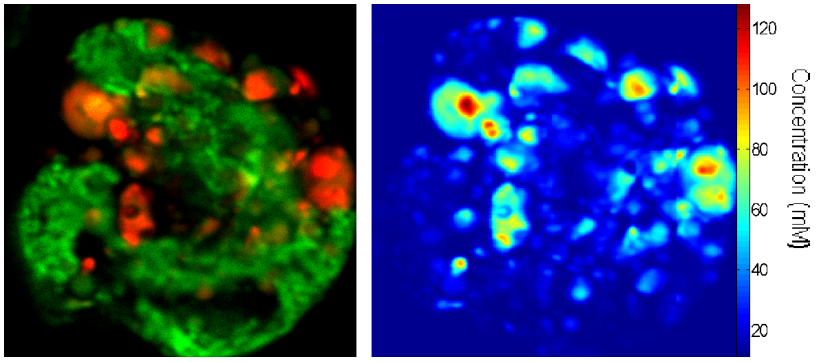

Figure 5.8: Left: CARS and TPEF image of *haematococcus pluvialis* alga in solution. Right: Absolute astaxanthin concentration map generated from this alga using the calibration in Figure 5.7(b)

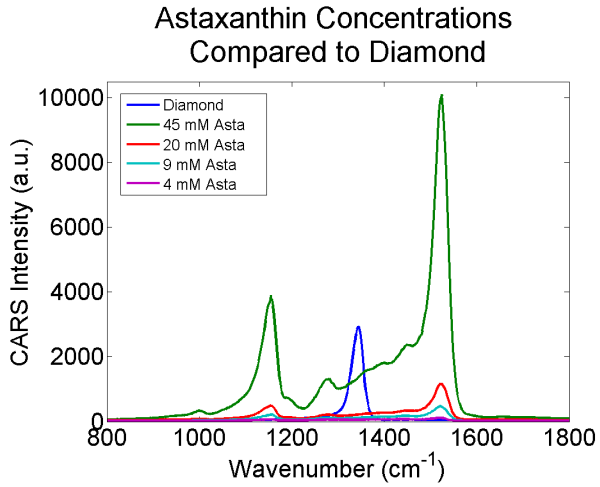

Figure 5.9: AstaReal dilution series compared to the intensity of bulk diamond.

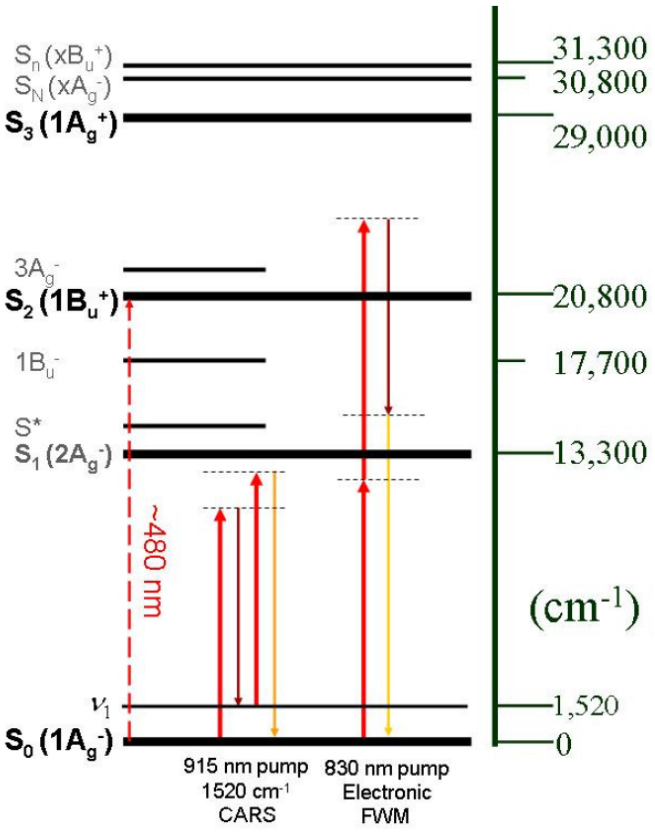

Figure 5.10: Known energy levels in AXN overlaid with experimental excitation scheme used for CARS and FWM. The lowest electronic transition, $S_0 \rightarrow S_1$ is one-photon forbidden. In the left scheme, for CARS signals from the S1 vibrational mode in AXN, pump and probe wavelengths of 915 nm (red arrows) are 1520 cm^{-1} higher in frequency than the Stokes wavelength of 1062 nm (smallest downwards arrow, brown), and the collected anti-Stokes signal is at 803 nm (largest downward arrow; yellow). None of these wavelengths are resonant with any known dipole transition. In the scheme on the right, for strong degenerate FWM signals in AXN, the pump wavelength is 830 nm (red arrows), and the signal is detected nominally at 650 nm (large yellow downwards arrow). Note that in this case the process does not appear to be resonant with any one- or two-photon allowed transitions. (Figure compiled and composed by Dr. Aaron Slepkov)

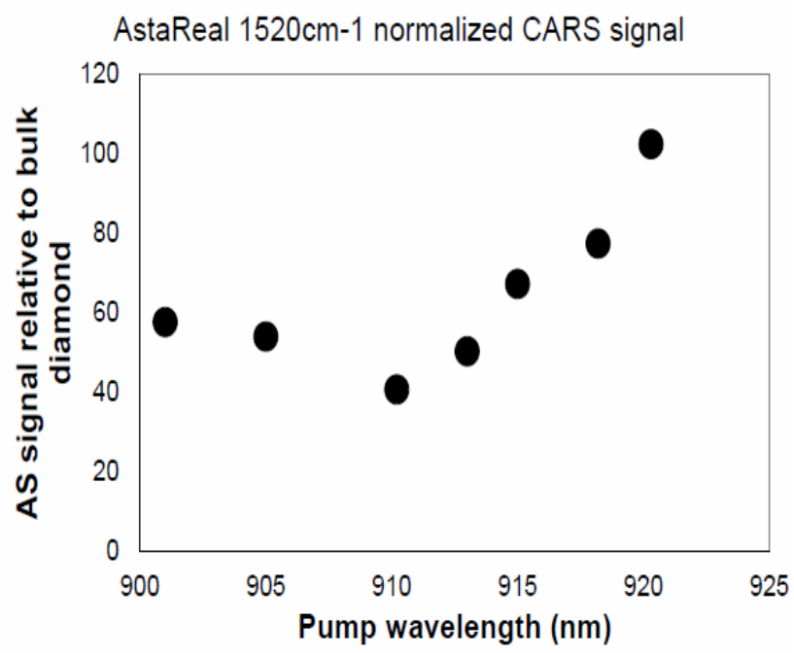

Figure 5.11: Measured intensity of high concentration astaxanthin in canola compared to diamond, as a function of the pump wavelength.

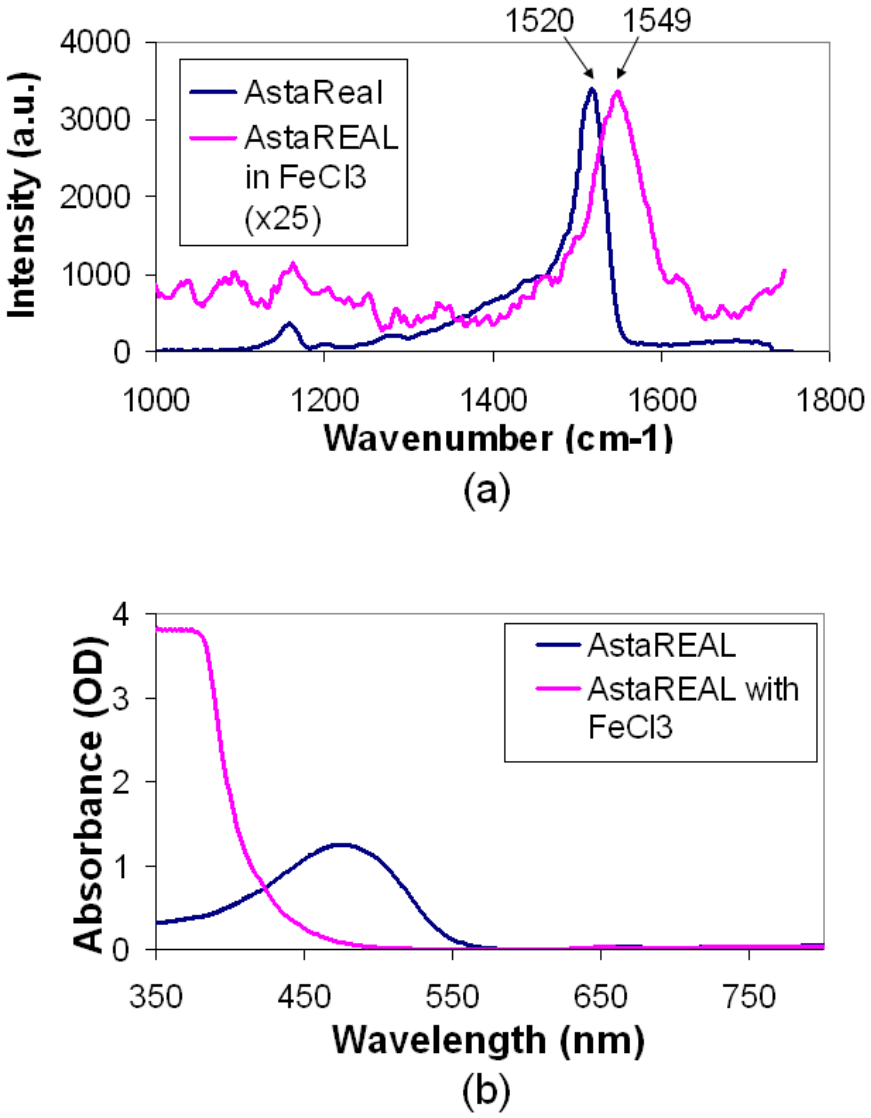

Figure 5.12: (a) Measured CARS spectrum of AstaREAL and AstaREAL in $FeCl_3$. $FeCl_3$ spectrum is multiplied by 25×. The main peak has a spectral shift of the main peak 29 cm^{-1}. (b) Absorption spectrum of AstaREAL and AstaREAL in $FeCl_3$.

6 Four-Wave Mixing Microscopy of *Haematococcus Pluvialis*

6.1 Introduction of Four-Wave Mixing Microscopy

In our previous discussions in Chapters 2 and 4, the NRB has been noted to generally be a detriment to CARS microscopy experiments due to the creation of unwanted spectral distortions that complicate the analysis of CARS spectra. The NRB is the result of a four-wave mixing (FWM) process produced coherently and concurrently with the CARS process and, while on a per-molecule basis FWM is generally much weaker than resonant CARS, due to the fact that it is generated ubiquitously throughout the focal volume, the number of contributing molecules may exceed that of CARS by many orders of magnitude, resulting in appreciable signals. The FWM response depends on the non-vibrationally-resonant $\chi^{(3)}_{FWM}$ of the interacting molecules and it is thus possible to generate contrast using FWM alone, provided that there are large variations in $\chi^{(3)}_{FWM}$ among the constituents of a sample.[2] Unlike CARS, the FWM signal is insensitive to vibrational resonances and rather relies on electronic variations in $\chi^{(3)}$ for image contrast. This is analogous to the situation in third-harmonic generation microscopy, where contrast can be generated by polarizability variations manifest in nonresonant third harmonic signals. While this means that the FWM signal will not produce spectra, it is also relatively insensitive to the specific frequencies of pump and Stokes, meaning that FWM imaging can, in

[2]There is some confusion in the literature over the naming conventions for FWM, CARS, and the NRB. For our purposes, CARS will refer to vibrationally resonant four-wave mixing and will have a susceptibility $\chi^{(3)}_R$; FWM will refer to vibrationally non-resonant four-wave mixing exclusively, which will have a susceptibilty donated by $\chi^{(3)}_{FWM}$. We will refer to FWM in this context only when it is used as an imaging modality. Although FWM and the NRB are the same physical process, we will use the term NRB to describe the undesirable background FWM that, in this case, derives primarily from the solvent. We will reserve the term $\chi^{(3)}_{NRB}$ for the NRB. For simplicity's sake, we will use the terms pump, Stokes, and anti-Stokes for the incoming photons regardless of the process under discussion.

principle, be achieved with a far simpler apparatus, notably one without spectral scanning capacity. FWM microscopy is generally applied to inorganic systems such as metal surfaces, semiconductors, and quantum dots[118, 119, 120, 121]. In these systems, electronic or plasmonic, rather than vibrational, resonance enhancement is typically used in order to ensure that the signals are sufficiently large for imaging[119]. In the NIR region, biological systems typically lack such resonances, and generally *in vivo* FWM measurements are only done using a label, such as a gold nanoparticle to provide a conduit for resonance enhancement [122]. In this Chapter, we provide among the first demonstrations of FWM microscopy applied to a native biological system [123]. The astaxanthin in *haematococcus pluvialis* discussed in Chapter 5 provides not only a tremendous CARS response in the fingerprint, but also, as we will demonstrate, a FWM response allowing for remarkable contrast imaging of *in vivo* carotenoids. These measurements will augment our previous discussion of signal enhancement in CARS, and will allow us to move toward a unified model to explain both phenomena in Chapter 7.

6.2 Theory of Four-Wave Mixing

In Chapter 2.1, we outlined a classical argument using Maxwell's equations to describe the general characteristics of the CARS process. In particular, we demonstrated classically that CARS operates at a frequency of $\omega_{aS} = 2\omega_p - \omega_S$, that the CARS intensity depends on the square of the pump power and linearly with the Stokes, and that the CARS process depends quadratically on the concentration of resonant oscillators in the medium. We also noted that the same argument essentially holds for FWM since the classical argument does not require any explicit reference to the presence of the vibrational resonance. Thus generally, the results as derived in Equations 2.9-2.10 hold for FWM as well as

CARS, which we reproduce below:

$$E_{FWM}(L) = \frac{i\omega_{aS}L}{8c}\chi^{(3)}E_p^2E_S^*\mathrm{sinc}\big(\frac{\Delta kL}{2}\big)e^{i\Delta kL/2} \tag{6.1a}$$

$$I_{FWM}(\omega) \propto |\chi^{(3)}_{FWM} + \chi^{(3)}_{NRB}|^2 I_p^2 I_S L^2 \tag{6.1b}$$

where we have used the subscript FWM to emphasize the fact these equations refer to FWM rather than CARS. In Equation 6.1(b), we have separated the contribution $\chi^{(3)}_{FWM}$ due to the FWM from that of the NRB, $\chi^{(3)}_{NRB}$. This distinction is artificial, as the physical process that creates the NRB is the same as that for FWM. The difference for FWM microscopy is that particular collections of molecules will have a significantly enhanced response compared to the conventional background–the solvent, for example–that allows for contrast to be generated. For example, in the specific case of astaxanthin, we will see a substantial FWM signal enhancement that is significantly above the background due to the surrounding water, in the case of *haematococcus pluvialis*, or due to the canola oil solvent, in the case of AstaREAL. Thus, there is some use in separating the components that are signal from those that are background. Unlike CARS, however, the behaviour of FWM differs with respect to the NRB. In particular, if the $\chi^{(3)}_{FWM}$ does not impinge on an electronic or vibrational resonance, then there will be no interference term in Equation 6.1(b), and consequently no distortions. As a result, in cases where the FWM is nonresonant vibrationally and nonresonant electronically, the signal dependence on the concentration, i.e., the number of oscillators, will always be quadratic.

An exception to this is if the FWM impinges on an electronic resonance. As noted above, this is often the case in FWM microscopy applications, since the native $\chi^{(3)}_{FWM}$ of most molecules is quite small. Most commonly, the FWM will be driven by a two-photon resonance at frequency $2\omega_p$. In this case, there will

indeed be an interference between the FWM and the NRB in much the same manner as with CARS. If we expand the total $\chi^{(3)}$ in a perturbative expansion, separating the one-and-two photon resonant contributions, then it is of the form [119]:

$$\chi^3(-\omega_{aS};\omega_p,-\omega_S,\omega_p) = \chi^{(3)}_{NRB} + \sum_r \Big(\frac{A_r}{\omega_r-(\omega_p-\omega_S)-i\Gamma_r}\Big) + \sum_t \Big(\frac{A_t}{\omega_t-2\omega_p-i\Gamma_t}\Big) \tag{6.2}$$

where r and t are Raman-active (i.e. CARS) resonances and two-photon resonances, respectively, at frequencies ω_r and ω_t with linewidths Γ_r and Γ_t. The three terms thus represent completely nonresonant contributions, CARS, and two-photon-enhanced FWM, respectively. Note that the two-photon-enhanced FWM, due to its resonant character, is complex. When it is enhanced in this manner, it creates an interference with the NRB. However, if both two-photon-enhanced FWM and CARS are present, then the two add constructively. In particular, rather than Equation 2.12 to describe the interference, we use the following:

$$\begin{aligned}|\chi^3(-\omega_{aS};\omega_p,-\omega_S,\omega_p)|^2 = {} & |\chi^{(3)}_{CARS}|^2 + |\chi^{(3)}_{FWM}|^2 + |\chi^{(3)}_{NRB}|^2 + 2\Re\Big(\chi^{(3)}_{CARS}\chi^{(3)}_{FWM}\Big) \\ & + 2\Im\Big(\chi^{(3)}_{CARS}\chi^{(3)}_{FWM}\Big) + 2\chi^{(3)}_{NRB}\Re\Big(\chi^{(3)}_{CARS}+\chi^{(3)}_{FWM}\Big)\end{aligned} \tag{6.3}$$

Equation 6.3 includes the contributions from the real and imaginary parts of the CARS and FWM processes, as well as the NRB. The first three terms describe the quadratic components of the NRB, CARS, and two-photon-enhanced FWM. Generally, the NRB term will be negligible. The fourth and sixth terms are the usual dispersive terms that generate the CARS lineshape. The fifth term deserves some additional comment. This term involves an interaction between

the resonant contributions of the CARS and FWM processes. Far from a two-photon resonance, this term is negligible; however, near resonance, this term adds constructively with the resonant CARS term and provides a moderate enhancement to the signal intensity. If, on the other hand, we are far from a CARS resonance, then only the second, third, and final terms of Equation 6.3 will be appreciable, and we may see some dispersion between the FWM and the NRB.

6.3 Method and Materials

Introduction

FWM is a nonlinear process that depends primarily on the intrinsic nonlinear susceptibility of the material, $\chi^{(3)}$. As such, it is essentially independent of the pump and Stokes powers used, save for when the interaction of these impinges on an electronic resonance in the system. As alluded to above, this simplifies the experimental procedure considerably, as we are not required to find a time-zero for a particular Raman resonance; indeed, we do not need to scan the Stokes or use a chirp-matched technique at all. In fact, there are significant advantages to not using the chirp-matched technique, as the chirp-matched FWM response will be proportional to the variations in the Stokes spectrum, whereas in the unchirped case, the FWM loses this dependence–generally, the FWM intensity increases the less chirp is present. Unlike CARS, where there is a spurious debate between whether fs or ps pulses are superior, in FWM the overriding concern is optimizing the peak power as considerations about the spectral resolution are entirely unnecessary, and thus transform-limited fs pulses are the best choice.

For the most part, we undertook FWM microscopy using the standard chirp-matched apparatus nonetheless, as it provides a more accurate comparison of the relative intensities of the FWM to that of CARS per unit bandwidth. In

particular, we worked primarily in the C-H region near 800 nm, with periodic detours into the fingerprint. Imaging was typically done by selecting the frequency that optimized the FWM signal, which, in turn, corresponds to the maximum of the Stokes spectrum. The signal-to-noise could then be vastly improved by integrating the FWM response per unit bandwidth into a single image frame, which provides the complete FWM signal.

Video Collection

Flagellated algae from the nitrogen-enriched sample described in Chapter 5.2 were selected as a focus of study. Due to the rapid motions of these algae under observation, spectral scanning in this case is not possible; thus CARS provides no advantage over FWM in this case. The stage position was fixed at the peak of the Stokes intensity as measured by the OSA. Under such circumstances, rather than collecting a spectrum, time scanning instead provides the ability to track the cellular motion at the rate of image acquisition, namely 2.8 frames per second on a 256×256 field. Regrettably, the frame rate is ultimately limited by the scanning speed of the galvo scanning mirrors in the microscope, as well as hard-coded limitations in the commercial software. In principle, however, this problem is not intractable and can be overcome by a software solution or improved hardware. There is also a compromise between frame rate and pixel dwell time; increasing the frame rate to video rates (24 fps) would reduce the pixel dwell time, and thus the signal intensity, by a factor of order 10. In this instance, such a sacrifice might have been merited, were it possible, due to the large signal strength in astaxanthin. The signal-to-noise ratio is of order 50:1, so improving the frame rate to video rates would still allow for a 4:1 signal-to-noise ratio.

There is some difficulty in collecting videos of the motile algae in the well slide, as the microscope does not automatically track the position of the algae,

and, in particular, their position in the focus. Thus motions in the axial direction that significantly exceed the focal distance, 1-2 μm, cannot be tracked particularly precisely, and large motions in this direction will cause the specimen to disappear entirely. Purely transverse motions could be tracked across the entire frame, and this could be extended further by careful adjustment of the transverse stage position as appropriate to recentre the algae.

Wavelength Dependence

The intensity of the FWM response was collected as a function of wavelength between 800-870 nm. DMSO was chosen as a calibration standard, as it produces a strong CARS response at 2900 cm^{-1}. The solution C_2', as described in Chapter **??**, with a concentration of 2.8 mM carotenoid, produces a comparable intensity per unit Stokes bandwidth to DMSO so that measurements could be taken of the two samples within the same dynamic range at the same PMT settings. Thus, we could use the ratio of the FWM to the DMSO signal at the same stage position, corresponding to 2900 cm^{-1}, as a metric to calibrate how the FWM intensity changes with pump wavelength (assuming the CARS from DMSO does not, which is reasonable as the UV-Vis absorption spectrum of DMSO peaks at 275 nm).

6.4 FWM Microscopy of *Haematococcus pluvialis*

FWM microscopy of *haematococcus pluvialis* was undertaken using the standard setup described in Chapter 3.2 with the laser tuned to the 815 nm with typical 'pump' powers of 5-10 mW and typical 'Stokes' powers of 15 mW. A flagellated alga is shown in Figure 6.1(a)-(d), whose motion can be tracked at 2.8 frames per second in a 256×256 field. The chlorophyll content is traced by TPEF in green, while astaxanthin is in this case associated with FWM in red.

In the series of frames of Figure 6.1, we can observe that the algae is undergoing a rapid spinning motion, and can be followed for extended periods of time. Likewise, we can follow the transverse motion of the algae over a larger field of view as shown in Figure 6.2(a)-(h). The ability to monitor the motions of living cells is a significant advantage, notably one that would not be possible with, for example, spontaneous Raman microscopy, as the integration time needed to collect the signal would greatly exceed the timescale of the motions. Somewhat surprisingly, these algae appear to contain small pockets of carotenoid at their centres, despite the fact that astaxanthin production in significant quantities is generally associated with encystment [78]. Nonetheless, astaxanthin accumulation in flagellates has observed previously under high light conditions, and it has been argued that initial astaxanthin production is a herald of encystment [124].

In Figure 6.3(a), we observe an algal cyst using FWM and TPEF. The FWM response is comparable to that seen with CARS, with a high signal-to-noise and clear differentiation between astaxanthin and chlorophyll. In Figure 6.3(b) we show the FWM response as a function of the frequency difference between the pump and Stokes fields. While the FWM spectrum does display some structure, as noted above, the structure is not associated with resonances in astaxanthin, but rather is proportional to the measured spectrum of the Stokes supercontinuum through the optical spectrum analyser. Affirming this, it can be seen that the 'spectral' features in the FWM signal are considerably broader than the vibrationally resonant features in the fingerprint region spectrum, as can be seen by the overlaid Raman spectrum in red, and no Raman features are expected in the 2500-3000 cm^{-1} region. As discussed above, the intensity of the FWM as a function of frequency is essentially an artefact of the scanning scheme in our system, and a more accurate representation of the FWM response

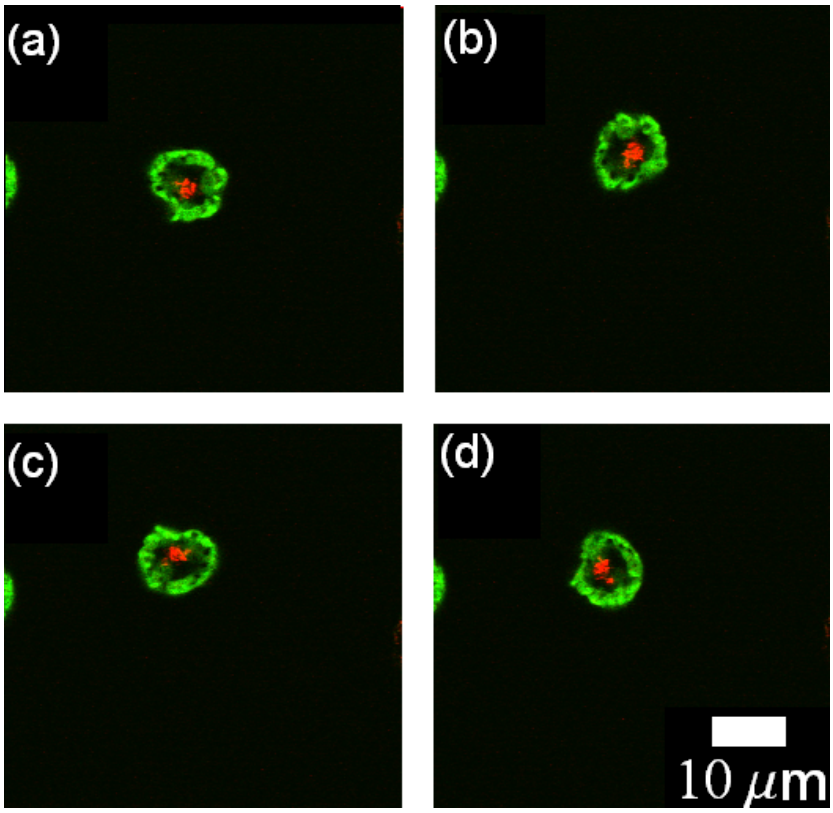

Figure 6.1: (a)-(d) Position of a spinning algae as a function of time. FWM is highlighted in red, TPEF in green. Frames are spaced 0.44 s apart.

would involve the integration of the frequency spectrum. We can see this in Figures 6.3(c) and (d). In Figure 6.3(c), we see a single-slice image at a particular frequency, equivalent to the type of image at a CARS peak; in Figure 6.3(d), we show the same image, this time integrated over all Stokes frequencies, and observe an improvement in signal-to-noise. We do not see the C-H vibrational resonance characteristic of lipid drops at 2850 cm^{-1}. This is uncharacteristic, as typically a resonance CARS response should significantly dominate over a nonresonant FWM response. As we have alluded to in the previous Chapter, the CARS response from carotenoids easily overwhelms that of lipids by several orders of magnitude; what is more remarkable is that the FWM (ie. the

nonresonant background) produced by astaxanthin also overwhelms that of vibrationally resonant lipids.

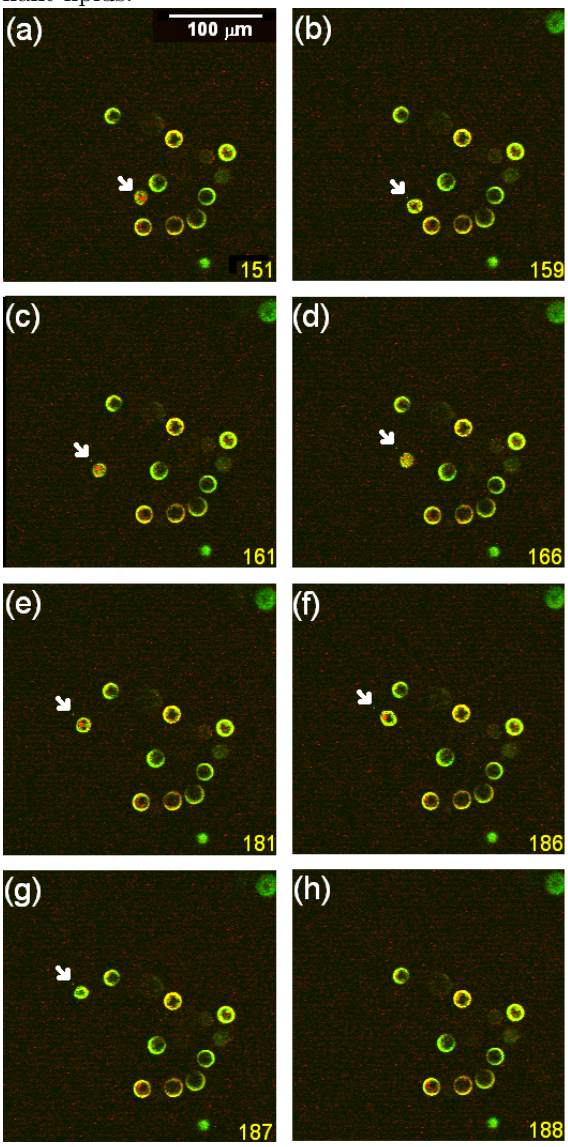

Figure 6.2: (a)-(h) Position of the highlighted algae as a function of time. Frame numbers are indicated in yellow, spaced 0.44s apart. FWM is highlighted in red, TPEF in green. In frame (h), the algae has moved out of the microscope focus in the z direction and cannot be observed.

In Figure 6.4, we show a composite image of several algae in various stages of development. Comparing to Figure 5.1, we see that we are able to track the

various stages of the algal life cycle from the flagellated stage through encystment to cell division, and, moreover, we can observe the relative amounts of astaxanthin in the algae at any given point in the cycle.

In Figure 6.5, we observe the per-unit-frequency FWM intensity of 2 mM astaxanthin measured at 2850 cm^{-1}, compared to the resonant response of DMSO at various pump wavelengths. The FWM response shows only a weak wavelength dependence, of order a factor 2, across the regime from 800-870 nm, which is the extent of the C-H detection system. More significantly, the concentration of neat DMSO is of order 14 M, whereas the concentration of astaxanthin in this measurement is 2 mM, so the signal intensity of the FWM is of order 10^7 times greater than that of the resonant DMSO on a per-molecule basis. Comparing this to Figure 5.7, we can see that the FWM intensity is rather comparable to that which we observe from CARS in the fingerprint regime.

It is instructive to compare the relative strengths of CARS and FWM in astaxanthin. In Figure 6.6(a), we see the response of both CARS and FWM measured simultaneously with a 860 nm pump. This spectrum extends from 1300cm^{-1} to 2500cm^{-1} in this instance, so only the 1520 cm^{-1} peak in astaxanthin is visible. Figure 6.6(a) shows that, at this wavelength, the CARS response is about seven times larger than the FWM. Despite this, we see minimal reshaping in the CARS peak at 1520 cm^{-1}. The FWM can also be observed in the fingerprint region. In Figure 6.6(b), we show a spectrum of the fingerprint region that has been intentionally saturated at the 1520 cm^{-1} peak to better show the NRB contribution. There is a notable feature at 2100 cm^{-1} that does not correspond to any Raman resonance in astaxanthin, but rather is a definite feature of the FWM. Examining the spectrum of pure canola oil under the same conditions, as in Figure 6.6(c), we can see that there is a feature in the FWM at 2100 cm^{-1} here as well. Since canola oil does not have any spectral features in

the fingerprint region, we can use its spectrum as model for the Stokes spectrum, and thus, based on the relative intensity of the 2100 cm^{-1} peak, estimate the FWM intensity per unit frequency. Using this model, we construct, in Figure 6.6(d), the expected FWM intensity. As in the case of the 860 nm pump, the expected FWM response due to the astaxanthin comparable, though smaller, to that of the resonant CARS. The peak of the Stokes spectrum, and therefore the FWM intensity is relatively large close to the 1520 cm^{-1} CARS peak, but minimal reshaping is observed.

6.5 Discussion

In this Chapter, FWM is presented as a parallel implementation of CARS for the study of carotenoid molecules. In particular, we demonstrated that FWM has the capacity to create high-contrast imaging of living biological systems, notably the algae *haematococcus pluvialis*, and determine their composition. FWM boasts several significant advantages over CARS for this type of imaging. FWM can use transform-limited fs pulses to achieve much higher peak powers than a typical chirp-matched CARS configuration, which, in turn, yields higher signals. This is somewhat offset by the fact that the higher peak powers may lead to increased rates of photobleaching, and lower average powers may be required [42]. Because FWM does not require spectral scanning, the signal-to-noise of FWM can be significantly enhanced compared to CARS, as we can use the entire Stokes bandwidth for imaging, as shown in comparison between Figures 6.3(c) and (d). For videography, such as those shown in Figures 6.1 and 6.2, this is particularly relevant, as it is not possible to simultaneously scan the spectrum and track the position as a function of time in this implementation.

In Figure 6.4, we demonstrate how FWM can be used to monitor carotenogenesis in *haematococcus pluvialis*. Our TPEF/FWM system allows us to mon-

itor the carotenoid concentrations within the cells to the submillimolar level, allowing for a high degree of contrast between the various stages. Our results generally support models emphasizing carotenogenesis as a precursor–or even a trigger of–algal encystment [124]: we observe significant carotenoid deposits present in the several flagellated cells and increasing carotenoid density as throughout the encystment process. While the monitoring of a single cell throughout its entire life cycle is currently beyond our capabilities due to our inability to track the motions of the flagellated cells for extended periods of time, we provide a proof-of-concept of a methodology that would allow a complete understanding of the carotenogenesis process in live cells, buttressed by calibrated assays of intracellular carotenoid.

As we have alluded to earlier, the primary reason for the distinct advantage of FWM in *haematococcus pluvialis* studies is due to the remarkable signal enhancement of the FWM. The enhancement far exceeds what would be typically expected from NRB signals in fingerprint CARS microscopy and it is this enhancement that engenders our demonstration of live-cell FWM imaging. Like the CARS response, we see that there is a minimal change in the FWM signal as a function of wavelength–no more than a factor of two–across the range from 815-870 nm, as shown in Figure 6.5. This is somewhat anticipated, as the S0→S2 resonance (480 nm) is two-photon forbidden; the S0→S1 resonance is two-photon allowed, but is quite distant from any of the participating photons in this case. It is nonetheless possible that this resonance produces a contribution to this interaction, but is sufficiently far away that wavelength-dependent intensity changes are not significant over the scale that we are observing. In practical terms, however, we are unable to obviously assign the enhancement to any simple one- or two-photon electronic resonance.

Given that the CARS signal is only seven times as large as the FWM, it is

somewhat remarkable that minimal spectral reshaping is observed in the CARS spectrum. The appearance of the CARS spectrum, accounting for our spectral resolution and the variations in the Stokes power across the bandwidth, is remarkably consistent with the spontaneous Raman spectrum, as shown in Figure 5.6. These observations are somewhat dischordant with our understanding of the interactions between CARS and the NRB producing the signal, as discussed in detail in Chapter 2.1, namely that the interference between CARS and the NRB should produce a spectral distortion. Even when the data strongly suggests that the FWM in the fingerprint ought to be sufficiently large to produce spectral distortions, the CARS spectra appears minimally perturbed. This behaviour might lead us to conclude that resonance enhancement of the FWM is a strong possibility, as this would favour the enhancement term in Equation 6.3 over the dispersive term. Unfortunately, entirely aside from the fact that the participating photons in the FWM do not impinge on any electronic resonances, it is somewhat unsatisfactory to assert that the CARS response in astaxanthin is somehow also enhanced through some other means and the enhancement of the CARS is coincidentally within an order of magnitude of the electronic resonance enhancement of the FWM at the wavelengths we are using. Rather, it seems far more plausible that the same mechanism that supplies an enhancement to the CARS process applies an enhancement of similar magnitude to the FWM process. Such a unified treatment, as we will present in Chapter 7, must invariably be a mechanism that is independent of the specific pump and Stokes frequencies applied, both to be consistent with our wavelength measurements, and to account for the differing resonance conditions of the two processes.

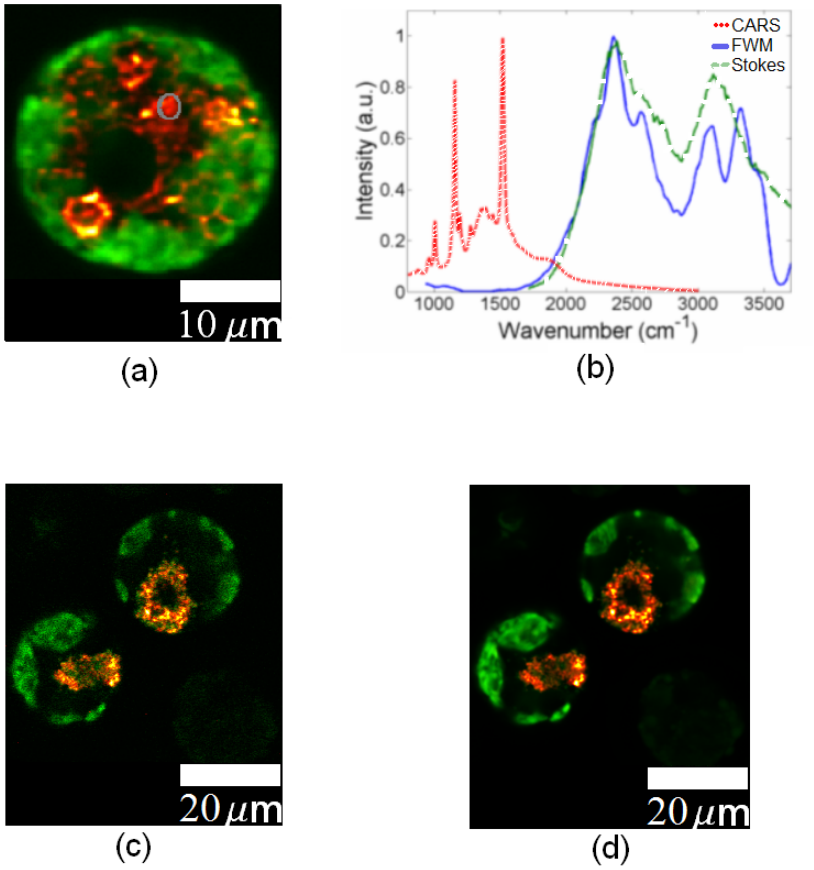

Figure 6.3: ((a) FWM image of a particular *haematococcus pluvialis* cell. (b) The frequency difference $\omega_1 - \omega_2$ of the FWM of the highlighted region of (a), shown in blue. The frequencies generated by the Stokes supercontinuum are shown in green. For comparison, the spontaneous Raman spectrum collected at 785 nm of AstaREAL is plotted in red. (c) A FWM image of a *haematococcus pluvialis* cysts collected using a single FWM frame. (d) A FWM image of the same *haematococcus pluvialis* cysts, integrated over all Stokes frequencies.

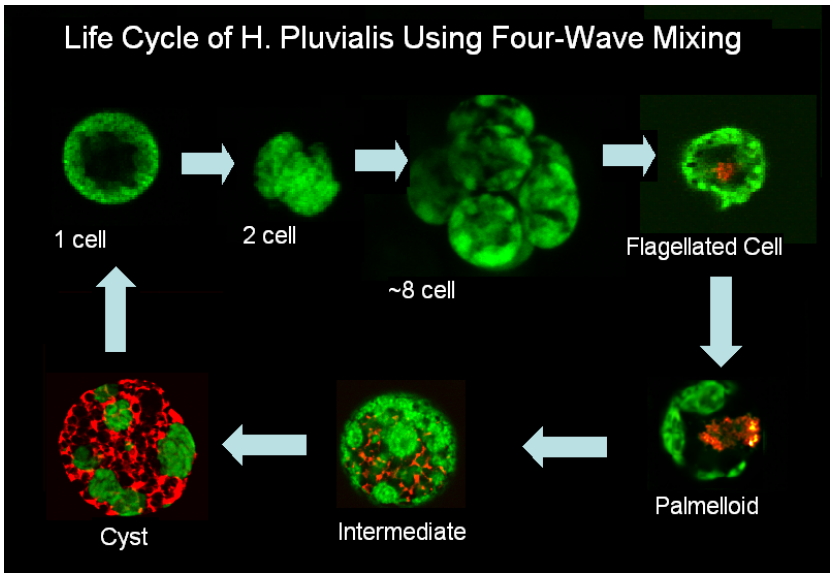

Figure 6.4: Composite images of the algal life-cycle with TPEF (green) and CARS (red). We can see the stages from cellular division to the flagellated algae, and the production of carotenoid as the encystment process proceeds.

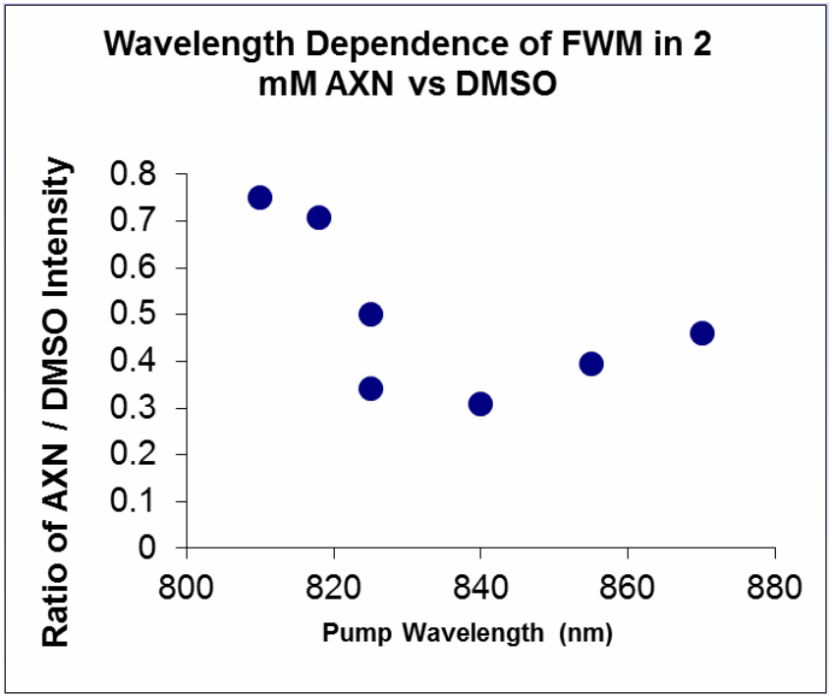

Figure 6.5: The intensity of the FWM response due to astaxanthin as compared to the intensity of the resonance of DMSO at 2850 cm^{-1}.

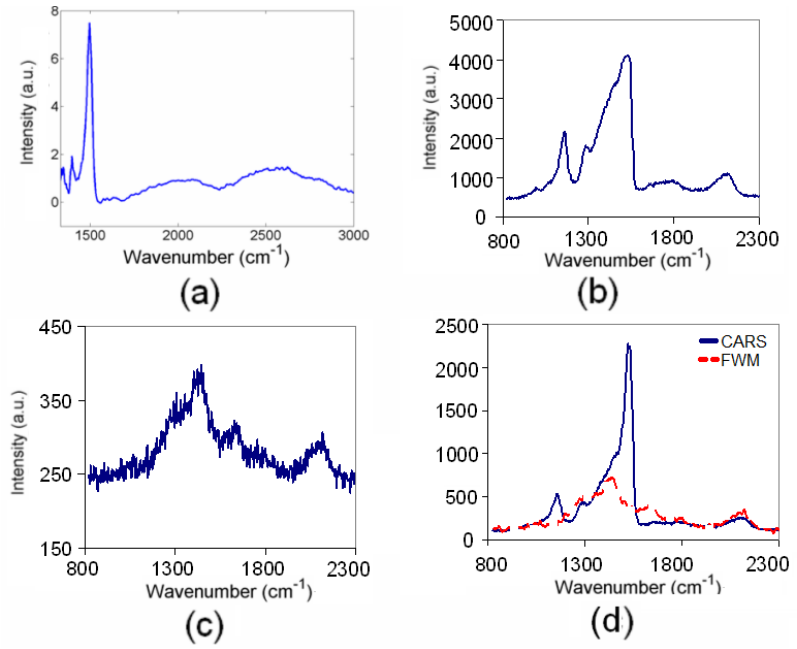

Figure 6.6: (a) The intensity of CARS and FWM at 860 nm in astaxanthin. The intensity has been scaled relative to the Stokes power measured by the OSA. (b) The CARS/FWM spectrum of astaxanthin at 915 nm. The 1520 cm^{-1} peak has been intentionally saturated on the detector in order to underscore the FWM intensity. (c) The NRB spectrum of pure canola oil under the same conditions as the spectrum of (b). (d) The unsaturated CARS spectrum of astaxanthin in canola at 915 nm is shown in blue. Overlaid in red is the simulated FWM spectrum based on the NRB due to the canola.

7 The Effective Conjugation Coordinate Model in CARS Microscopy

7.1 Introduction

In Chapters 5 and 6, we applied the techniques of CARS and FWM microscopy to the study of the molecule astaxanthin derived from the unicellular algae *haematococcus pluvialis*. These studies engendered several observations that were somewhat dischordant with conventional expectations regarding CARS and FWM, and these observations demand a more complete and thorough explanation. We summarize the key observations as follows: 1) Astaxanthin produces a CARS response that is anomalously large compared to typical CARS samples and calibration standards: of the order of 10^6 times that of pure lipids on a per molecule basis. 2) Astaxanthin produces a FWM response that is also anomalously large compared to typical NRB signals, dwarfing the response due to the solvent by many orders of magnitude, and even the response due to resonant CARS (e.g., lipids) by a similar factor of order 10^6. 3) Despite these two observations, we find that for the generated CARS spectrum in the fingerprint region, astaxanthin appears to be nearly background-free, and agrees extremely well with the spontaneous Raman spectrum of these molecules. 4) The excitation energies of the incident photons, and any relevant combination of these photons, are not capable of exciting the molecule to any known electronic resonance. Moreover, even if an electronic resonance enhancement were possible in this case, it is unclear why it would enhance both CARS and the FWM by a similar magnitude, when the energy levels associated with these processes are quite different. 5) Neither CARS nor FWM show a particularly strong wavelength dependence on the incident pump frequency. 6) The signal can be diminished either by photobleaching or by introduction of the compound $FeCl_3$ into the so-

lution. This is accompanied by a disappearance of the characteristic red colour of the astaxanthin.

We note that polyconjugated compounds, including carotenoids such as astaxanthin, display a number of unusual properties in their spontaneous Raman spectra as well. In particular, it has been observed that molecules of this nature display a characteristic Raman spectrum consisting only of a few, intense, well-defined bands, and that this holds for both small, simple molecules, as well as large molecules with hundreds of accessible normal modes [93]. Moreover, the positions of these bands are a function of the chain length, with a clear dispersion in the peak positions of the C=C and C-C stretch modes as a function of the chain length [125]. The characteristic Raman bands were observed to be very intense, and, interestingly, it was observed that these bands retained significant intensity even well outside the "pre-resonant" regime; excellent spectra could be recorded with Fourier-transform Raman spectroscopy using a 1064 nm pump, well below any electronic resonances [126]. Unfortunately, due to the difficulties involved in collection of spontaneous Raman spectra discussed in Chapter 5.2 and the references therein, a calibrated intensity dependence as a function of excitation wavelength has not been reported, to our knowledge. Nonetheless, the similiarities between this observation in spontaneous Raman and the relative wavelength independence of the CARS/FWM intensities of Figures 5.11 and 6.5 is extremely suggestive.

Several models have been developed to attempt to explain these phenomena. One of the most successful has been the Effective Conjugation Coordinate Model (ECCM). The ECCM was a model developed for the study of conjugated linear polyenes and carotenoids in order to explain these unusual properties of their spontaneous Raman spectra as well as to predict their nonlinear optical properties [93, 127, 128]. The ECCM hypothesizes that, in polyconjugated molecules,

the optical properties are primarily governed by a single dipole-allowed transition defined along a particular coordinate, called the Я coordinate, and all of the other possible normal modes are suppressed. This mode is associated with the driven collective motion of all of the electrons in the conjugated chain, which generates a significant enhancement in the polarizability through this coupled motion [129, 130, 131]. A consequence of this assumption is that the appearance of the Raman spectrum of the molecule is based entirely upon those modes that have an appreciable contribution along the Я coordinate. This is exactly equivalent to the situation in resonance Raman spectroscopy, where bands along a particular normal coordinate are selectively enhanced; the mathematical description of this collective motion is very similar to resonance Raman. Unlike resonance Raman, however, this collective motion can be excited at energies far below any electronic resonance in the molecule and, in fact, the ECCM operates in a static limit; no explicit dependence on the excitation laser frequency is necessary. Some authors have termed this effect to be a "pre-resonant" effect [132, 133, 134], but this seems somewhat of a misnomer as pre-resonance is normally used to describe an enhancement through a nearby electronic transition. Arguing that this is the case in the static limit seems somewhat misleading, and it perhaps makes more sense to discuss this in terms of an "intrinsic" resonance effect [135]. The ECCM has been very successful at predicting the Raman spectroscopic properties of linear polyenes, as well as carotenoids, including astaxanthin [136]. In addition, it can be used to calculate the nonlinear optical properties of these compounds [93]. In this Chapter, we will derive the essential equations of the ECCM as it applies to Raman and nonlinear optical processes, and use this with our experimental results to estimate the value of

the third-order molecular polarizability, γ, of astaxanthin.[3]

7.2 Calculating Raman Spectra from the ECCM

We begin with the general theory of calculating Raman spectra as proposed by Albrecht [137]. In this case, the intensity of scattered light by a Raman transition from state m to state n, I_{mn} will be emitted at frequency $\omega_0 - \omega_{mn}$, where ω_0 is the laser frequency and $\omega_{mn} = \omega_m - \omega_n$ is the vibrational transition frequency. The intensities will be related by the relation:

$$I_{mn} \propto I_0(\omega_0 - \omega_{mn})^4 \sum_{ab} |(\alpha_{ab})_{mn}|^2 \tag{7.1}$$

where we sum over the coordinate space a and b, and $(\alpha_{ab})_{mn}$ is the polarizability tensor of the molecule. In the most general case, for an arbitrary transition between the states m and n, the polarizability tensor, averaged over all rotational states, can be written as [137]

$$(\alpha_{ab})_{mn} = \frac{1}{\hbar} \sum_{j \neq m,n} \Big[\frac{\langle m| \hat{\mu}_a |j\rangle \langle j| \hat{\mu}_b |n\rangle}{\omega_{jn} - \omega_0 - i\Gamma_j} + \frac{\langle m| \hat{\mu}_b |j\rangle \langle j| \hat{\mu}_a |n\rangle}{\omega_{jn} + \omega_0 + i\Gamma_j} \Big] \tag{7.2}$$

where $\hat{\mu}$ is the dipole moment operator, ω_0 is the frequency of the Raman transition, Γ is the Raman linewidth, and we sum over states j in a transition from n to m. We apply a series of simplifying approximations to this general form. First, we adopt the Born-Oppenheimer approximation to separate the electronic and vibrational contributions. In this case, we are interested in a two-state model between the ground state to the first vibrationally excited state. Next, we expand the dipole operator $\hat{\mu}$ in a Taylor series expansion in the

[3]The quantity γ can be related to the third order polarizability by $\chi^{(3)} = \frac{1}{6} N_m L^4 \bar{\gamma}$, where N_m is the number density of molecules, L is the local field correction given by $L = (n^2+2)/3$ for linear refractive index n. In this Chapter we employ γ rather than $\chi^{(3)}$ since we are interested in per molecule rather than bulk properties.

vibrational coordinate Q.

$$\hat{\mu} = \mu(0) + \Big(\frac{\partial \mu}{\partial Q}\Big)\Big|_0 Q \tag{7.3}$$

Finally, we apply the effective conjugation coordinate approximation [127], restricting the coordinate space to only one single active normal mode. Under such approximations, Equation 7.2 may be recast in the form [138]

$$(\alpha_{ab})_Q = \frac{1}{\hbar}(\mu_a)_0^{ge}(\mu_b)_0^{eg}\Big(\frac{\partial E}{\partial Q}\Big)_0 \frac{1}{\omega - \omega_0 - i\Gamma} \tag{7.4}$$

Here, E is the potential energy surface of the excited state e. It has been well-established that the dominant vibrational motions in carotenoids are the stretching of the C=C and C–C bonds, respectively[139]. Thus we can assign the Я coordinate to the specific motion along this axis, with eigenvalues $L_{\text{Я}}$, and rewrite Equation 7.4 as:

$$(\alpha_{ab})_{\text{Я}} = \frac{1}{\hbar}(\mu_a)_0^{ge}(\mu_b)_0^{eg}\Big(\frac{\partial E}{\partial \text{Я}}\Big)_0 L_{\text{Я}} \frac{1}{\omega - \omega_0 - i\Gamma} \tag{7.5}$$

Equation 7.5 is a key result from the ECCM and bears some detailed analysis. The Equation consists of three factors. The first is a transition dipole factor, of the form $(\mu_a)_0^{ge}(\mu_b)_0^{eg}$. The matrix elements described in this factor give us information about the dipole coupling between the ground state and the first vibrationally excited state of the molecule. The third factor is a frequency factor, which is responsible for resonance enhancement through an electronic resonances ω with linewidths Γ and is generally small far from resonance. Figure 7.1 shows the near-resonant (514 nm) and off-resonant (785 nm) Raman spectra of AstaREAL. We note that both spectra display essentially the same characteristic structure in the fingerprint (900-1900 cm^{-1}) region, but the resonant case has overtone bands >1900 cm^{-1}. These bands are generally a sig-

nature of the resonance Raman effect [140, 141]. Within the fingerprint region, however, we observe comparable in the spectra of the two cases, despite the fact that the resonant Raman effect generally only selectively enhances particular bands–i.e., the resonance Raman spectrum often appears distorted compared to the off-resonant spectrum because not all Raman modes experience the same enhancement[137]. In our case, the Raman peaks of the two spectra are identical, because it is only along the Я coordinate that any enhancement can be produced. The enhancement is a result of the middle term, $\left(\frac{\partial E}{\partial Я}\right)_0 L_Я$, which characterize the electron-phonon coupling along the Я coordinate. When the coupling is sufficiently large, even off-resonant spectra can have significant Raman intensities.

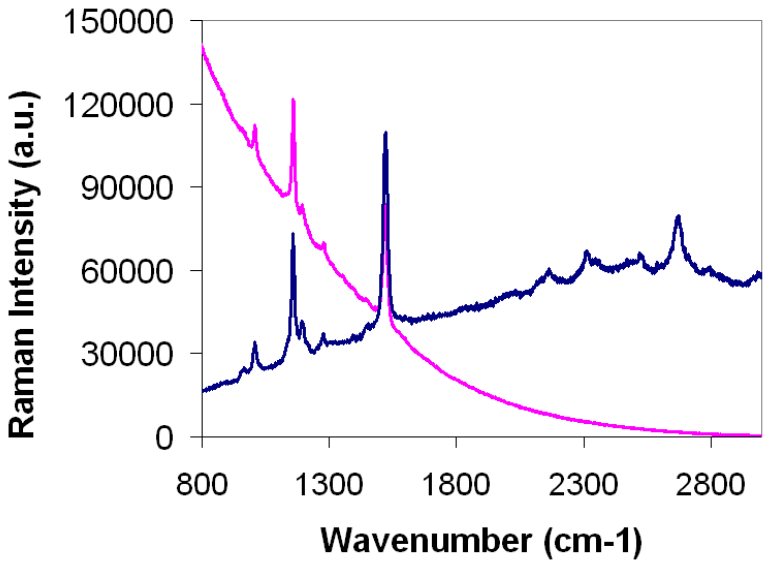

Figure 7.1: The spontaneous Raman spectrum of 45 mM astaxanthin taken at 514 nm, shown in blue, and 785 nm, shown in pink, with laser excitation powers of 95 and 360 μW, respectively. The 514 nm spectrum has been multiplied by 10 for easier viewing.

It is instructive to compare the relative intensities of the resonant and off-

resonant spectra in Figure 7.1. Direct comparison of the absolute intensities of Raman lines is challenging, as one must take into account the collection geometry and detector sensitivity as a function of frequency, refractive index changes, and absorption and re-absorption cross-sections of the solute [101]. To a very crude approximation, the relative strength of two Raman lines, R, scales as

$$R \propto \left(\frac{I_1}{I_2}\right)\left(\frac{\lambda_2}{\lambda_1}\right)^4\left(\frac{P_2}{P_1}\right)\left(\frac{\zeta(\lambda_1)}{\zeta(\lambda_2)}\right) \tag{7.6}$$

where I_1 and I_2 are the measured intensities of the Raman lines, λ_1 and λ_2, 557 nm and 891 nm, are the wavelengths of the Stokes light and P_1 and P_2 are the excitation laser powers, respectively. The function $\zeta(\lambda)$ represents the detector sensitivity at the wavelength of interest. The laser powers were 95 μW of 514 nm and 360 μW of 785 nm at the sample with identical exposure times. The integrated intensities of the peaks are of order 10^5 arb.u. for 514 nm and 10^6arb.u. for 785 nm. Assuming the detector sensitivity is nearly the same for both cases, then the intensity ratio of the 514/785 measurements at 1520 cm^{-1} is approximately 2.5:1. Under typical conditions, the resonance Raman effect should be in the order of 10^4 or 10^5 greater than that of the non-resonant contribution. In this case, we see that the near-resonance enhancement in astaxanthin does not result in an appreciably greater signal intensity in the 1520 cm^{-1} band. Nonetheless, both signals have considerable Raman intensity.

7.3 Calculating γ from the ECCM

We apply the results of the previous section to derive an expression for the second hyperpolarizability, γ, of astaxanthin in a semi-classical approximation. The second hyperpolarizability is a quantity that describes the per-molecule third-order polarizability due to an applied electric field. Naturally, this quan-

tity is proportional to the third-order susceptibility $\chi^{(3)}$ for a bulk medium. Specifically, the dipole moment μ_a can be expanded as follows

$$\mu_a = \mu_0 + \sum_b \alpha_{ab} E_b + \frac{1}{2} \sum_{bc} \beta_{abc} E_b E_c + \frac{1}{6} \sum_{bcd} \gamma_{abcd} E_b E_c E_d \qquad (7.7)$$

where α_{ab}, β_{abc}, and γ_{abcd} are the polarizability, hyperpolarizability, and second hyperpolarizability, respectively, the E terms represent the applied electric fields, and μ_0 represents the field-free dipole moment. For stronger fields, the term γ will be appreciable and becomes the primary contributor to nonlinear processes such as CARS and FWM. Suppose that the field creates an electric displacement along the coordinate Q, ΔQ from the equilibrium position Q_0 of the potential energy surface of μ. If we expand μ_a in a Taylor series expansion to first order, assuming a harmonic approximation, we have

$$\mu_a(Q_0 + \Delta Q) = \mu_a(Q_0) + \sum_b \Big(\frac{\partial \mu}{\partial Q_b}\Big)\Big|_{Q_0} \Delta Q \qquad (7.8)$$

$$= \mu_0(Q_0) + \sum_b \Big(\frac{\partial \mu_n}{\partial Q_b}\Big)\Big|_{Qo} \Delta Q_b$$

$$= \mu_0(Q_0) + \sum_b \alpha_{ab}(Q_0) E_b + \frac{1}{2} \sum_{bc} \beta_{abc} E_b E_c + \frac{1}{6} \sum_{bcd} \gamma_{abcd} E_b E_c E_d +$$

$$\sum_b \Big(\frac{\partial \mu_a}{\partial Q_b}\Big)\Big|_{Qo} \Delta Q_b + \sum_{bc} \Big(\frac{\partial \alpha_{ab}}{\partial Q_c}\Big)\Big|_{Qo} \Delta Q_c E_b +$$

$$\frac{1}{2} \sum_{bcd} \Big(\frac{\partial \beta_{abc}}{\partial Q_d}\Big)\Big|_{Qo} \Delta Q_d E_b E_c + \frac{1}{6} \sum_{bcde} \Big(\frac{\partial \gamma_{abcd}}{\partial Q_e}\Big)\Big|_{Qo} \Delta Q_e E_b E_c E_d$$

note that Equation 7.8 shows three different types of contributions to μ. There is the field-free contribution $\mu_0(Q)$; there is a contribution due to the polarizability α, the hyperpolarizability β and the second hyperpolarizability γ at Q_0; there are terms that depend on the gradient of the polarizabilities with respect to Q. We assign the α, β and γ terms in Equation 7.8 to α^e, β^e and γ^e, respec-

tively, and the $\frac{\partial\alpha}{\partial Q}$, $\frac{\partial\beta}{\partial Q}$, and $\frac{\partial\gamma}{\partial Q}$ terms to α^r, β^r and γ^r. These terms denote the electronic (superscript e) and relaxation, or Raman-associated, (superscript r) contributions to the dipole moment. The relaxation terms describe the contributions due to nuclear motions induced by the change in polarizability and are sensitive to the infrared, Raman, and hyper-Raman bands of the molecule. The terms $\left(\frac{\partial\beta}{\partial Q}\right)$ depend on the hyper-Raman intensities of the molecule, generally making them very difficult to measure experimentally. It has been argued in the literature that these terms can be neglected in calculation of γ for symmetric molecules with apolar end-groups such as astaxanthin [142]. Neglecting these terms, we can write γ^r, the relaxation component of the second hyperpolarizability, as follows [128]

$$\gamma^r_{abcd} = \frac{1}{c^2}\sum_e \frac{1}{\omega_e^2}\Big[\Big(\frac{\partial\alpha_{ab}}{\partial Q_e}\Big)\Big(\frac{\partial\alpha_{cd}}{\partial Q_e}\Big)+\Big(\frac{\partial\alpha_{ac}}{\partial Q_e}\Big)\Big(\frac{\partial\alpha_{bd}}{\partial Q_e}\Big)+\Big(\frac{\partial\alpha_{ad}}{\partial Q_e}\Big)\Big(\frac{\partial\alpha_{bc}}{\partial Q_e}\Big)\Big] \quad (7.9)$$

Note that the derivative components in Equation 7.9, $\left(\frac{\partial\alpha}{\partial Q}\right)$ can be related to the various components of Raman scattering polarizability tensor $(\alpha_{ab})_{mn}$. In classical Raman scattering, the intensity is given by the relation

$$I(\omega_s) = \frac{1}{32\pi^2\epsilon_0 c^3} N\omega_S^4 \Big|\frac{\partial\alpha}{\partial Q}\Big|^2 I_0 \quad (7.10)$$

where $\left|\frac{\partial\alpha}{\partial Q}\right|^2$ is the derivative of the polarizability with respect to Q, time-averaged and integrated over all orientations, and N is the number of scatters [39]. Comparing to Equation 7.1, it is clear that this derivative term is the classical equilavent of the quantum mechanical transition matrix $(\alpha_{ab})_{mn}$. Thus, in turn, we can relate γ^r directly to the intensities of the Raman modes of the molecule, which can be calculated from Equation 7.5, or measured experimentally. As noted in previously, these modes are anomalously large due to enhancement via the dipole and electron-phonon coupling terms in Equation

7.5, and that these intensities ought to be large even in the case where the pump frequency is far from an electronic resonance. For a specific Raman resonance of frequency $\omega_{Я}$ along the Я coordinate, the mean value of γ can thus be calculated as

$$< \gamma >^{Я} = \frac{1}{15c^2\omega_{Я}^2}(45\bar{\alpha} + 4\eta) \tag{7.11}$$

where $\bar{\alpha}$ and η are mean polarizability and anisotropy invariants from classical Raman scattering theory [39]. The peak at 1520 cm^{-1} is due to the symmetric C=C stretch, so, as a consequence of this symmetry, the polarizability tensor will be diagonal and hence $\eta = 0$ [39]. Using the 785 nm Raman scattering data from Figure 7.1, and Equations 7.9 and 7.11, we can estimate that the value of γ_r for astaxanthin is of order 10^{-33} esu.

7.4 Discussion

The ECCM provides a framework to determine the origin of the enhancement in astaxanthin both in CARS and in FWM. The intrinsic enhancement associated with electron-phonon coupling in the heavily restricted coordinate space of the molecule creates linear and nonlinear optical properties that are not typically seen in other molecular systems. This model has been the source of some controversy in the literature. In particular, it has been noted that this formalism explicitly excludes the effect of Herzberg-Teller coupling, which can potentially be a significant contribution to the polarizability tensor, especially off-resonance [143]. Moreover, since the ECCM is formulated in the static limit, it has been argued that it cannot properly describe optical effects [144]. Other alternative approaches, involving perturbative methods or *ab initio* calculations have been proposed as more appropriate models to describe this effect [129, 145]. In the former case, we note that the Herzberg-Teller coupling term is in fact present in

the ECCM formalism, so there is no reason in principle this cannot be accounted for. A very similar form of Equation 7.8 appears in the perturbative treatment, and the polarizability term $\left(\frac{\partial \beta}{\partial Q}\right)$ is associated with the Herzberg-Teller coupling [143]. One could explicitly account for this, then, by measuring the hyper-Raman spectrum of astaxanthin and calculating γ from the combined terms. In practice, hyper-Raman intensities are incredibly difficult to measure, so this is impractical to characterize experimentally. *Ab initio* calculations suggest, however, that the Raman term is the dominant term for symmetric molecules [142] and, to the level of approximation we are interested in, this appears to be sufficient. In terms of the issue of whether or not this model is sufficient for optical processes, we note that the model does not directly predict the CARS spectrum of astaxanthin and that, based on our experimental measurements, the CARS intensity of the 1520 cm^{-1} peak is nearly an order of magnitude greater than that of the FWM (and therefore γ for CARS is greater than FWM by a factor of about 3). It is clear, therefore, that the model as presented does not fully account for the details of the optical effects. The origin of the CARS spectrum is well-understood, as discussed in Chapter 2. Therefore, this is not a significant problem, and the intensity correction to the CARS response does not appreciably affect our analysis of astaxanthin. Given the relative simplicity of the model, and the predictive power it provides, we feel that adopting this model rather than more complex and conceptually challenging models is justified.

The anomalously large CARS response can be explained most adequately by comparing the relative values of γ (or $\chi_R^{(3)}$) between carotenoids and lipids. The polyconjugated carotenoid system has a significant electron-phonon coupling term that enhances γ^r to our measured value of $\sim 10^{-33}$ esu. Lipids, lacking this electron-phonon coupling term, have a per-molecule response that is several

orders of magnitude lower, in the order of 2×10^{-36} esu [146]. Recalling the squared dependence on γ in the CARS process, it is then quite reasonable that the observed CARS signals in astaxanthin are 10^6 or 10^7 times greater than that of pure lipids. Based on this model, it is similarly unsurprising that the observed response is independent of the pump wavelength: For both CARS and FWM, we are far from any allowed electronic resonance, so there is no reason to expect any significant changes in intensity. The signal is large exclusively because of the electron-phonon coupling term, which is independent of ω.

Applying this same argument to FWM is somewhat more subtle. In the case of CARS, it is quite reasonable to expect that its intensity will scale with γ^r; as FWM is an electronic process it is natural to assume that the intensity will scale with γ^e rather than γ^r. It has been found for a wide range of molecules that have a polyconjugated bond structure, however, that these quantities (as well as the hyperpolarizabilities β^r and β^e where applicable), are nearly identical in magnitude [147]. It has been argued that this is not mere coincidence, but rather that for an extended chain with only one active vibration mode, the same polarization state is achieved from either an electronic transition across the bandgap (i.e., a γ^e process), or via the vibrational excitation of the ground state (a γ^r process) [142]. As a result, the same factors that contribute to an enhancement in γ^r, namely the strong electron-phonon coupling, also produce a nearly identical enhancement in γ^e. We can see that this is the case empirically: based on our earlier estimate, we find that $\gamma^r \sim 10^{-33}$ esu and, based on measurements of nonresonant THG of astaxanthin from Ref [148], we find that $\gamma^e \sim 10^{-32}$ esu. Given the severity of some of the approximations in the previous sections, we feel that finding these two values within an order of magnitude is quite a reasonable correspondence. The fact that these values are of similar magnitude explains the strong observed FWM signals, as well as the relative

similarity in intensity between CARS and FWM. Both signals are enhanced by the same physical mechanism, the electron-phonon coupling of the polyconjugated bonds and, as a result, are enhanced by very nearly the same order of magnitude. Likewise both would share the property that they would be pump-wavelength independent far from resonance, consistent with our observations in Chapters 5.4 and 6.4. Moreover, since both processes are produced in the same molecules with essentially the same γ value, the relative strengths of their contributions to the observed signal will not change with concentration. Since the CARS signal is larger than the FWM, we see minimal spectral distortion and a quadratic concentration dependence; only when the CARS signal becomes small compared to the canola oil solvent do we begin to see linearization.

Since γ^r and γ^e induce the same polarization state in the molecule, the distinction between these quantities is somewhat artificial. As noted previously, these quantities refer to the nuclear and electronic motions of the molecule, respectively, and are treated separately. In fact, what we observe is that the electronic and nuclear motions of the molecule are highly coupled, suggesting a breakdown of the Born-Oppenheimer approximation. The fact that the electronic and nuclear motions are highly coupled leads to a remarkable implication: All nonlinear processes accessible to this molecule, including third-harmonic generation, CARS, FWM, degenerate four-wave mixing, etc. are all dependent on the Raman intensities of the same vibrational state, namely the vibrations along the Я coordinate, even though many of these processes do not have an obvious vibrational dependence. Thus, any nonlinear process with allowed transition dipole symmetries for this type of molecule will experience a similar enhancement.

We turn our attention to the issue of the astaxanthin radicals. As we discussed in Chapter 5.4, upon introduction of $FeCl_3$ to an astaxanthin solution,

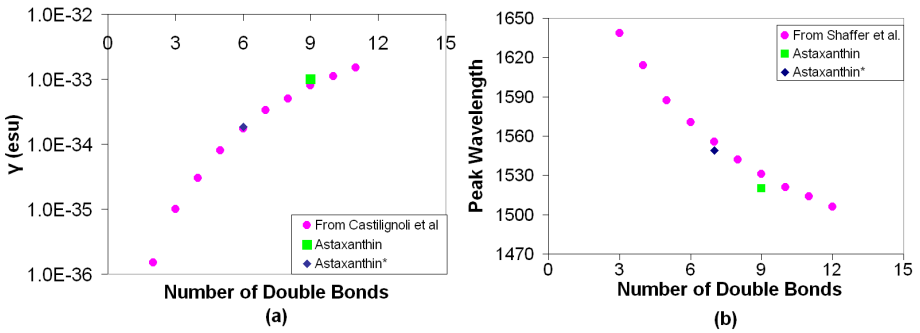

Figure 7.2: Chain length dependences of linear polyenes. For linear polyenes, γ depends superlinearly on the effective conjugation length of the chain. (a) The γ value of astaxanthin (green) compared to Ref [142] (pink). We estimate the chain length of the astaxanthin radical (blue diamond) based on its γ value. (b) Dispersion of polyene peak wavenumbers with chain length. We estimate the effective conjugation length of the radical astaxanthin by noting its spectral shift relative to neutral astaxanthin and compare to the measurements of Ref [125].

we observe a permanent and significant decrease in the CARS (as well as spontaneous Raman) intensity, as well as a notable shift in the positions of the Raman peaks. In Figure 7.2(a), we show the γ values of various polyenes as a function of the chain length, calculated from an *ab initio* analysis in Ref [142]. Our measurement of γ is 10^{-33} corresponds to a chain length of 9 in the linear chain,[4] which is in good agreement with the *ab initio* calculations. Since the signal drops by a factor of 25 upon introduction of the $FeCl_3$, γ for AXN* must be a factor of 5 smaller than astaxanthin. Based on the *ab initio* data, we find that this corresponds to an effective chain length of approximately 7. In Figure 7.2(b), we show the experimentally measured dispersion of the C=C stretching bond as a function of the number of double bonds. This is compared to Ref [125] and overlaid with our experimental values for astaxanthin and AXN*. In AXN*, this peak position is shifted from 1520 cm^{-1} to 1549 cm^{-1}, which is

[4] Although there are two double bonds in the ring structure of astaxanthin, it has been shown that double bonds in cyclic structures have minimal effect on the conjugation length [149]

consistent with of approximately 6 double bonds. Based on these results, then, we argue that the effect of radicalization is to shorten the effective conjugation length of the chain by 2-3 double bonds. As noted above, Herzberg-Teller coupling is not expected to be significiant in astaxanthin; however, in the radical, there is a strong possibility that the $\left(\frac{\partial \beta}{\partial Q}\right)$ term could be quite significant due to symmetry breaking. Since this term can be negative, it is possible that the effect of radicalization is the introduction of this coupling into the system, thereby reducing γ.

7.5 Conclusion

Based on the results of Chapters 5 and 6, we had identified several key observations that required explanation. In particular, we identified the significant intensities of the CARS and FWM responses, the background-free nature of the fingerprint response, the lack of resonance enhancement or wavelength dependence in signal, and the signal decrease in the radical. These effects can be adequately explained through the ECCM. The CARS and FWM intensities are a result of the enhancement due to the electron-phonon coupling term of Equation 7.5, rather than an electronic resonance enhancement. This enhancement is wavelength independent, as the ECCM operates in the static limit. Due to the strong coupling between the electronic and nuclear coordinates, the CARS and FWM cannot be treated as wholly separate processes with distinct γ^r and γ^e values; as a result, we do not observe any spectral distortions resulting from interference between them. Finally, the effect of the radicalization appears to be a shortening of the effective conjugation length of the molecule, which results in a reduced intensity and a shift from 1520 cm^{-1} to 1549 cm^{-1} in the C=C vibration mode.

8 Time-Correlated Single Photon Counting CARS Microscopy

8.1 Introduction

In the preceeding Chapters, we discussed the multimodal capabilities of our system–in particular, the ability to measure both the fluorescence and CARS responses of a sample in separate detectors, and to use these signals as indicators of different constituents in a physical system. This is most notable in the case of the algae *haematococcus pluvialis* studied in Chapters 5-7, where clear differentiation could be made between the CARS/FWM response associated with carotenoids, and the fluorescent response due to chlorophyll. Unfortunately, not all systems behave in a manner conducive to this type of analysis: In many cases, CARS and TPEF may be co-localized in both space and frequency, and a weak CARS signal may be lost within a stronger fluorescent background. Moreover, the fluorescent signal itself carries a wealth of information about the nature of the specimen that is lost entirely by simply integrating the signal over frequency and time in a PMT. For example, the probability of a particular molecule fluorescing depends on the radiative decay rate of the excited state of the molecule. By measuring the arrival time (at a detector) of individual photons relative to a very short excitation pulse, an emission time probability distribution function can be reconstructed from the fluorescence, characterizing the fluorescent lifetime. This method is known as time-correlated single photon counting (TCSPC).

TCSPC has been used since the late 60s, primarily as a method for determining the fluorescence lifetimes of organic compounds [150, 151]. It was established that the fluorescence lifetime was sensitive to the local environment of the molecular system [152, 153, 154] and therefore, lifetime itself could be used

as a contrast mechanism for imaging. This engendered the field of fluorescence lifetime imaging (FLIM) which has been immensely successful in molecular and cell biology, with applications including the imaging of cellular calcium channels [155], monitoring of variations in cellular pH [156], and distinguishing cancerous cells from healthy cells [157, 158]. One particularly fruitful application of FLIM has been to apply FLIM to systems involving Forster resonance energy transfer (FRET). FRET is a process that involves an energy transfer from one molecule (called the donor) to another (called the acceptor) with overlapping fluorescence emission and absorption spectra, via non-radiative dipole-dipole coupling. This process operates only on scales of a few nm in length and results in a change in both fluorescence intensity and lifetime at the interaction site [159]. As a result, FRET may be used for "super-resolution" (i.e. below the diffraction limit) measurements on the single molecule scale [160, 161, 162, 163].

In addition to lifetime, the emitted fluorescent light also has a spectrum. The emission spectrum is a function both of the molecule and of the interaction between the molecule and solvent. Shifts in the emission spectrum relative to the absorption (Stokes shifts) can therefore equally provide information on local dynamics and local chemistry within a sample [159]. The fluorescence spectrum can be collected simultaneously with the lifetime using a multi-channel detection system, where the fluorescent light is dispersed into several synchronized detectors, each monitor a different wavelength range. By combining both these time and frequency resolved techniques, TCSPC provides a powerful tool for the analysis of biological systems.

TCSPC also allows enhanced signal detection in CARS systems. There are two motivations for this development. The first is consideration of the noise characteristics between single-photon detection compared to standard PMTs. The signals in single photon counting are inherently digital; the detector either

records the presence of a single photon, or it does not. Therefore, the noise characteristics of the system depend primarily on the Poisson counting statistics of the arriving photons and are relatively insensitive to the detection electronics. In standard analog detection schemes, the signal-to-noise ratio depends on the photomultiplier and all subsequent electronics. The analog signal depends on the pulse height distribution of the detector, the noise spectra of any amplifiers, and the characteristics of the analog-to-digital acquisition card . Digital signals (i.e., TCSPC) are immune to these effects and therefore not only have better signal-to-noise, but also the analysis of their noise characteristics is generally much simpler [164]. Therefore, since the CARS process operates often in the low light limit, we can improve measurement sensitivity by moving from analog to digital detection. A second advantage is that many samples have both fluorescence and CARS responses. While our system is designed to spectrally filter a significant portion of the fluorescence in the forward direction through use of filters and alignment (i.e., the CARS channel is only collected in a relatively narrow solid angle in the forward direction), native fluorescence can be several orders of magnitude stronger than CARS. If the fluorescence emission is at same wavelength as the CARS signal, there is a significant possibility of cross-talk between the two channels. Using TCSPC, this cross-talk can be minimized since parametric nonlinear optical processes, including CARS, FWM, and SHG are essentially instantaneous on the electronic timescale, whereas fluorescence always has a characteristic lifetime, typically of a few ns. Therefore, the photons generated by instantaneous nonlinear optical processes will arrive entirely within the instrument response function (IRF) of the detector [165], which can be very short ($\sim$ 45 ps). Fluorescence lifetimes, on the other hand, are typically several ns, but possibly much longer. Hence, it is possible to time-gate the detected signal, further distinguishing the CARS response from fluorescence,

based on lifetime discrimination [165, 166]. For optimal contrast, it is necessary that the detector IRF be as short as possible, as the longer the IRF, the poorer the discrimination.

The combination of CARS with TCSPC, FLIM, or FRET has received little attention in the literature. This is likely due to the fact that there are several significant technological challenges that must be overcome in order to incorporate these modalities. Most notably, when the laser scans the sample, collection in the forward (non-descanned) direction results in small changes in the position of the beam on the detector face. While this is generally not significant for conventional large area PMTs, the area of the photocathode in high-fidelity TCSPC detectors may only be a few mm^2, meaning that as laser scanning occurs, the forward beam may miss the detector. The first TCSPC implementations of CARS, therefore, used epi-directed or back-reflected CARS rather than forward-directed CARS [165, 167]. Since the light path in the backward (descanned) direction is reversed, there will be no walk-off from the active area of the detector. Using this technique, it was demonstrated that fluorescence could be successfully distinguished from CARS using a 600 ps discrimination window and that epi-CARS and back-reflected CARS could be distinguished from each other by their respective path length–and therefore timing–differences [165]. Unfortunately, the magnitude of the CARS signal using either epi-CARS or back-reflected CARS is significantly diminished, greatly reducing the efficiency of this approach. A natural alternative, coupling the forward-directed light to an optical fibre, would allow the more intense forward-propagating light to be collected, but also presents other difficulties. As the lasers are x-y scanned over the sample, the forward-directed beam is spatially displaced. This changes the acceptance angle of the light into the detector, resulting in some loss of signal. However, at the conjugate plane of the condenser lens, this x-y spatial variation

is converted into an angular variation at a fixed spot. If a multi-mode optical fibre of the appropriate numerical aperture (NA) was located at this conjugate plane, it would therefore couple in all forward-directed light during the x-y scan. This allows collection of forward-directed light in a fibre [166]. Moreover, coupling to a low numercial aperture multi-mode optical fibre with different entrance angles will result in different optical paths of the light which depend on the entrance angles of the fibre, possibly leading to poorer TCSPC timing resolution [164]. In practice, it was found that collecting the light into a large-core (600 μm) optical fibre [166] located at the condenser conjugate plane led to modal dispersion that was within the overall IRF. This work demonstrated a forward-collected CARS time-gating of 300 ps, and successfully combined CARS with FLIM for the imaging of pollen and tissues. More recent work has demonstrated the application of combined CARS, FLIM and SHG system for clinical applications in tomography [168].

In this Chapter, building on the work of [166], we demonstrate the first wavelength resolved TCSPC combined with CARS to allow for simultaneous CARS, FLIM, and fluorescence spectroscopy imaging. We also demonstrate the effect of improved detector timing resolution on contrast in time-gated CARS experiments.

8.2 Theory of TCSPC

Fluorescence Lifetime

When a fluorophore absorbs a resonant photon, an electron is promoted from the ground state S_0 into an excited state, S_N. If S_N radiates, it has an associated spontaneous emission lifetime. However, there also exist non-radiative processes such as vibrational energy redistribution and internal conversion. If one of these occurs, then the photon ultimately radiated will have a lower frequency than

the absorbed photon, resulting in a Stokes shift. If the first excited state has an initial population of N_0 immediately after the laser pulse, then the population of the state at any future time is governed by first order kinetics, namely that

$$N(t) = N_0 e^{-\sum_p \Gamma_p t} \tag{8.1}$$

where each Γ_p represents the rate of a given decay pathway to some other state, both radiative and non-radiative. The fluorescence lifetime τ is thus defined as

$$\tau^{-1} = \sum_p \Gamma_p \tag{8.2}$$

Note that some molecules may have a multi-step pathway back to the ground state, and thus the decay would be multi-exponential. For organic fluorophores, the fluorescence lifetime is generally in the range of 1-10 ns.

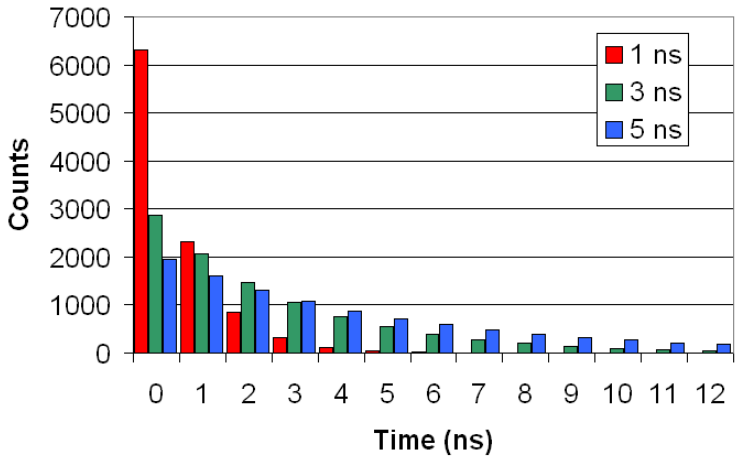

Figure 8.1: Simulated fluorescence lifetime histograms calculated from Equation 8.1 assuming a single decay pathway with lifetimes $\tau = 1$ ns (red), $\tau = 3$ ns (green) $\tau = 5$ ns (blue). The simulated histograms assume 10000 events have been collected.

Fluorescence is a stochastic process. It is thus impossible to determine the

fluorescence lifetime by considering only a single photon; rather, the arrival times of the photons may be determined by accumulation of a histogram of many events. Figure 8.1 shows the histograms of three fluorescent lifetimes, of 1 ns (red), 3 ns (green) and 5 ns (blue) in duration, binned in 1 ns steps, with 10000 total events in each distribution. The general shape of the lifetime distribution remains the same, but the distribution shifts and flattens as the lifetime lengthens. By fitting these histograms to an exponential function, the lifetime may be extracted. The error bars scale as $\sqrt{N_0}$; thus, signal-to-noise may be improved readily by accumulating more counts.

Forster Resonance Energy Transfer

Forster resonance energy transfer (FRET) is an excitation transfer process that shares many similarities to fluorescence and is a powerful tool for molecular imaging, in particular, super-resolution imaging. This is outlined schematically in Figure 8.2(a). One fluorophore, the donor, absorbs light, and populating the excited state S_1. Through short-range dipole-dipole coupling, it transfers energy to a neighbouring fluorophore, the acceptor, populating its slightly lower energy S_1 state. The acceptor then fluoresces, producing a very significant Stokes shift. The dipole-dipole coupling is a very short range interaction, where the efficiency E scales as follows:

$$E \propto \frac{1}{1 + (\frac{r}{R_0})^6} \tag{8.3}$$

where R_0 is called the Forster radius, whose value is typically of the order 1-10 nm [159] and r is the distance between the donor and acceptor. Due to the r^6 dependence and the very small value for R_0, FRET is exclusively a nano-scale interaction. The efficiency of the FRET is tied to the absorption and emission spectra of the donor-acceptor pair. Specifically, FRET is a result of the overlap

between the donor emission spectrum and the acceptor absorption spectrum, as shown in Figure 8.2(b).

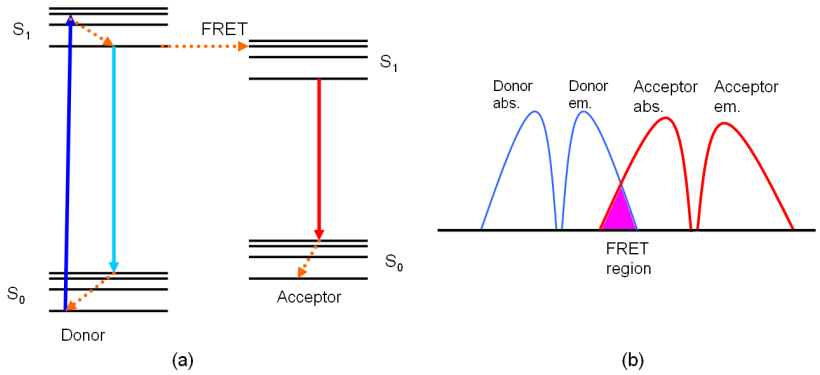

Figure 8.2: (a) Schematic of the energy level diagram of FRET. The donor is excited into the S_1 state (blue) the undergoes fluorescence (light blue) or non-radiatively transfers energy to the acceptor (orange), which undergoes a further Stokes shift (orange) and fluoresces (red). (b) The absorption and emission spectra of a FRET pair. The FRET process is governed by the overlap of the emission spectrum of the donor with the absorption spectrum of the acceptor (pink).

FRET is a subtle effect, but can be observed in several ways. First, there will be an enhancement in the fluorescence of the acceptor compared to in regions without FRET, and a corresponding reduction in fluorescence in the acceptor emission due to the non-radiative transfer. Second, as alluded to previously, local environmental effects result in changes to the fluorescence lifetime of molecules. By monitoring the fluorescence lifetime in regions containing the donor, acceptor, and the donor-acceptor pair, it also is possible to infer the action of FRET by a reduction in the lifetime of the donor.

8.3 Method and Materials

Multi-modal TCSPC Setup

The essential problem in TCSPC is the ability to accurately determine the arrival time of a detected photon compared with the timing of the laser pulse with a resolution generally on the order of 100 ps or less and in such a way that the system is able to clear its memory and detect subsequent photons at very high laser repetition rates (e.g. 80 MHz). This means that the system requires very fast, low noise, and high fidelity electronics. In Figure 8.3, we show a block diagram of the essential electronics in a TCSPC system [164]. The TCSPC module is synchronized to the laser source, which is used as a timing reference. The detector, typically an avalanche photodiode, microchannel plate or a single photon PMT, generates an electrical pulse for each photon that is collected. Avalanche detectors typically suffer from significant amplitude variation due to the pulse height distribution of the detectors. This pulse height distribution can introduce an undesirable timing jitter when using level discriminators to detect the arrival of the pulse. In order to achieve accurate timing, it is necessarily to employ a constant fraction discriminator (CFD), which transforms the pulse into, essentially, its first derivative. Timing is then based on the point of zero crossing, which to zeroth order is independent of the pulse amplitude. These signals are fed into a time-to-amplitude converter (TAC), which creates a voltage which depends linearly on the delay between the signal and reference–i.e. a "start-stop" technique. The voltage is then digitized by an analog-to-digital converter (ADC). The ADC specifies the upper limit to the number of timing bins available to the system, and, hence, its maximum timing resolution. In practice, this is not a significant limitation, as other noise sources introduce timing jitter that far exceed the resolution of the ADC. In our case, the time between pulses is 12.5 ns, (1/80 MHz) so in a 12-bit ADC, would give an ideal

resolution of 3 ps, far beyond the capabilities of even the fastest TCSPC systems or detectors. Given this, the ADC channels are often binned into 10 bits or even 8 bits without significant loss in timing resolution. Such electronics are available through several commercial providers. In our case, a SPC-150 system from Becker and Hickl GmbH was selected [169].

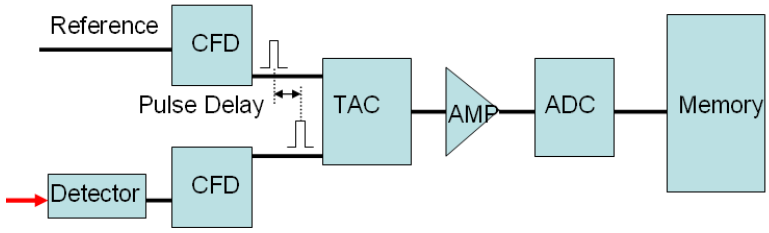

Figure 8.3: The basic architecture of a TCSPC system. The detected light is compared to a reference synchronization pulse generated from the laser source using two CFDs. This is converted into a timing pulse, digitized and stored in the computer memory to build up a histogram.

In our experiments, we used two different detectors. One is a high-fidelity single-channel detector, the R3809-U50 (Hamamatsu) [52], designed specifically for maximum timing resolution. This detector is a microchannel plate) PMT with excellent sensitivity from 300-800 nm, and an instrument response function of 45 ps. The timing stability comes at a cost, however, as microchannel plate PMTs are very sensitive to photodamage and cannot be run at particularly high ($<10^5$ Hz) count rates without risk of photodamage to the microchannel plate. Moreover, such detectors tend to have a higher dark count rate (10^3 Hz at room temperature), which generally necessititates a cooling apparatus to reduce the background. The second detection system used a PML-16-C detector (Becker and Hickl, GmbH) [170]. This detector provides up to 16 wavelength channels, each 12.5 nm wide, to create a time-and-frequency resolved TCSPC image. The timing resolution on this detector is poorer, 150-200 ps, but it has a lower dark

count rate at room temperature (10^2 Hz) and can be run at count rates as high as 5×10^6 Hz.

Our TCSPC system can be coupled to the microscope in either the forward or backwards direction and the signal is propagated to the detector using a large core fibre, following the implementation of Ref [166]. It should be noted that, in either case, single photon counting is a far more time-consuming process than our earlier implementations of CARS, owing primarily to these extra dimensions in both time and wavelength.

Detector Control

The detectors can be most easily managed through use of a software system called Single-Photon Counting Module (SPCM) created by Becker and Hickl. The detector power supplies are computer controlled by an applet that can specify the applied voltage (as a percentage of the maximum). In order to achieve high timing fidelity, the detectors operate ideally near 90% of the maximum gain, provided that the count rate does not exceed the threshold for potential damage, $\sim 10^5$ counts/s for the R3809-U50 and $\sim 10^7$ for the PML-16-C. The laser power may be adjusted accordingly to ensure optimal performance of the detection system. We highlight a few crucial features of the detection scheme here; the details of the detector setup are discussed in Appendix B.

FLIM can be done using the "Fifo imaging" mode in the SPCM software. The dimensionality of the image is defined in terms of the timing channels (via the ADC), spatial resolution and, in the case of the PML-16-C, frequency channels. Typical images are 256×256 pixels with 1024 timing channels. In order to do imaging with 16 wavelength channels, however, it is necessary to reduce the resolution of one of the other dimensions, as the system memory of the SPC-150 is insufficient to handle the data throughput otherwise. In our case, reducing the spatial resolution is difficult: The FlowView software that

controls the galvo scanning mirrors has a hard-coded minimum image size of 256×256, so running SPCM in 64×64 or smaller resolution will produce a highly distorted image. This means that it is not trivial to reduce the spatial resolution to gain additional wavelength channels. Instead we choose to bin ADC channels, reducing the timing resolution to 64 channels. Each channel in this case would have a timing bandwidth of ∼200 ps, which is of the order of the instrument response function of the detector, so this does not greatly impact the timing resolution of the detector.

Calibration of the PML-16-C

The PML-16-C detector splits the incoming light into up to 16 channels by use of a slit in front of the detector face. The corresponding wavelengths of the channels depends on their relative position to that of the slit. The dispersion is controlled by a micrometer screw attached to the side of the detector housing that moves the detector relative to the slit. It is thus necessary to calibrate the position of the screw relative to the different wavelength channels. In our case, this is done by simultaneously measuring the spectrum of an incandescent lamp using our spectrometer, with the intensities measured in each channel in the detector. By making very small changes to the micrometer ($< 0.05\mu$m steps), one can generate a reasonable estimate of when the emission line from the lamp is in the centre of the channel and thus create a relatively accurate calibration of the channel wavelengths. In Table 8.3, we show the wavelength calibrations for five different screw settings, 1.52 μm 2.00 μm, 2.53 μm, 2.70 μm, and 3.00 μm. These correspond to detection regimes in the UV/Vis, visible, Vis-NIR, and NIR regions, respectively. Each channel is 12.5 nm wide with the central wavelength as indicated. If the number of channels is reduced, these values must be binned; in single channel operation, the PML-16-C collects a 200 nm band.

Channel	λ at 1.52 μm	λ at 2.53 μm	λ at 2.85 μm	λ at 3.00 μm	λ at 3.41 μm
1	330	405	480	510	605
2	342.5	417.5	492.5	522.5	617.5
3	355	430	505	535	630
4	367.5	442.5	517.5	547.5	642.5
5	380	455	530	560	655
6	392.5	467.5	542.5	572.5	667.5
7	405	480	555	585	680
8	417.5	492.5	567.5	597.5	692.5
9	430	505	580	610	705
10	442.5	517.5	592.5	622.5	717.5
11	455	530	605	635	730
12	467.5	542.5	617.5	647.5	742.5
13	480	560	630	660	755
14	492.5	572.5	642.5	672.5	767.5
15	505	590	655	685	780
16	517.5	602.5	667.5	697.5	792.5

Table 8.1: Calibration of PML-16-C 16 Channel Detector. Channel maxima are quoted in nm. The uncertainty in the peaks of the channel maxima is of order ± 2 nm.

Measuring the Instrument Response Function

The IRF of the TCSPC system determines the timing resolution of our measurements. For FLIM-CARS applications, the IRF is particularly important as it determines the degree of discrimination available between the two modalities. Since parametric nonlinear optical processes such as CARS, SHG, SFG, etc. have a lifetime of effectively zero, we may use the signals generated from these processes to measure the IRF. In our cases, the CARS response from octadecene was used to find the IRF of the R3809-U50 and PML-16-C detectors, as shown in Figure 8.4. We measured their IRFs to be 44 ps and 208 ps, respectively. The design specifications indicate an IRF of 45 ps for the R3809-U50 and 150-200 ps per channel for the PML-16-C. The R3809-U50 IRF meets the design specifications, and the PML-16-C IRF is at the upper edge of the design specification.

Sample Preparation

Two common fluorophores were used to create various samples to test the TC-SPC system. Fluorescein (FCN) is a water-soluble dye that has an absorption peak at 400 nm, and a broad emission peaked at 520 nm, with a lifetime of 4.1 ns [171]. Nile Red (NLR) is a dye soluble in apolar solvents, with an excitation maximum at 445 nm in n-hexane and an emission peak at 524 nm, with a typical lifetime of 2.4 ns [172]. We created samples from a mixture of FCN in water and NLR in n-hexane to provide lifetime contrast by adding each dye to their respective solvents, then vigorously mixing the two to generate an emulsion.

A sample consisting of undiluted AstaREAL and FCN was created for combined FLIM and CARS experiments. In this state, AstaREAL is a thick, oily paste that is nearly insoluble in water. The astaxanthin in this compound agglomorates into many small deposits that produce an intense CARS response in the fingerprint, and FWM in the C-H region. AstaREAL has a weak fluorescent signal due to trace amounts of chlorophyll in the compound, but this fluorescence is many orders of magnitude lower in intensity than FCN. A small amount of this compound was thinly smeared onto a cover slide, which was coated by FCN in water and trapped by the cover slip. This produced a thin sample with a fluorescent background due to the FCN, interspersed with AstaREAL droplets.

Due to the strong fluorescence in FCN and the FWM response in AstaREAL, as well as concerns about photobleaching in both samples, laser powers of 30 mW pump, and, for FWM experiments, 18 mW of Stokes, were used for the PML-16-C detector. Due to the lower count rates required for the R3809-U50 detector, laser powers of 10-15 mW were more typical.

8.4 Applications of TCSPC

Fluorescence Lifetime Imaging

In Figure 8.5(a), we show an image of the interface between FCN and NLR using the R3809-U50 single channel detector. This image is the simplest level of detection available on the TCSPC system; it is an intensity image that reports the total number of photons accumulated in each channel. In Figure 8.5(b), the intensity image from Figure 8.5(a) has been converted into a lifetime image by fitting the fluorescence lifetime at each pixel. This image combines both intensity and lifetime information: The brightness is determined by the number of photons collected in a given pixel, whereas its lifetime is illustrated by its colour. In the inset, we show the distribution of lifetimes in Figure 8.5(b). There are two clear peaks in the lifetime histogram, corresponding to the two dyes. The lifetime of NLR is found to peak at $\sim$2.2 ns, and that of FCN is 3.4 ns.

The emission spectrum of pure FCN dye was measured using the PML-16-C with lifetime contrast, as shown in Figure 8.6. Despite the relatively poor frequency resolution of the PML-16-C, we see relatively good agreement between the measured FCN emission spectrum compared to the literature [171]. We find that the lifetime is relatively constant across all wavelength channels, with a value ranging from 3.3-3.5 ns.

In Figure 8.7, we show an example of FCN and NLR interface imaging using the PML-16-C detector. In this case, each frame represents an 12.5 nm wide wavelength channel, integrated along the time axis. The image hypercube was collected over a period of 30 minutes with a count rate of 4×10^5 counts/s. One can also integrate along the wavelength axis, and create a fluorescence lifetime image of the same data, as shown in Figure 8.8. One could also use this time-wavelength hypercube to generate a fluorescence lifetime image at each

wavelength, but this particular data set was too sparse for the lifetimes to have good statistics without spatial integration.

Time-Gated FWM with TCSPC

The effectiveness of the faster response time of the R3809-U50 detector compared to the PML-16-C were investigated using a combined lifetime and FWM setup. Using the sample made from AstaREAL deposits and fluorescein, a forward-directed image was created from the FWM and fluorescent responses of the two compounds. In Figure 8.9(a), we show an image of this sample using the PML-16-C detector, collected in single channel mode. As can be observed, there are small, dense deposits of AstaREAL present, dispersed in a fluorescent medium. The average background counts was found to be 190 counts. The signal had a maximum of 3000 counts, yielding a signal-to-noise ratio (SNR) of up to 16:1 for this image. The total number of counts is approximately 50 million counts. For the ADC resolution of 1024 timing channels, each channel had a width of approximately 12 ps, and thus 18 channels corresponded to the IRF of 208 ps. The image created by this timing window is shown in Figure 8.9(b). Significant background suppression is observed, with the background count rate falling by a factor of two to approximately 100 counts per pixel. The signal intensities similarly dropped by 100 counts, improving the SNR to 28:1 at maximum. For a hypothetical sample that produced exactly 1000 counts, the initial SNR would be about 5:1, which would improve to 9:1 following this time-gating.

For comparison, we attempted a similar experiment using the R3809-U50 detector using the same sample, but in a different position in the sample. Although the astaxanthin content in both fields is slightly different, both fields have the same background, the FCN solvent, so we can compare the relative improvements in signal-to-noise based on the proportion of background sub-

tracted. For an accurate comparison, approximately 50 million counts were collected. The count rate in this experiment was 2×10^4 counts/s, compared to 1×10^5 counts/s in the PML-16-C detector, so this required a factor of 5 longer to achieve the same number of counts. The generated image is shown in Figure 8.10(a). The mean background count rate is 148 counts, which is comparable to that of the PML-16-C detector. The maximum count rate was 2093, yielding a SNR of 14:1. With a time resolution of 12 ps, only four timing channels were necessary to fit the FWHM of the 44 ps IRF. The image created by this timing window is shown in Figure 8.10(b). The background count rate was reduced by over a factor of four to an average of 38 counts per pixel. As a result, the maximum SNR improved to more than 55:1. For a sample with exactly 1000 counts initially, we would expect an improvement of SNR from 7:1 to 26:1. We show the residual fluorescence in Figure 8.10(c). We observe that there is some residual signal from the astaxanthin droplets, which likely results from the choice to time-gate to the FWHM of the IRF. Using a larger time gate would likely capture more of the FWM signal, but also more of the fluorescence, likely resulting in a poorer overall signal-to-noise. We can validate this time-gating approach by constructing a fluorescence lifetime image as shown in Figure 8.10(d). The background fluorescence lifetime is >2 ns typically, whereas regions of significant FWM response have lifetimes of a few tens of picoseconds, consistent with the IRF approach. Note that regions of weaker FWM response have lifetimes that are derived from the convolution of the FWM response and the fluorescence lifetime, and thus reflect some intermediate value. While it should be stressed that these are not the true lifetimes, then, this can be used as a diagnostic for the relative weights of FWM and fluorescence in given parts of the sample.

8.5 Discussion

The R3809-U50 and PML-16-C detectors provide each provide distinct advantages and disadvantages for lifetime imaging. Figure 8.5 shows the simplest demonstration of the use of lifetime imaging in the R3809-U50, where two compounds can be easily distinguished by their fluorescence lifetime, and the specific values of the lifetimes can be calculated. We note that the fluorescence lifetime of NLR, 2.2 ns, was found to be in good agreement with the literature value of 2.4 ns [172] , but that of FCN, 3.4 ns, was found to be somewhat shorter than the expected lifetime of 4.1 ns [171]. Possible mechanism are due to concentration-dependent self-quenching in the fluorescein, or FRET in fluorescein, both of whichare known to shorten its lifetime [171]. From Figure 8.6, we note that the lifetime of fluorescein is essentially constant as a function of wavelength. This observation makes FRET an unlikely candidate for a significant reduction in lifetime, as FRET results in a decrease in lifetime of the donor [159]; as a consequence, we would anticipate that fluorescence emitted from the donors (shorter wavelengths) would have slightly longer lifetimes than that of the acceptors (longer wavelengths), which was not observed in this case. Therefore, we attribute the shorter lifetime primarily to self-quenching.

One major advantage to collecting lifetime simultaneously with CARS or FWM is the added degree of discrimination afforded by lifetime imaging. While CARS and FWM are undoubtedly less sensitive to background fluorescence than spontaneous Raman, background fluorescence can nonetheless present significant difficulties in CARS or FWM experiments, depending on the nature of the sample. For example, chlorophyll is highly fluorescent and happens to have an emission in the region of 670 nm; CARS experiments using a 815 nm pump and 1064 nm Stokes produce an anti-Stokes at 660 nm, contributing to significant cross-talk between the channels that cannot be easily separated using a

band-pass filter; however, as chlorophyll-a and -b have lifetimes of 5.1 ns and 3.9 ns, respectively [173], lifetime-gating provides a clear method to improve CARS contrast in a highly fluorescent medium [165]. We find that lifetime gating can lead to substantial gains in SNR. With a lifetime gating of 208 ps, we were able to reduce the background by nearly a factor of two using the PML-16-C for the 3.4 ns lifetime fluorescein, and with the improved time resolution of the R3809-U50, a factor of four in background reduction could be achieved. We note that discrimination generally improves with increasing fluorescence lifetime. The total fraction of background fluorescence rejected can be calculated from Equation 8.4,

$$R = 1 - \frac{\int_0^{\tau_{\mathrm{irf}}} e^{-\Gamma t} \mathrm{d}t}{\int_0^{12.5ns} e^{-\Gamma t} \mathrm{d}t} \tag{8.4}$$

where τ_{irf} is the instrument response function and we integrate between two pulses separated by 12.5 ns. In Figure 8.11, we plot Equation 8.4 as a function of the lifetime Γ out to 4 ns for our two detectors. As can be seen from the Figure, efficient background rejection requires an IRF that is considerably shorter than the fluorescence lifetime; even for relatively long-lived species, the performance of the PML-16-C is considerably worse than the R3809-U50. Indeed, if the PML-16-C were operating at its optimal performance of 150 ps IRF, there would already be a considerable improvement in background rejection. The experimental results for the PML-16-C agree well with theory, predicting a background rejection of approximately a factor of 2; for the R3809-U50, the background rejection was found to only be about a factor of 4, whereas theory predicts it should be closer to a factor of 6. This may be a statistical error, as the residual count rate of approximately 34 counts/pixel is at the noise floor of the system.

It is clear from this analysis that the R3809-U50 provides a significant advantage in terms of time-gated background rejection for CARS signals. However, this detector does suffer from some significant limitations. In particular, the R3809-U50 has a rather low damage threshold, requiring that count rates not exceed 10^5 Hz, compared to rates of $>10^6$ Hz available for the PML-16-C detector. This lower detection rate makes measurements considerably more time-consuming, presenting considerable difficulty for more unstable samples. Moreover, the R3809-U50 requires a large and expensive cooling apparatus to operate and, even cooled, still has a considerably higher rate of dark counts than the PML-16-C. For experiments run for the same length of time, rather than the same number of counts, the much lower signal rates of the R3809-U50 may not be sufficient to offset its improved timing resolution. Moreover, the PML-16-C has the added advantage of wavelength resolution. This advantage can manifest in two ways. First, on the issue of background rejection, the PML-16-C has the option to reject fluorescence on the basis of wavelength. The anti-Stokes bandwidth is only a few nanometers wide, and thus can likely fit into one, or at most two, wavelength channels. Thus the PML-16-C can be used effectively as a tunable bandpass filter for CARS with a width of as little as 12.5 nm, the width of the wavelength channels. This comes at the expense of timing resolution, but nonetheless filtering in this manner, provides another option for fluorescent background rejection. We note that, due to the differing count rates of the two systems, collecting sixteen channels of wavelength data on the PML-16-C would not require significantly longer than a single channel on the R3809-U50. On the other hand, the PML-16-C has poor sensitivity beyond 750 nm, and thus would be unsuitable for fingerprint-region CARS using NIR pulses.

We note that the increased sensitivity and added modalities provided by TCSPC comes at significant cost compared to conventional CARS experiments.

Using our standard PMTs and CARS detection scheme, we can generate hyperspectral CARS images in a matter of minutes and, at a single Raman shift, can monitor dynamic changes in real-time. By comparison, in our single-photon detection scheme, we sacrifice many of the advantages of CARS for additional information in fluorescence. In particular, TCSPC is much more time-consuming than the CARS setup from Chapter 3, to the point that collecting an image–at a single Raman shift–takes comparable, if not longer, time than collecting the entire CARS spectrum. This makes dynamic measurements virtually impossible and makes CARS spectra consisting of more than a handful of data points rather impractical. Thus the added benefits of improved signal-to-noise from the TCSPC system and the added imaging modality of lifetime imaging are partially offset by the loss of dexterity in CARS measurements.

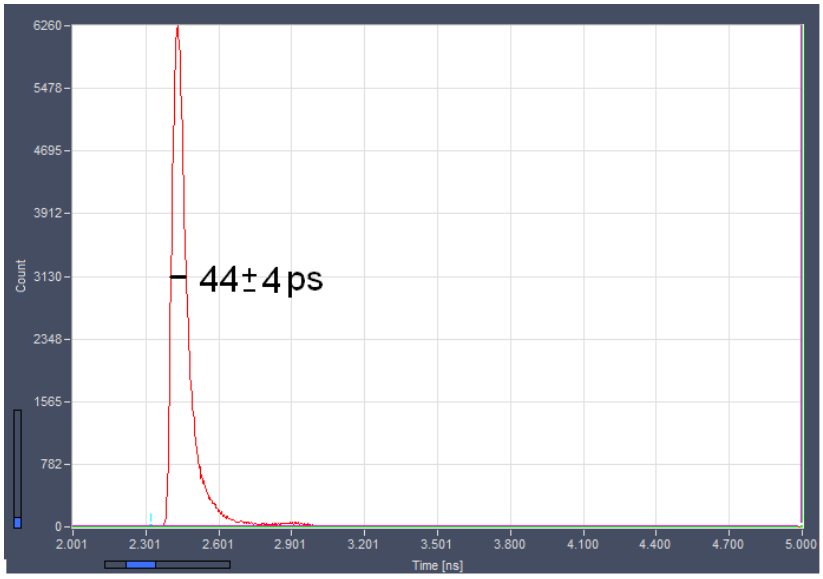

(a)

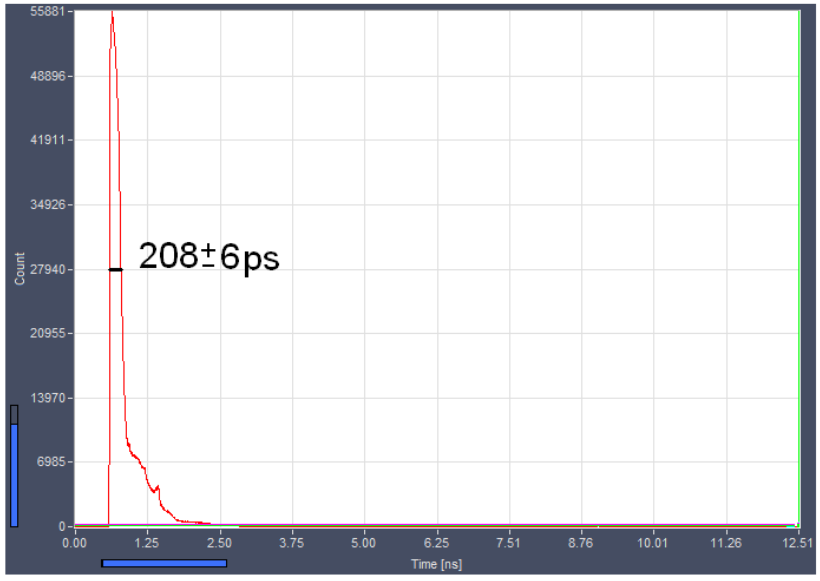

(b)

Figure 8.4: Instrument response functions of the (a) R3809-U50 and (b) PML-16-C detectors. The R3809-U50 has a measured IRF of 44 ps. The PML-16-C has an IRF of 208 ps.

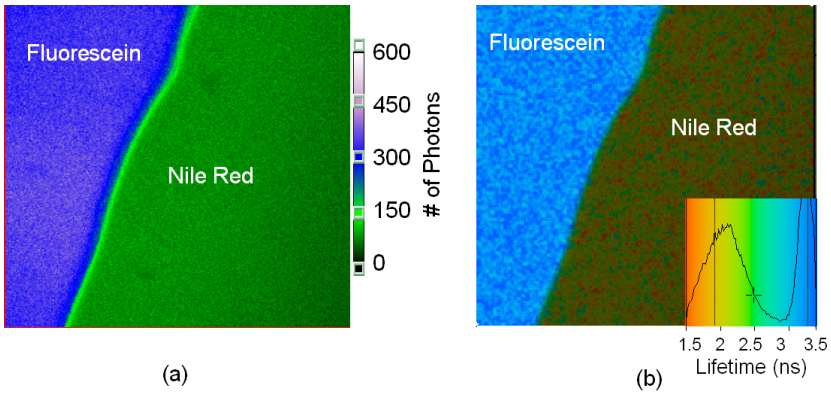

Figure 8.5: (a) Intensity image showing the number of photons collected at a FCN and NLR interface. (b) FLIM image of (a) calculated assuming each decay is a single-exponential. The lifetime of NLR is found to be distributed near 2.2 ns; FCN is found to be approximately 3.4 ns.

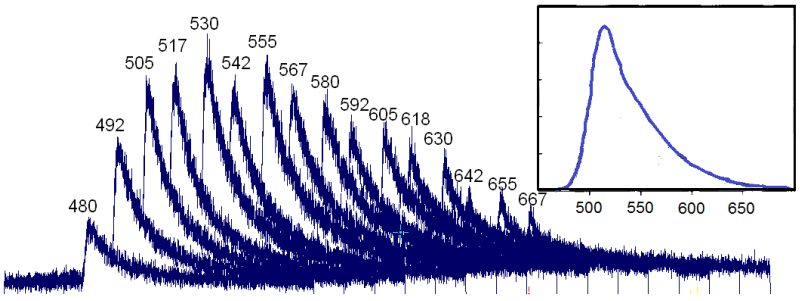

Figure 8.6: Emission spectrum of fluorescein measured using 16 wavelength channels. The fluorescein was measured at neutral pH with a two-photon excitation at 800 nm. The micrometre was set to 2.85 μm. The centre wavelength of each channel is indicated. Inset: Reference emission spectrum of fluorescein from [171].

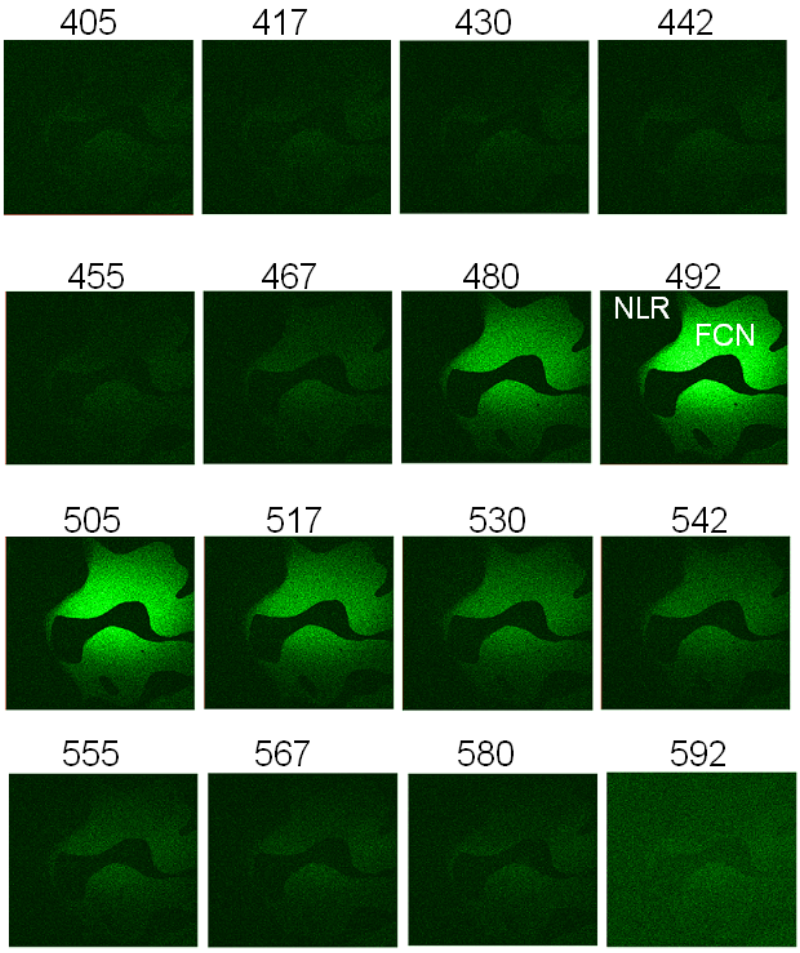

Figure 8.7: 16-channel wavelength imaging of FCN and NLR interface measured using the PML-16-C detector. Channel wavelengths for each image are noted in nm. The micrometre was set to 2.53 μm.

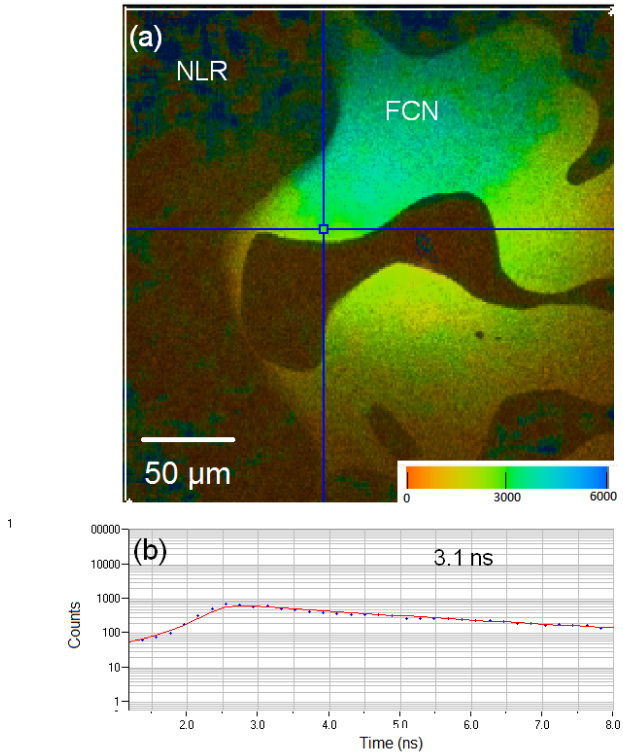

Figure 8.8: (a) Fluorescence lifetime image of Figure 8.7. (b) Measured fluorescence lifetime of the indicated point is 3.1 ns.

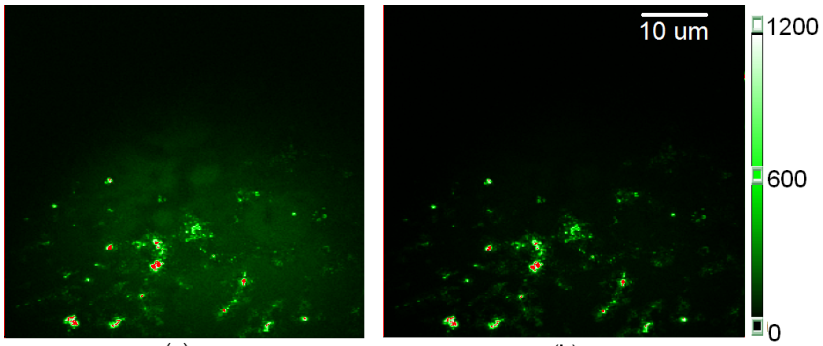

Figure 8.9: (a) Image of AstaREAL and FCN in water. AstaREAL droplets produce FWM around 650 nm and minimal fluorescence. The image has been integrated along the time axis to show the total signal. (b) Image of AstaREAL and FCN in water using only channels 86-104, which correspond to the 208 ps IRF of the PML-16-C. Small, extremely bright deposits have been saturated (red) in order to better display the remainder of the image.

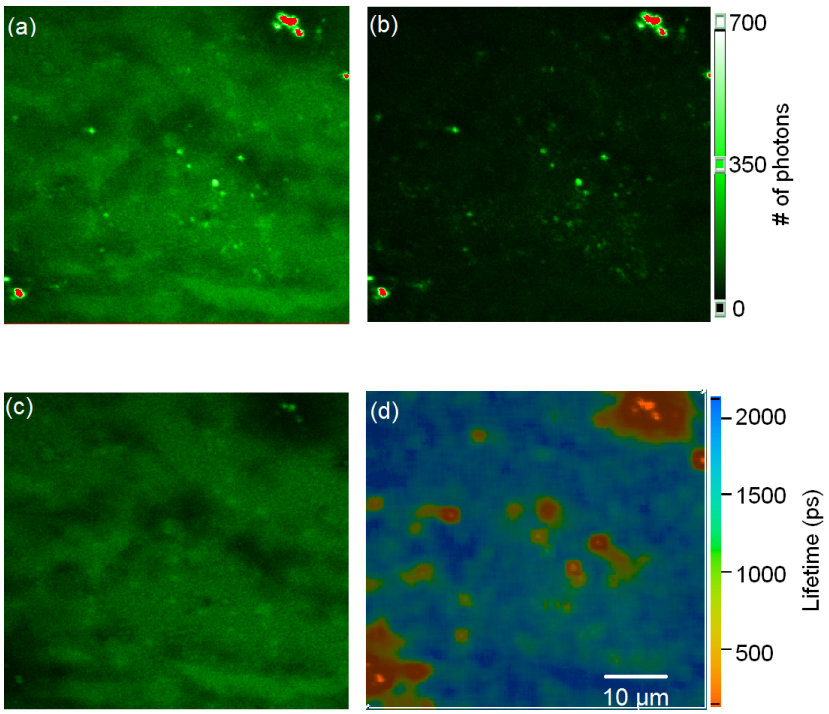

Figure 8.10: (a) Image of AstaREAL and FCN in water collected with the R3809-U50 detector, integrated along the time axis. (b) Time-gated image of AstaREAL and FCN in water using only channels 88-92, which correspond to the 45 ps IRF of the R3809-U50. Small, extremely bright deposits have been saturated (red) to better display the image. (c) Residual background from channels 92-1024. (d) FLIM image of (a). FWM signals have extremely short lifetimes, allowing us to differentiate between FWM and fluorescent responses.

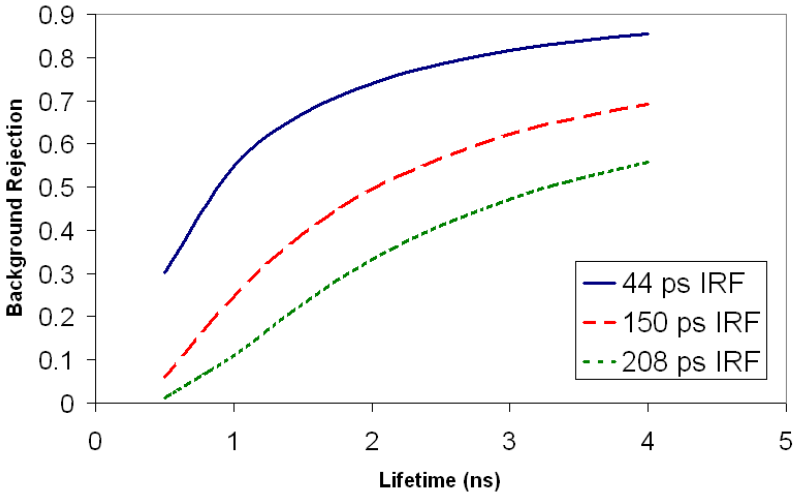

Figure 8.11: The fraction of fluorescence background rejected depends on the detector IRF and the sample lifetime. Rejection rates for the R3809-U50 (blue, solid), PML-16-C (green, dotted), and the PML-16-C using its optimal IRF (red, dashed) are plotted.

9 Conclusion

The goal of this thesis has been to demonstrate various advances in the field of CARS microscopy, specifically advances related to the formations of images and associated spectra, and how CARS images and spectra could be distorted or enhanced depending on the sample, the optical geometry or chirp matching conditions, or the presence of a highly fluorescent background.

Hyperspectral CARS imaging is a technically challenging technique both due the complexity of its implementation and to its coherent nature. In Chapter 3, we discussed various implementations of a CARS system, with specific focus on a chirp-matched implementation of CARS. While this technique has been available for longer than a decade, in this thesis we have shown that in many respects it is still poorly characterized, particularly in terms of calibrating the translation stage to the CARS frequency spectrum, the confounding effects of the non-uniform PCF output, and the determination of the optimal spectral resolution and chirp-matching conditions. We highlight in particular the non-uniform nature of the Stokes spectrum as a particular challenge, an issue that we have raised at various points in Chapters 3-6. This creates substantial complications for interpreting the intensities of CARS spectra. In Raman spectroscopy, the relative heights of the peaks in the spectrum can often be used as an indicator of various physical processes, such a relative saturation of lipids [174], but applying this analysis to CARS, even Raman-retrieved CARS, is fraught with difficulty as there is no guarantee that the intensities are not contaminated by the non-uniform behaviour of the Stokes spectrum. Moreover, as the Stokes spectrum varies slowly in time, it is possible to remove much of its influence by dividing the measured signal by an OSA-collected Stokes spectrum, but this measurement needs to be repeated frequently between scans to ensure high fidelity.

The coherent nature of the CARS process provides an added obstacle to interpretation of CARS experiments. It is well-established that CARS signals interfere with a simultaneously generated nonresonant background [12], and much of early CARS microscopy innovations have been attempts to remove or suppress the NRB [29, 30, 31]. Other researchers have argued for a transition from CARS to stimulated Raman scattering (SRS), a non-parametric coherent Raman scattering technique that provides similar spectral information to CARS, but is insensitive to the NRB [107, 175, 176]. In Chapter 4, we have shown that the coherent nature of CARS creates several more subtle effects apart from the well-established spectral distortions noted in the literature. In particular, we demonstrated the existence of a coupling between coherent spatial artefacts, notably shadows, that appear in CARS microscopy images and that these artefacts induce corresponding distortions in the spectrum due to the phase relations between the signal and the NRB. These distortions are driven primarily by the Gouy phase shift, as well as by changes in the linear refractive index between the object and the solvent, and cannot be easily accounted for in standard retrieval methods. Fortunately, these distortions are limited to samples whose signals are comparable to the NRB, and whose size is comparable to the Rayleigh length of the microscope focus. This seems to be an argument in favour of SRS, which does not produce imaging artefacts via the Gouy phase if the signal is modulated by frequency [177]. We stress that CARS researchers need to take extraordinary care when interpreting variations in spectra, as it is very easy to misinterpret the spatial-spectral coupling effect, the non-uniformity of Stokes spectrum, or a calibration error due to an inappropriate method, as a biological or chemical variation within the sample. We note that such subtle difficulties and limitations of the technique are rarely discussed in the literature and an important component of this thesis has been to carefully highlight these

various effects both in theory and in application, and to explain our results in the context of these challenges.

The other key theme in this thesis is the issue of spectral enhancements in CARS spectroscopy and nonlinear optical microscopy more broadly. The most common form of enhancement in optical systems is resonant enhancement. Resonant enhancement occurs when the energies of some combination of the participating photons in an optical process approach that of a real electronic or vibrational resonance in the material system. The CARS spectrum is generated by the interaction of the pump and Stokes on vibrational resonance in the molecular system. It is also possible to do double or even triple resonance enhanced CARS, where the pump or probe photons' energy approaches that of an electronic resonance [113]; however, this is often difficult to do in practice with NIR photons as they are typically below the energy of electronic resonances. Resonance enhancement, however, is not the only way to produce stronger signals in nonlinear optical systems. In Chapters 5-7, we discuss an unusual effect that appears in the carotenoid compound astaxanthin that generates extremely intense CARS signals. In Chapter 5, we have highlighted the extremely large CARS response of astaxanthin compared to samples generally known for their intense CARS response, namely lipids and diamond, and demonstrated conclusively that this enhancement cannot be due to an electronic resonance. Furthermore, we have provided numerous examples of how this enhancement can be exploited for *in vivo* studies of biological samples of substantial commercial interest. We argue that, while the bulk of CARS studies have focused on the study of lipids [22, 23, 24], polyconjugated molecules and carotenoids may be the ideal system for study using CARS microscopy due to their intrinsic enhancement effects. We further show that not only does astaxanthin produce extremely intense CARS signals, but that it also generates a substantial FWM

response. In Chapter 6, we demonstrate the first example of label-free FWM microscopy of a biological system. The fact that the FWM intensity is comparable to that of CARS means that it can be used as an imaging modality with subtly different properties that may be used advantageously by researchers. FWM does not interfere with the NRB, so it is much easier to interpret images and generate concentration studies. Moreover, since FWM does not have a spectral dependence, it can be achieved using an off-the-shelf laser system without the need for a chirp-matched apparatus. In Chapter 7, we demonstrated the subtle origin of this enhancement. Polyconjugated molecules such as astaxanthin are strongly coupled systems, such that the dominant contribution to their Raman spectrum (and, as it turns out, to the CARS and FWM responses) is due to a single vibrational mode along the Я coordinate. This, in turn, generates the identical conditions for resonance enhancement, even in the static limit. This enhancement engenders both a significant enhancement in the CARS signal, as well as an intrinsic coupling between the electronic and vibrational states of the molecule, resulting in a corresponding enhancement in FWM. While we have restricted our analysis to only to one type of molecule, polyconjugation is quite a general phenomenon and, therefore, there are many molecules that will experience similar enhancements that will be extremely amenable to CARS study, greatly expanding the field beyond its lipid-focused origin.

Finally, we turn our attention to the matter of fluorescence. While the NIR pulses used in CARS microscopy experiments, as well as the confocal microscope geometry, generally reduce the problems of fluorescent background contamination compared to spontaneous Raman, this is still a potential problem for weak CARS signals embedded in a highly fluorescent medium whose spectrum happens to overlap with the anti-Stokes colour of the CARS process. In such case, we cannot use colour to distinguish between the two processes and must turn to

some other mechanism. Fluorescence lifetime is one such contrast mechanism: Because of the physical processes that cause CARS and fluorescence, the photons generated by each process will have different delay times relative to the laser pulse. CARS is essentially instantaneous, whereas fluorescence depends on the emission lifetime. Consequently, using a TCSPC apparatus, the signals from CARS and fluorescence can be separated by time-gating [165, 166]. Lifetime also provides us with a further degree of freedom for imaging. The lifetime of a molecule is sensitive to the local environment and, therefore, lifetime itself may be used as a contrast mechanism. Changes in lifetime, including changes resulting from FRET, are sensitive to nano-scale changes in the local environment of the molecule. In effect, lifetime imaging has the potential to act as a fine "Vernier scale" for spatial localization within CARS images. In Chapter 8, we outlined an implementation of multi-channel TCSPC for use in CARS and FLIM experiments, and demonstrated the potential of time-and-frequency resolved fluorescence measurements as an extremely powerful extension to FLIM studies.

CARS hyperspectroscopy is a growing field that has a wide breadth of applications many fields, and researchers will increasingly encounter and be required to interpret CARS images and spectra. This thesis has outlined many varying challenges associated with CARS spectra, particularly relating to how distortions can be manifested, and how significant many of these effects can be. Interpretation of CARS spectra requires knowledge of the contribution due to the nonresonant background, as well as an understanding both of the instrument design and calibration, and the focal geometry, and, consequently, researchers must be exceptionally careful in drawing strong conclusions from CARS spectra, even those subject to Raman retrieval algorithms. On the other hand, enhancement of CARS spectra provides an opportunity for exceptionally high-quality

measurements to be undertaken, and many of the distortions associated with CARS may be overcome with sufficiently enhanced signals. Thus by taking into account the opportunities associated with CARS enhancements and the challenges associated with CARS distortions, future researchers will have a clear guide for how to approach CARS spectra in innumerable future applications.

Appendices

A Microscope Alignment

Optimization of the overlap of the pump and Stokes pulses in space, time, and polarization, and effective coupling into the detection system is a critical component of effective usage of the microscope system. For completeness' sake, we describe the standard alignment procedure used to optimize the CARS response in our system. First, the combined pump and Stokes beams are aligned separately making use of two pinholes, one located near the dichroic mirror and the other near the microscope output, identified as (1) and (2) on Figure A.1. For the Stokes light, especially if there has been a recent change in laser wavelength, it is generally preferably to commence course alignment using the 3-axis translation stage on the output of the fiber before using the actuating mirrors (4), (5). If fibre has been moved in the z direction on the 3-axis translation stage, the collimating lens (3) should be adjusted to optimize the spot size of the Stokes on a distant fluorescent card. Note that the pump spot size is much larger than the pinholes, so only coarse alignment using actuating mirrors (6) and (7) is necessary at this point.

Figure A.2 shows the alignment through the condensor. In order to maximize coupling into the fiber, it is sometimes necessary to align the condensor optics. This can be done in the following manner. First, the condensor (1) is removed, leaving the housing. The microscope objective (2) should be set in the position of best focus onto the sample holder. Upon closing the aperture on the side of the housing (3), an octagon should be visible in the eyepiece under illumination of the transmission lamp. The condensor height (4) may need to be adjusted slightly to achieve best focus. By adjusting the actuators on the condensor housing (5),(6), the octagon can be centred in the eyepiece. This indicates that

the condensor is properly aligned. Note that this stage is generally not necessary under most circumstances, as this alignment changes little day-to-day, but does require optimization on occasion.

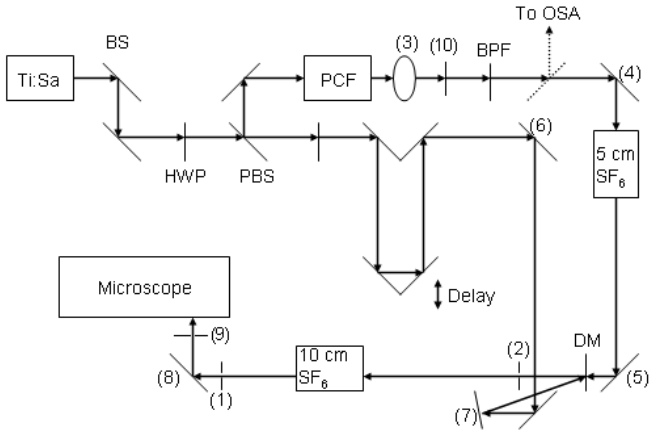

Figure A.1: The system should be aligned by using the numbered elements, in order. Elements that are not numbered should be considered static and not touched except under exceptional circumstances.

Once aligned through the compressor, a red fluorescent card can be used to optimize the alignment of the backward-generated fluorescence. This should be done in the following manner. First, the pump should be blocked, and the fluorescence PMT gain should be increased to the point where the Stokes light is visible on the detector. On an 8 bit color scale, 18 mW Stokes can typically be observed at around 800V on the PMT. The Stokes light should be centred using the final steering mirror (8) on Figure A.1 that directs the combined light into the microscope. The PMT gain should then be reduced (typically around 300V for a 100 mW pump with 8 bits on the color scale) and the pump light observed. This should be centred onto the detector using the pump actuating mirrors (6) and (7).

If the stage position where the pump and Stokes overlap in time, time-zero,

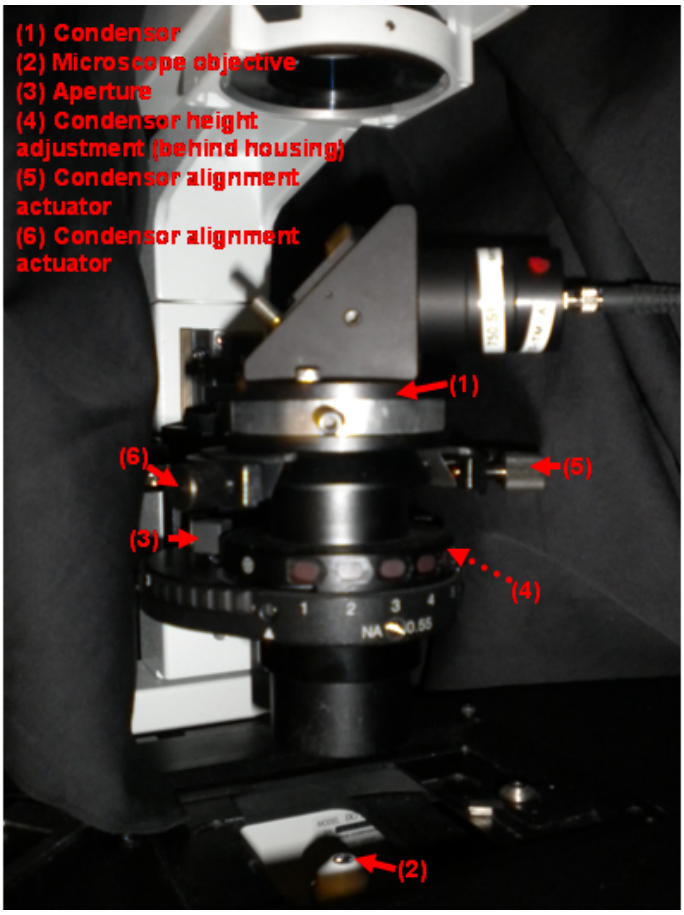

Figure A.2: The microscope condensor system.

is unknown, it is recommended that a sample of the compound astaxanthin be used first to optimize the signal. As discussed in Chapter 6, astaxanthin has a tremendously strong FWM response across all frequencies except for the specific region between 1000cm^{-1}–1600cm^{-1} where a resonant CARS response dominates. Since this produces a broadband response over virtually the entire Stokes bandwidth, this makes it extremely easy to optimize the pump and Stokes overlap before searching for time zero. Thus astaxanthin can be used as a calibration standard in any regime. If necessary, SFG from a KDP powder may

be used in this same manner to find the optimal overlap. Note that astaxanthin photobleaches at low powers. 40 mW pump and 20 mW Stokes powers are more than sufficient for alignment purposes, and even lower powers may be tolerated without difficulty.. The FWM signal from the astaxanthin should be optimized starting at the microscope and working backwards: First, the condensor height and microscope focus (X and Y on Figure A.2 should be chosen to maximize the signal intensity. Next, the final steering mirror (8) and pump actuators (6) and (7) can be tuned slightly to enhance contrast. Note that changes at this point should be minimal. Once a strong signal is seen in the CARS channel, a sample of ocadecene (nitrobenzene in the fingerprint) should be scanned. Ocadecene has an intense Raman resonance at 2861 cm^{-1} (1330 cm^{-1} for nitrobenzene) that is typical of lipids. At 140 mW pump and 20 mW Stokes, this resonance can be easily detected simply by scanning the translation stage across its travel. In practice, provided that the chirp has not changed, the peak positions should not move significantly between wavelength tuning, so this step may be unnecessary. Once the intense peak is located, the stage position of time-zero should be tuned to precisely match the maximum of the peak. Time zero for octadecene can typically be optimized to within ± 2 μm on the stage travel. The alignment process for the astaxanthin should now repeat, beginning with the condensor and focus (these should not change). In this case, the Stokes should be carefully walked using the actuating mirrors (4) and (5). Note that translating the Stokes light also affects the timing between pump and Stokes, so small adjustments to the delay may also be necessary. Finally, the polarization should be optimized. Optimal coupling requires the pump and Stokes to have the same polarization state; the microscope itself also appears to have a preferred polarization axis. The polarization of the microscope with respect to the pump is optimized when the input polarizer (9) is set to 340^o. The polarization of the Stokes output (10)

may then be adjusted to optimize the Stokes polarization with respect to the pump. Note that further signal can be gained by changing the Stokes spectrum, either through the input to the PCF polarization, or through the Stokes power. If only one specific resonance is required, then this procedure may be worthwile; however, increasing the power of the Stokes at one frequency may decrease it at others, so a compromise may be required if broad spectral scanning is required.

Table A summarizes the optimal parameters attainable for the microscope system using the method described above on the standard calibration samples of octadecene (C-H) and nitrobenzene (fingerprint). Note that even small changes in the PMT gain represent dramatic increases in signal intensity: As a general rule of thumb, an increase in gain of 50V represents approximately a factor of 2 increase in signal.

	815 nm Pump	915 nm Pump
Verdi Power (W)	8.49	8.5
Power at Mira output (mW)	970	620
Fibre coupling (%)	40	35
Stokes power at microscope (mW)	17	16
Pump power at microscope (mW)	144	116
Sample	Octadecene 2850 cm^{-1} peak	Nitrobenzene 1330 cm^{-1} peak
Saturation voltage of PMT with 255 colour scale on FlouView (V)	580	382

Table A1: System parameters for C-H and fingerprint CARS implementations.

B Configuring the TCSPC Module

The TCSPC module is controlled by the SPCM software by Becker and Hickl. This is an extremely versatile software that can be used for many applications ranging from FLIM to fluorescence correlation spectroscopy, to optical tomogra-

phy. Here, we only focus on the specific details required for setup of the TCSPC system for CARS and FLIM experiments. Other applications are discussed in extensive detail in the Becker and Hickl handbook [164].

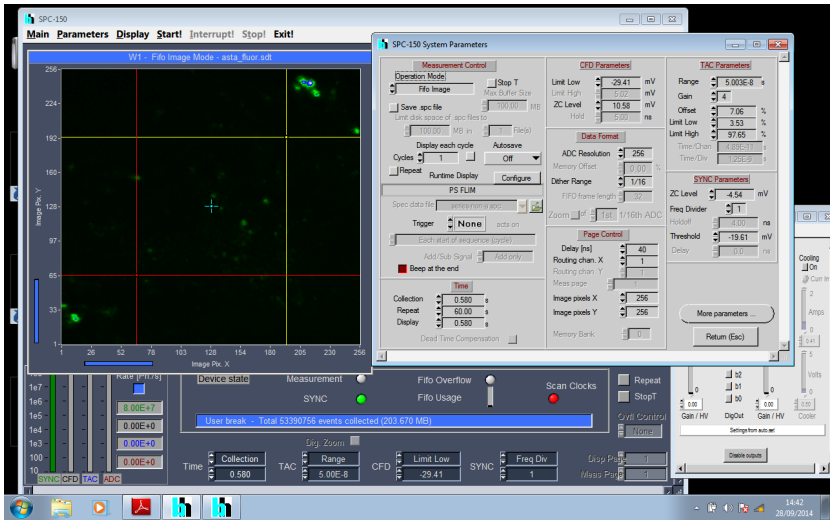

Figure B.1: Exemplar data taken from a sample of AstaREAL in fluorscein showing the TCSPC interface in SPCM with typical imaging parameters.

Figure B.1 shows a typical display in SPCM of an image taken with the PML-16-C detector. The main frame (top left) shows the image generated from a particular slice of the data hypercube: If 16 channel detection is used, then the image will correspond to the intensity (ie. number of photons collected) from single wavelength channel, and a certain number of binned timing channels. Generating lifetimes from this image requires further post-processing. The bottom left panel provides information on the synchronization pulse rate (80 MHz in our case), and the number of counts collected by the CFD, TAC, and ADC, the latter of which determines the count rate ultimately used to generate the image. The right-hand panel specifies the relevant system parameters.

The operation mode specifies what type of data will be collected. For imaging applications "Fifo image" is typically used. "Oscilloscope" mode is useful for

calibration purposes, as it integrates the entire image plane to produce a single lifetime. This can be used to ensure that the detector is collecting data properly. A notable timing error can occur if the lengths of the cables between the sync and CFD pulses are poorly matched. In this case, the lifetime will appear shifted and begin at some large time. In this case, additional cables must be added to either the CFD or the sync lines to delay the pulses relative to each other. When the pulses are well-matched, the lifetime curve will resemble Figure 8.6.

The CFD limit low parameter specifies the amplitude below which pulses will not be collected. Setting this parameter too high will lead to efficient counting; setting it too low will lead to high noise and poor timing resolution. Typical CFD low rates are -80mV for the PML-16-C and -29mW for the $\mathring{3}$.

The ADC resolution controls the number of timing channels available to the system. The ADC has 12 bits of data storage, allowing a maximum resolution of 4096 channels; however, binning may be necessary to improve performance or to account for the limitations of system memory. In practice, an ADC resolution of 1024 is sufficient for most purposes; for 16 channel detection, a maximum resolution of 64 bins is available due to constraints on the system memory.

The delay setting controls an internal delay between the routing and control signals. The delay should be set to maximize the ADC count rate. If the delay is too short, the ADC will become out of sync with the TAC and will not be able to collect any counts.

The routing X channel controls the number of wavelength bins available for the PML-16-C, up to a maximum of 16.

The image pixel counts should be chosen to match image size on FlowView. Note that FlowView uses a pixel clock and SPCM uses a line clock; as a result, a mismatch between the two will produce dramatic image distortions.

Other parameters may be left at their default values.

List of Publications

- A. M. Barlow, A. D. Slepkov, A. Ridsdale, P. J. McGinn, and A. Stolow, "Label-free hyperspectral nonlinear optical microscopy of the biofuel microalgae Haematococcus Pluvialis," *Biomedical Optics Express,* vol 5., pp 3391-3402, Sept. 2014

- A. D. Slepkov, A. M. Barlow, A. Ridsdale, P. J. McGinn, and A. Stolow, "In vivo hyperspectral CARS and FWM microscopy of carotenoid accumulation in H. Pluvialis," *Proc. SPIE 8937, Multimodal Biomedical Imaging IX,* 893707, Feb. 2014

- A. M. Barlow, K. Popov, M. Andreana, D. J. Moffatt, A. Ridsdale, A. D. Slepkov, J. L. Harden, L. Ramunno, and A. Stolow, "Spatial-spectral coupling in coherent anti-Stokes Raman scattering microscopy," *Optics Express,* vol. 21, pp 15298-15307, Jun. 2013

- A. M. Barlow, K. Popov, M. Andreana, D. J. Moffatt, A. Ridsdale, A. D. Slepkov, L. Ramunno, and A. Stolow, "Spatial-spectral coupling in hyperspectral CARS microscopy image formation," *Proc. SPIE 8589, Three-Dimensional and Multidimensional Microscopy: Image Acquisition and Processing XX,* 85890T, Feb. 2013

References

[1] L. F. Kourkoutis, J. M. Plitzko, and W. Baumeister, "Electron microscopy of biological materials at the nanometer scale," *Annual Review of Materials Research*, vol. 42, no. 1, pp. 33–58, 2012.

[2] A. R. Kherlopian, T. Song, Q. Duan, M. A. Neimark, M. J. Po, J. K. Gohagan, and A. F. Laine, "A review of imaging techniques for systems biology," *BMC Systems Biology*, vol. 2, p. 74, Aug. 2008. PMID: 18700030.

[3] S. A. Claridge, J. J. Schwartz, and P. S. Weiss, "Electrons, photons, and force: Quantitative single-molecule measurements from physics to biology," *ACS Nano*, vol. 5, pp. 693–729, Feb. 2011.

[4] P. A. Franken, A. E. Hill, C. W. Peters, and G. Weinreich, "Generation of optical harmonics," *Physical Review Letters*, vol. 7, pp. 118–119, Aug. 1961.

[5] R. W. Terhune, P. D. Maker, and C. M. Savage, "Optical harmonic generation in calcite," *Physical Review Letters*, vol. 8, pp. 404–406, May 1962.

[6] M. Bass, P. A. Franken, A. E. Hill, C. W. Peters, and G. Weinreich, "Optical mixing," *Physical Review Letters*, vol. 8, pp. 18–18, Jan. 1962.

[7] C. C. Wang and G. W. Racette, "Measurement of Parametric Gain Accompanying Optical Difference Frequency Generation," *Applied Physics Letters*, vol. 6, pp. 169–171, Apr. 1965.

[8] R. L. Carman, R. Y. Chiao, and P. L. Kelley, "Observation of degenerate stimulated four-photon interaction and four-wave parametric amplification," *Physical Review Letters*, vol. 17, pp. 1281–1283, Dec. 1966.

[9] P. D. Maker and R. W. Terhune, "Study of optical effects due to an induced polarization third order in the electric field strength," *Physical Review*, vol. 137, pp. A801–A818, Feb. 1965.

[10] R. W. Boyd, *Nonlinear Optics*. Acad. Press, 2003.

[11] C. V. Raman, "A new radiation," *Indian Journal of Physics*, vol. 2, pp. 387–398, 1928. Inaugural Address delivered to the South Indian Science Association on Friday, the 16th March 1928, at Bangalore.

[12] W. M. Tolles, J. W. Nibler, J. R. McDonald, and A. B. Harvey, "A review of the theory and application of coherent anti-stokes raman spectroscopy (CARS)," *Applied Spectroscopy*, vol. 31, pp. 253–271, July 1977.

[13] S. A. J. Druet and J.-P. E. Taran, "Cars spectroscopy," *Progress in Quantum Electronics*, vol. 7, no. 1, pp. 1–72, 1981.

[14] P. HuberWlchli and J. W. Nibler, "CARS spectroscopy of molecules in supersonic free jets," *The Journal of Chemical Physics*, vol. 76, pp. 273–284, Jan. 1982.

[15] W. Nitsch and W. Kiefer, "High resolution pulsed cars spectroscopy of the q-branches of some simple gases," *Optics Communications*, vol. 23, pp. 240–244, Nov. 1977.

[16] S. Roy, T. R. Meyer, R. P. Lucht, V. M. Belovich, E. Corporan, and J. R. Gord, "Temperature and CO2 concentration measurements in the exhaust stream of a liquid-fueled combustor using dual-pump coherent anti-stokes raman scattering (CARS) spectroscopy," *Combustion and Flame*, vol. 138, pp. 273–284, Aug. 2004.

[17] J. J. Valentini, D. P. Gerrity, D. L. Phillips, J.-C. Nieh, and K. D. Tabor, "CARS spectroscopy of o2(1g) from the hartley band photodissociation of o3: Dynamics of the dissociation," *The Journal of Chemical Physics*, vol. 86, pp. 6745–6756, June 1987.

[18] M. D. Duncan, J. Reintjes, and T. J. Manuccia, "Scanning coherent anti-stokes raman microscope," *Optics Letters*, vol. 7, pp. 350–352, Aug. 1982.

[19] A. Zumbusch, G. R. Holtom, and X. S. Xie, "Three-dimensional vibrational imaging by coherent anti-stokes raman scattering," *Physical Review Letters*, vol. 82, pp. 4142–4145, May 1999.

[20] E. O. Potma, W. P. de Boeij, and D. A. Wiersma, "Nonlinear coherent four-wave mixing in optical microscopy," *JOSA B*, vol. 17, no. 10, p. 16781684, 2000.

[21] J.-X. Cheng, A. Volkmer, and X. S. Xie, "Theoretical and experimental characterization of coherent anti-stokes raman scattering microscopy," *JOSA B*, vol. 19, no. 6, p. 13631375, 2002.

[22] C. L. Evans, E. O. Potma, M. Puoris'haag, D. Ct, C. P. Lin, and X. S. Xie, "Chemical imaging of tissue in vivo with video-rate coherent anti-stokes raman scattering microscopy," *Proceedings of the National Academy of Sciences of the United States of America*, vol. 102, pp. 16807–16812, Nov. 2005. PMID: 16263923.

[23] J.-X. Cheng and X. S. Xie, "Coherent anti-stokes raman scattering microscopy: instrumentation, theory, and applications," *The Journal of Physical Chemistry B*, vol. 108, pp. 827–840, Jan. 2004.

[24] C. L. Evans and X. S. Xie, "Coherent anti-stokes raman scattering microscopy: Chemical imaging for biology and medicine," *Annual Review of Analytical Chemistry*, vol. 1, no. 1, pp. 883–909, 2008.

[25] J.-X. Cheng, S. Pautot, D. A. Weitz, and X. S. Xie, "Ordering of water molecules between phospholipid bilayers visualized by coherent anti-stokes raman scattering microscopy," *Proceedings of the National Academy of Sciences*, vol. 100, pp. 9826–9830, Aug. 2003.

[26] M. Hashimoto, T. Araki, and S. Kawata, "Molecular vibration imaging in the fingerprint region by use of coherent anti-stokes raman scattering microscopy with a collinear configuration," *Optics Letters*, vol. 25, pp. 1768–1770, Dec. 2000. WOS:000165814600008.

[27] A. F. Pegoraro, A. D. Slepkov, A. Ridsdale, D. J. Moffatt, and A. Stolow, "Hyperspectral multimodal CARS microscopy in the fingerprint region," *Journal of biophotonics*, Dec. 2012. PMID: 23242840.

[28] K. I. Popov, A. F. Pegoraro, A. Stolow, and L. Ramunno, "Image formation in cars microscopy: effect of the gouy phase shift," *Opt. Express*, vol. 19, pp. 5902–5911, Mar 2011.

[29] D. L. Marks, C. Vinegoni, J. S. Bredfeldt, and S. A. Boppart, "Interferometric differentiation between resonant coherent anti-stokes raman scattering and nonresonant four-wave-mixing processes," *Applied Physics Letters*, vol. 85, pp. 5787–5789, Dec. 2004.

[30] J.-X. Cheng, L. D. Book, and X. S. Xie, "Polarization coherent anti-stokes raman scattering microscopy," *Optics Letters*, vol. 26, pp. 1341–1343, Sept. 2001.

[31] F. Ganikhanov, C. L. Evans, B. G. Saar, and X. S. Xie, "High-sensitivity vibrational imaging with frequency modulation coherent anti-stokes raman scattering (FM CARS) microscopy," *Optics Letters*, vol. 31, no. 12, p. 1872, 2006.

[32] E. M. Vartiainen, H. A. Rinia, M. Müller, and M. Bonn, "Direct extraction of raman line-shapes from congested cars spectra," *Opt. Express*, vol. 14, pp. 3622–3630, Apr 2006.

[33] Y. Liu, Y. J. Lee, and M. T. Cicerone, "Broadband CARS spectral phase retrieval using a time-domain KramersKronig transform," *Optics Letters*, vol. 34, p. 1363, Apr. 2009.

[34] E. O. Potma, X. S. Xie, A. Volkmer, and J.-X. Cheng, *Coherent Raman scattering microscopy*, ch. 2: Coherent Raman Scattering under Tightly Focused Conditions. Vol. 1 of Cheng and Xie [35], 2013.

[35] J.-X. Cheng and X. S. Xie, eds., *Coherent Raman scattering microscopy*, vol. 1. Boca Raton, FL: CRC Press, 2013.

[36] Muller, Squier, D. L. CA, and Brakenhoff, "CARS microscopy with folded BoxCARS phasematching," *Journal of microscopy*, vol. 197 (Pt 2), pp. 150–158, Feb. 2000. PMID: 10652008.

[37] E. O. Potma, W. P. de Boeij, and D. A. Wiersma, "Nonlinear coherent four-wave mixing in optical microscopy," *J. Opt. Soc. Am. B*, vol. 17, pp. 1678–1684, Oct 2000.

[38] J.-X. Cheng, A. Volkmer, and X. S. Xie, "Theoretical and experimental characterization of coherent anti-stokes raman scattering microscopy," *J. Opt. Soc. Am. B*, vol. 19, pp. 1363–1375, Jun 2002.

[39] D. A. Long, *The Raman effect: a unified treatment of the theory of Raman scattering by molecules.* Chichester; New York: Wiley, 2002.

[40] B. Pegoraro, A. Sussman. Private Communication.

[41] J.-x. Cheng, A. Volkmer, L. D. Book, and X. S. Xie, "An epi-detected coherent anti-stokes raman scattering (e-CARS) microscope with high spectral resolution and high sensitivity," *The Journal of Physical Chemistry B*, vol. 105, pp. 1277–1280, Feb. 2001.

[42] Y. Fu, H. Wang, R. Shi, and J.-X. Cheng, "Characterization of photodamage in coherent anti-stokes raman scattering microscopy," *Opt. Express*, vol. 14, no. 9, p. 39423951, 2006.

[43] T. Hellerer, A. M. K. Enejder, and A. Zumbusch, "Spectral focusing: High spectral resolution spectroscopy with broad-bandwidth laser pulses," *Applied Physics Letters*, vol. 85, pp. 25–27, July 2004.

[44] I. Rocha-Mendoza, W. Langbein, and P. Borri, "Coherent anti-stokes raman microspectroscopy using spectral focusing with glass dispersion," *Applied Physics Letters*, vol. 93, pp. 201103–201103–3, Nov. 2008.

[45] I. Pope, W. Langbein, P. Watson, and P. Borri, "Simultaneous hyperspectral differential-CARS, TPF and SHG microscopy with a single 5 fs ti:sa laser," *Optics Express*, vol. 21, p. 7096, Mar. 2013.

[46] A. F. Pegoraro, A. Ridsdale, D. J. Moffatt, Y. Jia, J. P. Pezacki, and A. Stolow, "Optimally chirped multimodal CARS microscopy based on a single ti:sapphireoscillator," *Optics Express*, vol. 17, pp. 2984–2996, Feb. 2009.

[47] A. F. Pegoraro, A. D. Slepkov, A. Ridsdale, D. J. Moffatt, and A. Stolow, "Hyperspectral multimodal cars microscopy in the fingerprint region," *Journal of Biophotonics*, vol. 7, no. 1-2, pp. 49–58, 2014.

[48] I. Coherent, "Operator's manual: The coherent mira900 laser,"

[49] "Verdi: Solid state green laser,"

[50] "Femtowhite cars: Supercontinuum device for coherent anti-stokes raman scattering,"

[51] "Confocal laser scanning biological microscopes: Fluoview fv300,"

[52] "Photomultiplier tubes: Basics and applications,"

[53] C. Romero, J. R. Vzquez de Aldana, C. Mndez, and L. Roso, "Non-collinear sum-frequency generation of femtosecond pulses in a micro-structured -BaB2O4 crystal," *Optics Express*, vol. 16, pp. 18109–18117, Oct. 2008.

[54] K. M. Hilligse, T. Andersen, H. Paulsen, C. Nielsen, K. Mlmer, S. Keiding, R. Kristiansen, K. Hansen, and J. Larsen, "Supercontinuum generation in a photonic crystal fiber with two zero dispersion wavelengths," *Optics Express*, vol. 12, pp. 1045–1054, Mar. 2004.

[55] J. M. Dudley, L. Provino, N. Grossard, H. Maillotte, R. S. Windeler, B. J. Eggleton, and S. Coen, "Supercontinuum generation in air?silica microstructured fibers with nanosecond and femtosecond pulse pumping," *Journal of the Optical Society of America B*, vol. 19, pp. 765–771, Apr. 2002.

[56] J. M. Dudley, G. Genty, and S. Coen, "Supercontinuum generation in photonic crystal fiber," *Reviews of Modern Physics*, vol. 78, pp. 1135–1184, Oct. 2006.

[57] G. Ghosh, "Sellmeier coefficients and dispersion of thermo-optic coefficients for some optical glasses," *Applied Optics*, vol. 36, pp. 1540–1546, Mar. 1997.

[58] L. Li, H. Wang, and J.-X. Cheng, "Quantitative coherent anti-stokes raman scattering imaging of lipid distribution in coexisting domains," *Biophysical Journal*, vol. 89, no. 5, pp. 3480 – 3490, 2005.

[59] G. W. H. Wurpel, J. M. Schins, and M. Müller, "Chemical specificity in three-dimensional imaging with multiplex coherent anti-stokes raman scattering microscopy," *Opt. Lett.*, vol. 27, pp. 1093–1095, Jul 2002.

[60] S. H. Parekh, Y. J. Lee, K. A. Aamer, and M. T. Cicerone, "Label-free cellular imaging by broadband coherent anti-stokes raman scattering microscopy," *Biophysical Journal*, vol. 99, no. 8, pp. 2695 – 2704, 2010.

[61] J. H. Hibben, "The raman spectra of water, aqueous solutions, and ice," *Journal of Chemical Physics*, pp. 172–177, 1937.

[62] C. C. Hatley and D. Callihan, "The effect of varying concentrations of certain electrolytes on the violet band of the raman spectra of water," *Phys. Rev.*, vol. 38, pp. 909–913, Sep 1931.

[63] W. G. Braun, D. F. Spooner, and M. R. Fenske, "Raman spectra. hydrocarbons and oxygenated compounds," *Analytical Chemistry*, vol. 22, no. 9, pp. 1074–1114, 1950.

[64] N. Djaker, D. Gachet, N. Sandeau, P.-F. Lenne, and H. Rigneault, "Refractive effects in coherent anti-stokes raman scattering microscopy," *Appl. Opt.*, vol. 45, pp. 7005–7011, Sep 2006.

[65] W. Demtröder, *Laser Spectroscopy: Basic Concepts and Instrumentation*, vol. 3 of *Advanced Texts in Physics*. Springer, 2002.

[66] C. Stephenson, W. C. Jr., and W. Wilcox, "The vibrational spectra and assignments of nitrobenzene, phenyl isocyanate, phenyl isothiocyanate, thionylaniline and anisole," *Spectrochimica Acta*, vol. 17, no. 9 - 10, pp. 933 – 946, 1961.

[67] A. Taflove and S. Hagness, *Computational Electrodynamics: The Finite-Difference Time-Domain Method*. Artech House Antennas and Propagation Library, Artech House, 2005.

[68] M. Fujii, M. Tahara, I. Sakagami, W. Freude, and P. Russer, "High-order fdtd and auxiliary differential equation formulation of optical pulse propagation in 2-d kerr and raman nonlinear dispersive media," *Quantum Electronics, IEEE Journal of*, vol. 40, pp. 175 – 182, feb. 2004.

[69] K. Yee, "Numerical solution of initial boundary value problems involving maxwell's equations in isotropic media," *Antennas and Propagation, IEEE Transactions on*, vol. 14, pp. 302 –307, may 1966.

[70] D. Vanderbilt and S. G. Louie, "A monte carlo simulated annealing approach to optimization over continuous variables," *Journal of Computational Physics*, vol. 56, no. 2, pp. 259 – 271, 1984.

[71] D. Gachet, F. Billard, N. Sandeau, and H. Rigneault, "Coherent anti-stokes raman scattering (cars) microscopy imaging atinterfaces: evidence of interference effects," *Opt. Express*, vol. 15, pp. 10408–10420, Aug 2007.

[72] R. Droop, *On the Ecology of Flagellates from Some Brackish and Fresh Water Rockpools of Finland*. Acta botanica Fennica, Soc. pro Fauna et Flora Fennica, 1953.

[73] M. R. Droop, "Conditions governing haematochrome formation and loss in the alga haematococcus pluvialis flotow," *Archiv fr Mikrobiologie*, vol. 20, pp. 391–397, Dec. 1954.

[74] M. Guerin, M. E. Huntley, and M. Olaizola, "Haematococcus astaxanthin: applications for human health and nutrition," *Trends in biotechnology*, vol. 21, pp. 210–216, May 2003. PMID: 12727382.

[75] K. Tominaga, N. Hongo, M. Karato, and E. Yamashita, "Cosmetic benefits of astaxanthin on humans subjects," *Acta Biochimica Polonica*, vol. 59, no. 1, 2012.

[76] J.-P. Yuan, J. Peng, K. Yin, and J.-H. Wang, "Potential health-promoting effects of astaxanthin: A high-value carotenoid mostly from microalgae," *Molecular Nutrition & Food Research*, vol. 55, no. 1, pp. 150–165, 2011.

[77] R. Lorenz and G. R. Cysewski, "Commercial potential for haematococcus microalgae as a natural source of astaxanthin," *Trends in Biotechnology*, vol. 18, no. 4, pp. 160 – 167, 2000.

[78] T. W. Goodwin and M. Jamikorn, "Studies in carotenogenesis. 11. carotenoid synthesis in the alga haematococcus pluvialis," *Biochemical Journal*, vol. 57, pp. 376–381, July 1954. PMID: 13181843 PMCID: PMC1269765.

[79] S. Boussiba, "Carotenogenesis in the green alga haematococcus pluvialis: Cellular physiology and stress response," *Physiologia Plantarum*, vol. 108, no. 2, p. 111117, 2000.

[80] M. C. Damiani, C. A. Popovich, D. Constenla, and P. I. Leonardi, "Lipid analysis in haematococcuspluvialis to assess its potential use as a biodiesel feedstock," *Bioresource technology*, vol. 101, pp. 3801–3807, June 2010. PMID: 20117928.

[81] M. Kobayashi, Y. Kurimura, T. Kakizono, N. Nishio, and Y. Tsuji, "Morphological changes in the life cycle of the green alga haematococcus pluvialis," *Journal of Fermentation and Bioengineering*, vol. 84, no. 1, pp. 94–97, 1997.

[82] M. Kobayashi, Y. Kurimura, and Y. Tsuji, "Light-independent, astaxanthin production by the green microalga haematococcus pluvialis under salt stress," *Biotechnology Letters*, vol. 19, no. 6, pp. 507–509, 1997.

[83] J. Fbregas, A. Otero, A. Maseda, and A. Domnguez, "Two-stage cultures for the production of astaxanthin from haematococcus pluvialis," *Journal of biotechnology*, vol. 89, pp. 65–71, July 2001. PMID: 11472800.

[84] A. M. Collins, H. D. T. Jones, D. Han, Q. Hu, T. E. Beechem, and J. A. Timlin, "Carotenoid distribution in living cells of haematococcus pluvialis (chlorophyceae)," *PLoS ONE*, vol. 6, p. e24302, Sept. 2011.

[85] M. Wayama, S. Ota, H. Matsuura, N. Nango, A. Hirata, and S. Kawano, "Three-dimensional ultrastructural study of oil and astaxanthin accumulation during encystment in the green alga haematococcus pluvialis," *PLoS ONE*, vol. 8, p. e53618, Jan. 2013.

[86] A. J. Young, "The photoprotective role of carotenoids in higher plants," *Physiologia Plantarum*, vol. 83, pp. 702–708, Dec. 1991.

[87] M. Kobayashi, T. Kakizono, N. Nishio, S. Nagai, Y. Kurimura, and Y. Tsuji, "Antioxidant role of astaxanthin in the green alga haematococcus pluvialis," *Applied Microbiology and Biotechnology*, vol. 48, no. 3, pp. 351–356, 1997.

[88] R. J. Cogdell, "Carotenoids in photosynthesis," *Philosophical Transactions of the Royal Society B: Biological Sciences*, vol. 284, pp. 569–579, Nov. 1978.

[89] C. Hagen, W. Braune, and F. Greulich, "Functional aspects of secondary carotenoids in haematococcus lacustris [girod] rostafinski (volvocales) IV. protection from photodynamic damage," *Journal of Photochemistry and Photobiology B: Biology*, vol. 20, pp. 153–160, Oct. 1993.

[90] Z. Pilt, S. Bernatov, J. Jeek, M. er, O. Samek, P. Zemnek, L. Nedbal, and M. Trtlek, "Raman microspectroscopy of algal lipid bodies: -carotene quantification," *Journal of Applied Phycology*, vol. 24, pp. 541–546, June 2012.

[91] A. Kaczor and M. Baranska, "Structural changes of carotenoid astaxanthin in a single algal cell monitored in situ by raman spectroscopy," *Analytical Chemistry*, vol. 83, pp. 7763–7770, Oct. 2011.

[92] A. Kaczor, K. Turnau, and M. Baranska, "In situ raman imaging of astaxanthin in a single microalgal cell," *The Analyst*, vol. 136, no. 6, p. 1109, 2011.

[93] C. Castiglioni, M. Del Zoppo, and G. Zerbi, "Vibrational raman spectroscopy of polyconjugated organic oligomers and polymers," *Journal of Raman Spectroscopy*, vol. 24, no. 8, p. 485494, 1993.

[94] T. G. Truscott, "New trends in photobiology: The photophysics and photochemistry of the carotenoids," *Journal of Photochemistry and Photobiology B: Biology*, vol. 6, pp. 359–371, Aug. 1990.

[95] C. Brackmann, A. Bengtsson, M. L. Alminger, U. Svanberg, and A. Enejder, "Visualization of β-carotene and starch granules in plant cells using CARS and SHG microscopy," *Journal of Raman Spectroscopy*, vol. 42, pp. 586–592, Apr. 2011.

[96]

[97] A. Dementjev and J. Kostkeviiene, "Applying the method of coherent anti-stokes raman microscopy for imaging of carotenoids in microalgae and cyanobacteria," *Journal of Raman Spectroscopy*, vol. 44, pp. 973–979, July 2013.

[98] X. N. He, J. Allen, P. N. Black, T. Baldacchini, X. Huang, H. Huang, L. Jiang, and Y. F. Lu, "Coherent anti-stokes raman scattering and spontaneous raman spectroscopy and microscopy of microalgae with nitrogen depletion," *Biomedical Optics Express*, vol. 3, pp. 2896–2906, Nov. 2012.

[99] Y. Koyama, M. Kuki, P. O. Andersson, and T. Gillbro, "Singlet excited states and the light-harvesting function of carotenoids in bacterial photosynthesis," *Photochemistry and Photobiology*, vol. 63, no. 3, p. 243256, 1996.

[100] H.-M. Chen and S. P. Meyers, "A rapid quantitative method for determination of astaxanthin pigment concentration in oil extracts," *Journal of the American Oil Chemists Society*, vol. 61, pp. 1045–1047, June 1984.

[101] F. Inagaki, M. Tasumi, and T. Miyazawa, "Excitation profile of the resonance raman effect of -carotene," *Journal of Molecular Spectroscopy*, vol. 50, no. 13, pp. 286 – 303, 1974.

[102] S. Amarie, U. Frster, N. Gildenhoff, A. Dreuw, and J. Wachtveitl, "Excited state dynamics of the astaxanthin radical cation," *Chemical Physics*, vol. 373, pp. 8–14, July 2010.

[103] L. Rimai, M. E. Heyde, and D. Gill, "Vibrational spectra of some carotenoids and related linear polyenes. raman spectroscopic study," *Journal of the American Chemical Society*, vol. 95, no. 14, p. 44934501, 1973.

[104] P. J. Carroll and L. E. Brus, "Saturation and nonlinear electromagnetic field effects in the picosecond resonance raman spectra of carotene," *The Journal of Chemical Physics*, vol. 86, pp. 6584–6590, June 1987.

[105] B. Wang, A. Zarka, A. Trebst, and S. Boussiba, "Astaxanthin accumulation in haematococcus pluvialis (chlorophyceae) as an active photoprotective process under high irradiance1," *Journal of Phycology*, vol. 39, no. 6, pp. 1116–1124, 2003.

[106] D. Krishnamurti, "The raman spectrum of diamond," *Proceedings of the Indian Academy of Sciences - Section A*, vol. 40, pp. 211–216, Nov. 1954.

[107] C. W. Freudiger, W. Min, B. G. Saar, S. Lu, G. R. Holtom, C. He, J. C. Tsai, J. X. Kang, and X. S. Xie, "Label-free biomedical imaging with high sensitivity by stimulated raman scattering microscopy," *Science*, vol. 322, pp. 1857–1861, Dec. 2008. WOS:000261799400059.

[108] H. A. Rinia, K. N. Burger, M. Bonn, and M. Mller, "Quantitative label-free imaging of lipid composition and packing of individual cellular lipid droplets using multiplex {CARS} microscopy," *Biophysical Journal*, vol. 95, no. 10, pp. 4908 – 4914, 2008.

[109] J. P. R. Day, K. F. Domke, G. Rago, H. Kano, H.-o. Hamaguchi, E. M. Vartiainen, and M. Bonn, "Quantitative coherent anti-stokes raman scattering (cars) microscopy," *The Journal of Physical Chemistry B*, vol. 115, no. 24, pp. 7713–7725, 2011.

[110] S. A. J. Druet, B. Attal, T. K. Gustafson, and J. P. Taran, "Electronic resonance enhancement of coherent anti-stokes raman scattering," *Phys. Rev. A*, vol. 18, pp. 1529–1557, Oct 1978.

[111] B. Attal-Trtout, P. Berlemont, and J. Taran, "Three-colour cars spectroscopy of the oh radical at triple resonance," *Molecular Physics*, vol. 70, no. 1, pp. 1–51, 1990.

[112] B. Attal, M. Pealat, and J.-P. Taran, "CARS diagnostics of combustion," *Journal of Energy*, vol. 4, no. 3, pp. 135–141, 1980.

[113] W. Min, S. Lu, G. R. Holtom, and X. S. Xie, "Triple-resonance coherent anti-stokes raman scattering microspectroscopy," *ChemPhysChem*, vol. 10, pp. 344–347, Feb. 2009.

[114] M. Fuciman, M. Durchan, V. louf, G. Kean, and T. Polvka, "Excited-state dynamics of astaxanthin aggregates," *Chemical Physics Letters*, vol. 568-569, pp. 21–25, May 2013.

[115] B. Demmig-Adams and W. W. Adams, "Antioxidants in photosynthesis and human nutrition," *Science*, vol. 298, pp. 2149–2153, Dec. 2002. PMID: 12481128.

[116] N. E. Holt, D. Zigmantas, L. Valkunas, X.-P. Li, K. K. Niyogi, and G. R. Fleming, "Carotenoid cation formation and the regulation of photosynthetic light harvesting," *Science*, vol. 307, pp. 433–436, Jan. 2005. PMID: 15662017.

[117] S. Amarie, K. Arefe, J. H. Starcke, A. Dreuw, and J. Wachtveitl, "Identification of an additional low-lying excited state of carotenoid radical cations," *The Journal of Physical Chemistry B*, vol. 112, pp. 14011–14017, Nov. 2008.

[118] J. Renger, R. Quidant, N. van Hulst, and L. Novotny, "Surface-enhanced nonlinear four-wave mixing," *Physical Review Letters*, vol. 104, p. 046803, Jan. 2010.

[119] Y. Wang, C.-Y. Lin, A. Nikolaenko, V. Raghunathan, and E. O. Potma, "Four-wave mixing microscopy of nanostructures," *Advances in Optics and Photonics*, vol. 3, p. 1, Sept. 2010.

[120] M. Danckwerts and L. Novotny, "Optical frequency mixing at coupled gold nanoparticles," *Physical Review Letters*, vol. 98, p. 026104, Jan. 2007.

[121] L. Huang and J.-X. Cheng, "Nonlinear optical microscopy of single nanostructures," *Annual Review of Materials Research*, vol. 43, no. 1, pp. 213–236, 2013.

[122] F. Masia, W. Langbein, P. Watson, and P. Borri, "Resonant four-wave mixing of gold nanoparticles for three-dimensional cell microscopy," *Optics Letters*, vol. 34, pp. 1816–1818, June 2009.

[123] P. Mahou, N. Olivier, G. Labroille, L. Duloquin, J.-M. Sintes, N. Peyrieras, R. Legouis, D. Debarre, and E. Beaurepaire, "Combined third-harmonic generation and four-wave mixing microscopy of tissues and embryos," *Biomedical Optics Express*, vol. 2, pp. 2837–2849, Sept. 2011. PMID: 22025988 PMCID: PMC3190961.

[124] C. Hagen, K. Grnewald, S. Schmidt, and J. Mller, "Accumulation of secondary carotenoids in flagellates of haematococcus pluvialis (chlorophyta) is accompanied by an increase in per unit chlorophyll productivity of photosynthesis," *European Journal of Phycology*, vol. 35, no. 01, pp. 75–82, 2000.

[125] H. E. Schaffer, R. R. Chance, R. J. Silbey, K. Knoll, and R. R. Schrock, "Conjugation length dependence of raman scattering in a series of linear polyenes: Implications for polyacetylene," *The Journal of Chemical Physics*, vol. 94, pp. 4161–4170, Mar. 1991.

[126] S. F. Parker, S. M. Tavender, N. M. Dixon, H. Herman, K. P. J. Williams, and W. F. Maddams, "Raman spectrum of beta-carotene using laser lines from green (514.5 nm) to near-infrared (1064 nm): Implications for the characterization of conjugated polyenes," *Applied Spectroscopy*, vol. 53, pp. 86–91, Jan. 1999.

[127] C. Castiglioni, J. T. Lopez Navarrete, G. Zerbi, and M. Gussoni, "A simple interpretation of the vibrational spectra of undoped, doped and photoexcited polyacetylene: Amplitude mode theory in the GF formalism," *Solid State Communications*, vol. 65, pp. 625–630, Feb. 1988.

[128] C. Castiglioni, M. Gussoni, M. Del Zoppo, and G. Zerbi, "Relaxation contribution to hyperpolarizability. a semiclassical model," *Solid State Communications*, vol. 82, pp. 13–17, Apr. 1992.

[129] D. Y. Paraschuk and V. M. Kobryanskii, "Coherent electron-lattice vibrations in trans-nanopolyacetylene probed by raman scattering," *Physical Review Letters*, vol. 87, p. 207402, Oct. 2001.

[130] "Effect of cc coherent vibration on relative raman scattering cross sections of all-trans -carotene," vol. 26.

[131] C. Castiglioni, M. Delzoppo, P. Zuliani, and G. Zerbi, "Experimental molecular hyperpolarizabilities from vibrational-spectra in systems with large electron-phonon coupling," *Synthetic Metals*, vol. 74, pp. 171–177, Sept. 1995. WOS:A1995TB70400013.

[132] F. Schulte, J. Mder, L. W. Kroh, U. Panne, and J. Kneipp, "Characterization of pollen carotenoids with in situ and high-performance thin-layer chromatography supported resonant raman spectroscopy," *Analytical Chemistry*, vol. 81, pp. 8426–8433, Oct. 2009.

[133] D. B. Thomas, P. C. Nascimbene, C. J. Dove, D. A. Grimaldi, and H. F. James, "Seeking carotenoid pigments in amber-preserved fossil feathers," *Scientific Reports*, vol. 4, June 2014.

[134] S. Keller, B. Schrader, A. Hoffmann, W. Schrader, K. Metz, A. Rehlaender, J. Pahnke, M. Ruwe, and W. Budach, "Application of near-infrared-fourier transform raman spectroscopy in medical research," *Journal of Raman Spectroscopy*, vol. 25, pp. 663–671, July 1994.

[135] C. Castiglioni, M. Del Zoppo, and G. Zerbi, "Reply to comment on molecular first hyperpolarizability of push-pull polyenes: Relationship between electronic and vibrational contribution by a two-state model ," *Physical Review B*, vol. 56, pp. 2275–2276, July 1997.

[136] B. Subramanian, N. Tchoukanova, Y. Djaoued, C. Pelletier, M. Ferron, and J. Robichaud, "Investigations on the geometrical isomers of astaxanthin: Raman spectroscopy of conjugated polyene chain with electronic and mechanical confinement," *Journal of Raman Spectroscopy*, vol. 45, pp. 299–304, Apr. 2014. WOS:000334156000005.

[137] A. C. Albrecht, "On the theory of raman intensities," *The Journal of Chemical Physics*, vol. 34, no. 5, p. 1476, 1961.

[138] L. Brambilla, M. Tommasini, G. Zerbi, and R. Stradi, "Raman spectroscopy of polyconjugated molecules with electronic and mechanical confinement: the spectrum of corallium rubrum," *Journal of Raman Spectroscopy*, vol. 43, no. 10, pp. 1449–1458, 2012.

[139] F. Zerbetto, M. Z. Zgierski, F. Negri, and G. Orlandi, "Theoretical study of the force fields of the three lowest singlet electronic states of linear polyenes," *The Journal of Chemical Physics*, vol. 89, pp. 3681–3688, Sept. 1988.

[140] K. Kodama and Y. Mori, "Overtone intensities in resonance raman scattering," *Chemical Physics*, vol. 46, pp. 371–378, Mar. 1980.

[141] L. D. Ziegler and A. C. Albrecht, "Preresonance raman scattering of overtones: The scattering of two overtones of benzene in the ultraviolet," *Journal of Raman Spectroscopy*, vol. 8, pp. 73–80, Apr. 1979.

[142] C. Castiglioni, M. Tommasini, and M. Del Zoppo, "Experimental vibrational contributions to molecular hyperpolarisabilities: methods and measurements," *Journal of Molecular Structure*, vol. 521, pp. 137–155, Mar. 2000.

[143] D. M. Bishop and B. Kirtman, "Comment on "molecular first hyperpolarizability of push-pull polyenes: Relationship between electronic and vibrational contribution by a two-state model"," *Phys. Rev. B*, vol. 56, pp. 2273–2274, Jul 1997.

[144] B. Kirtman, B. Champagne, and J.-M. Andre, "Role of collective modes in vibrational polarizabilities and hyperpolarizabilities of polyacetylene and other quasilinear polymers," *The Journal of Chemical Physics*, vol. 104, no. 11, p. 4125, 1996.

[145] D. M. Bishop and B. Kirtman, "A general finite-field scheme for the calculation of frequency-dependent electronicvibrational hyperpolarizabilities," *The Journal of Chemical Physics*, vol. 109, pp. 9674–9676, Dec. 1998.

[146] J. P. Hermann, "Third-order polarizabilities of long-chain molecules," *Journal of Applied Physics*, vol. 45, no. 11, p. 5100, 1974.

[147] M. Del Zoppo, C. Castiglioni, P. Zuliani, A. Razelli, M. Tommasini, G. Zerbi, and M. Blanchard-Desce, "Use of vibrational spectra for the determination of first-order molecular hyperpolarizabilities of pushpull polyenes as function of structural parameters," *Journal of Applied Polymer Science*, vol. 70, pp. 1311–1320, Nov. 1998.

[148] D. Tokarz, R. Cisek, M. Garbaczewska, D. Sandkuijl, X. Qiu, B. Stewart, J. D. Levine, U. Fekl, and V. Barzda, "Carotenoid based bio-compatible labels for third harmonic generation microscopy," *Physical Chemistry Chemical Physics*, vol. 14, no. 30, p. 10653, 2012.

[149] R. Withnall, B. Z. Chowdhry, J. Silver, H. G. M. Edwards, and L. F. C. de Oliveira, "Raman spectra of carotenoids in natural products," *Spectrochimica Acta Part A: Molecular and Biomolecular Spectroscopy*, vol. 59, pp. 2207–2212, Aug. 2003.

[150] A. M$\dot{}\cdot$ *u*ller, R. Lumry, and M. S. Walker, "Light-intensity dependence of the in vivo fluorescence lifetime of chlorophyll*," *Photochemistry and Photobiology*, vol. 9, pp. 113–126, Feb. 1969.

[151] S. J. Strickler and R. A. Berg, "Relationship between absorption intensity and fluorescence lifetime of molecules," *The Journal of Chemical Physics*, vol. 37, pp. 814–822, Aug. 1962.

[152] N. Mataga, Y. Kaifu, and M. Koizumi, "The solvent effect on fluorescence spectrum - change of solute-solvent interaction during the lifetime of excited solute molecule," *Bulletin of the Chemical Society of Japan*, vol. 28, no. 9, pp. 690–691, 1955. WOS:A1955WX55200019.

[153] R. Spencer and G. Weber, "Influence of brownian rotations and energy transfer upon measurements of fluorescence lifetime," *Journal of Chemical Physics*, vol. 52, no. 4, pp. 1654–&, 1970. WOS:A1970F560400006.

[154] P. I. H. Bastiaens and A. Squire, "Fluorescence lifetime imaging microscopy: spatial resolution of biochemical processes in the cell," *Trends in Cell Biology*, vol. 9, pp. 48–52, Feb. 1999.

[155] J. Lakowicz, H. Szmacinski, K. Nowaczyk, W. Lederer, M. Kirby, and M. Johnson, "Fluorescence lifetime imaging of intracellular calcium in cos cells using quin-2," *Cell Calcium*, vol. 15, no. 1, pp. 7–27, 1994.

[156] R. Sanders, A. Draaijer, H. C. Gerritsen, P. M. Houpt, and Y. K. Levine, "Quantitative pH imaging in cells using confocal fluorescence lifetime imaging microscopy," *Analytical Biochemistry*, vol. 227, pp. 302–308, May 1995.

[157] N. Galletly, J. McGinty, C. Dunsby, F. Teixeira, J. Requejo-Isidro, I. Munro, D. Elson, M. Neil, A. Chu, P. French, and G. Stamp, "Fluorescence lifetime imaging distinguishes basal cell carcinoma from surrounding uninvolved skin," *British Journal of Dermatology*, vol. 159, pp. 152–161, July 2008.

[158] E. Dimitrow, I. Riemann, A. Ehlers, M. J. Koehler, J. Norgauer, P. Elsner, K. Knig, and M. Kaatz, "Spectral fluorescence lifetime detection and selective melanin imaging by multiphoton laser tomography for melanoma diagnosis," *Experimental Dermatology*, vol. 18, pp. 509–515, June 2009.

[159] E. A. Jares-Erijman and T. M. Jovin, "FRET imaging," *Nature Biotechnology*, vol. 21, pp. 1387–1395, Nov. 2003. WOS:000186320000042.

[160] J. B. Edel, J. S. Eid, and A. Meller, "Accurate single molecule FRET efficiency determination for surface immobilized DNA using maximum likelihood calculated lifetimes," *The Journal of Physical Chemistry B*, vol. 111, pp. 2986–2990, Mar. 2007.

[161] B. Schuler and W. A. Eaton, "Protein folding studied by single-molecule FRET," *Current Opinion in Structural Biology*, vol. 18, pp. 16–26, Feb. 2008.

[162] C. Joo, H. Balci, Y. Ishitsuka, C. Buranachai, and T. Ha, "Advances in single-molecule fluorescence methods for molecular biology," *Annual Review of Biochemistry*, vol. 77, pp. 51–76, June 2008.

[163] N. G. Walter, C.-Y. Huang, A. J. Manzo, and M. A. Sobhy, "Do-it-yourself guide: how to use the modern single-molecule toolkit," *Nature Methods*, vol. 5, pp. 475–489, June 2008.

[164] W. Becker, *The bh TCSPC Handbook, 4th ed.* Becker and Hickl GmbH, 2010.

[165] S. Ly, G. McNerney, S. Fore, J. Chan, and T. Huser, "Time-gated single photon counting enablesseparation of CARS microscopy data frommultiphoton-excited tissue autofluorescence," *Optics Express*, vol. 15, pp. 16839–16851, Dec. 2007.

[166] A. D. Slepkov, A. Ridsdale, H.-N. Wan, M.-H. Wang, A. F. Pegoraro, D. J. Moffatt, J. P. Pezacki, F.-J. Kao, and A. Stolow, "Forward-collected simultaneous fluorescence lifetime imaging and coherent anti-stokes raman scattering microscopy," *Journal of Biomedical Optics*, vol. 16, no. 2, pp. 021103–021103, 2011.

[167] I. W. Schie, T. Weeks, G. P. McNerney, S. Fore, J. K. Sampson, S. Wachsmann-Hogiu, J. C. Rutledge, and T. Huser, "Simultaneous forward and epi-CARS microscopy with a single detector by timecorrelated single photon counting," *Optics Express*, vol. 16, pp. 2168–2175, Feb. 2008.

[168] M. Weinigel, H. G. Breunig, and K. Knig, "A novel clinical multimodal multiphoton tomograph for AF, SHG, CARS imaging, and FLIM," vol. 8948, pp. 89481R–89481R–6, 2014.

[169] "Spc 150 high performance tcspc module,"

[170] "Pml 16-c: 16 channel detector head for time-correlated single photon counting,"

[171] R. Sjöback, J. Nygren, and M. Kubista, "Absorption and fluorescence properties of fluorescein," *Spectrochimica Acta Part A: Molecular and Biomolecular Spectroscopy*, vol. 51, pp. L7–L21, June 1995.

[172] M. Krishna, "Excited-state kinetics of the hydrophobic probe nile red in membranes and micelles," *The Journal of Physical Chemistry A*, vol. 103, no. 19, pp. 3589–3595, 1999.

[173] S. S. Brody, "Fluorescence lifetime, yield, energy transfer and spectrum in photosynthesis, 1950–1960*," *Photosynthesis research*, vol. 73, no. 1-3, pp. 127–132, 2002.

[174] C. H. Huang, J. R. Lapides, and I. W. Levin, "Phase-transition behavior of saturated, symmetric chain phospholipid bilayer dispersions determined by raman spectroscopy: correlation between spectral and thermodynamic parameters," *Journal of the American Chemical Society*, vol. 104, pp. 5926–5930, Nov. 1982.

[175] W. Min, C. W. Freudiger, S. Lu, and X. S. Xie, "Coherent nonlinear optical imaging: Beyond fluorescence microscopy," *Annual Review of Physical Chemistry*, vol. 62, pp. 507–530, May 2011.

[176] P. Nandakumar, A. Kovalev, and A. Volkmer, "Vibrational imaging based on stimulated raman scattering microscopy," *New Journal of Physics*, vol. 11, p. 033026, Mar. 2009. WOS:000264725600001.

[177] K. I. Popov, A. F. Pegoraro, A. Stolow, and L. Ramunno, "Image formation in CARS and SRS: effect of an inhomogeneous nonresonant background medium," *Optics Letters*, vol. 37, pp. 473–475, Feb. 2012.